

# A Line-free Method of Monopoles for 3D Dislocation Dynamics

Thesis by  
Arnold Deffo

In Partial Fulfillment of the Requirements for the  
Degree of  
Doctor of Philosophy

The logo for the California Institute of Technology (Caltech), featuring the word "Caltech" in a bold, orange, sans-serif font.

CALIFORNIA INSTITUTE OF TECHNOLOGY  
Pasadena, California

2019  
Defended July 31, 2018

© 2019

Arnold Deffo

ORCID: 0000-0001-9077-8315

All rights reserved except where otherwise noted

In loving memory of Ma'a Angèle.  
This work is the result of your sacrifices over the years.

## ACKNOWLEDGEMENTS

It's hard to believe that after five years of graduate studies, the most difficult part of writing this thesis is the *Acknowledgements* section. Indeed, so many people have contributed to my success over the years that despite my best efforts, I'm afraid I'll forget to mention some of them here. To those people, I sincerely apologize and hope you know that I appreciate all you've done in helping shape the person I'm today.

With that said, I'd first and foremost like to thank my father Pa'a Fra and my brothers Bleriaud, Joël, Chanel, and Borel. Your optimism and confidence was a never-ending source of motivation. I particularly think of my father who, though he didn't have a high school diploma, seemed to know the value of having a good education.

Second, I'd like to thank my advisor Prof. Michael Ortiz. You showed patience and understanding throughout this process and gave me the space and freedom to develop into the kind of researcher I'm today. I'm also grateful to Prof. Pilar Ariza for acting as a second advisor to me. I particularly appreciate your willingness to mentor me on some of the most basic tasks of my Ph.D. work.

Third, I'd like to thank Lydia Suarez for treating me like a mother treats a son. I don't take for granted everything you've done for me and will remember it for years to come. I'm also grateful to the members of the Ortiz research group, past and present, for their willingness to lend a helping hand and provide feedback whenever needed. I'm especially thankful to Jonathan Chiang for providing assistance with some of the computer science components of my work.

Beyond the lab, I'd like to thank my many friends for providing relief from the stress I experienced throughout this process. As challenging as this journey has been, it would be more so without your support and laughs. I'm particularly indebted to the Sander family for providing me with a home away from home.

To Steve and Phyllis Brady: I'm thankful to you in so many ways that trying to list them here will be a futile experiment. Let me just say that your willingness to mentor that young student from Cameroon is something for which he will forever be grateful.

Going back further, this journey would not have been possible without papa Fokou Bernard who gave me the opportunity to pursue my studies in the U.S. Just like

me, I'm sure many young Bansas appreciate the financial support you so willingly offer, which support provides life-long opportunities we would not have otherwise.

Finally, I'd like to thank Mr. and Mrs. Foster and Coco Stanback for providing funding for this thesis work through the *Stanback STEM Fellowship* in Aerospace.

## ABSTRACT

Despite the emergence of architected materials for various applications, metals still play a key role in engineering in general and aeronautics in particular. Turbine blades in jets engines for instance are made from single-crystal Nickel superalloys. As a result, studying the failure mechanism of these crystalline materials would help understand the limits for their application. At the core of this mechanism are line defects called *dislocations*. Indeed, the plastic deformation of metals is governed by the motion of dislocation ensembles inside the crystal. In this thesis, we propose a novel approach to dislocation dynamics through the *method of monopoles*. In this approach, we discretize the dislocation line as a collection of points (or *monopoles*), each of which carries a Burgers "charge" and an element of line. The fundamental difference between our method and current methods for dislocation dynamics lies in the fact that the latter discretize the dislocation as a collection of line segments from which spans a need to keep track of the connectivity of the nodes. In our approach, we propose a "line-free" discretization where a linear connectivity or sequence between monopoles need not be defined. This attribute of the formulation offers significant computational advantages in terms of simplicity and efficiency. Through verification examples, we show that our method is consistent with existing results for simple configurations. We then build on this success to investigate increasingly complex examples, with the ultimate goal of simulating the plastic deformation of a *body-centered cubic* grain in an elastic matrix.

## PUBLISHED CONTENT AND CONTRIBUTIONS

- [1] A. Deffo, M. P. Ariza, and M. Ortiz. “A Line-free Method of Monopoles for 3D Dislocation Dynamics”. In: *ArXiv e-prints* (June 2018). arXiv: 1806.04512 [physics.comp-ph].  
A.D. participated in the development of the theory, the writing of the source code for numerical simulations, and the writing of the manuscript through figures and the derivation of various equations.

## TABLE OF CONTENTS

Acknowledgements . . . . .	iv
Abstract . . . . .	vi
Published Content and Contributions . . . . .	vii
Table of Contents . . . . .	viii
List of Illustrations . . . . .	x
Chapter I: Introduction . . . . .	1
1.1 Motivation . . . . .	1
1.2 Perfect and Real Crystals . . . . .	3
1.3 More on Dislocations . . . . .	7
1.4 Outline of the Thesis . . . . .	15
Chapter II: Continuum Theory of Dislocations . . . . .	17
2.1 Introduction . . . . .	17
2.2 Review of Classical Linear Elasticity Theory . . . . .	18
2.3 Straight Dislocations . . . . .	23
2.4 Curved Dislocations . . . . .	32
2.5 Forces on a Dislocation . . . . .	41
Chapter III: A Method of Monopoles for Dislocation Dynamics . . . . .	47
3.1 Introduction . . . . .	47
3.2 Previous Approaches to Dislocation Dynamics . . . . .	47
3.3 Introduction to the Method of Monopoles . . . . .	52
3.4 Dislocation Dynamics as a Transport Problem . . . . .	54
3.5 Mobility and Energetics . . . . .	59
3.6 Variational Formulation and Approximation . . . . .	67
3.7 Topological Transitions . . . . .	75
3.8 Summary . . . . .	79
Chapter IV: Verification Examples . . . . .	80
4.1 Introduction . . . . .	80
4.2 Infinite Straight Screw Dislocation . . . . .	80
4.3 Infinite Straight Edge Dislocation . . . . .	85
4.4 Circular Prismatic Dislocation Loop . . . . .	87
4.5 Summary . . . . .	94
Chapter V: Numerical Examples . . . . .	96
5.1 Introduction . . . . .	96
5.2 Activation of a Single Slip Plane . . . . .	96
5.3 Activation of a Single Slip System . . . . .	97
5.4 Activation of Multiple Slip Systems . . . . .	102
Chapter VI: Conclusion . . . . .	106
6.1 Summary . . . . .	106
6.2 Future Work . . . . .	107

Bibliography . . . . .	109
Appendix A: Interpolated Transport Maps . . . . .	120
A.1 Zeroth-order Max Ent Shape Functions . . . . .	120
A.2 Tests . . . . .	120

## LIST OF ILLUSTRATIONS

<i>Number</i>	<i>Page</i>
1.1 Difference in the path of a refracted wave in a metamaterial (with negative index of refraction) and in water (with positive index of refraction). . . . .	1
1.2 Classification of materials classes by their strength-to-weight ratio. Image credit: <a href="http://www-materials.eng.cam.ac.uk/mpsite/interactive_charts/strength-density/basic.html">http://www-materials.eng.cam.ac.uk/mpsite/interactive_charts/strength-density/basic.html</a> . . . . .	2
1.3 Schematic of a perfect crystal with a unit cell highlighted. . . . .	4
1.4 Intrinsic point defects in a crystal. . . . .	4
1.5 Extrinsic point defects in a crystal. . . . .	5
1.6 Schematic of grain boundaries separating three single crystals of different orientations. . . . .	6
1.7 (Deformation) twin boundary in a crystal. . . . .	7
1.8 Plastic deformation of a single crystal through shearing. . . . .	8
1.9 Sequence showing the role of dislocations in the plastic deformation of crystals. . . . .	10
1.10 <i>SF/RH</i> Burgers circuit and Burgers vector in a crystal with a dislocation. The positive sense of dislocation line is taken out of the page. . . . .	11
1.11 <i>FS/RH</i> Burgers circuit and Burgers vector in a crystal with a dislocation. The positive sense of dislocation line is taken out of the page. . . . .	11
1.12 Equivalent Burgers circuits and corresponding (identical) Burgers vectors in a dislocated crystal using the <i>FS/RH</i> convention. The positive sense of dislocation line is taken out of the page. . . . .	13
1.13 Conservation of Burgers vector at a dislocation node. . . . .	14
1.14 Illustration of edge and screw dislocations in a continuum. The dislocation line is shown in the dash-dot pattern with direction $\xi$ . . . . .	15
1.15 Illustration of a mixed dislocation in a continuum. The dislocation line is shown in the dash-dot pattern with direction $\xi$ . . . . .	16
2.1 Schematic illustrating the definition of the Burgers vector of a dislocation in an elastic continuum. . . . .	17

2.2	Stress distribution on an infinitesimal volume element. . . . .	19
2.3	Body under displacement boundary conditions $\bar{u}_i$ on its boundary $\partial B_1$ and traction boundary conditions $\bar{t}_i$ on its boundary $\partial B_2$ . Note that if no traction or displacement is prescribed at a boundary, this is equivalent to having a traction of $\bar{t}_i = 0$ at said boundary. . . . .	20
2.4	Screw dislocation along the positive $x_3$ axis in a cartesian coordinate system. . . . .	24
2.5	Screw dislocation along the positive $x_3$ axis in a hollow cylinder used to compute the strain energy of the dislocation. . . . .	26
2.6	Edge dislocation along the positive $x_3$ axis in a cartesian coordinate system. . . . .	27
2.7	Edge dislocation along the positive $x_3$ axis in a hollow cylinder used to compute the strain energy of the dislocation. . . . .	29
2.8	Mixed dislocation in an infinite medium with its Burgers vector inclined at an angle $\beta$ to the dislocation line. . . . .	30
2.9	Displacement at the point $\boldsymbol{x}$ due to a point force at $\boldsymbol{x}'$ inside an anisotropic solid with boundary $S$ . Here $\Delta S$ is any surface enclosing $\boldsymbol{x}'$ . . . . .	33
2.10	Schematic of a (closed) curved dislocation $L$ in an infinite solid. $S_0$ is an arbitrary surface bounded by the dislocation. . . . .	36
2.11	Schematic of the surface cap used for determination of the displacement field of a curved dislocation. The cap consists of the cut faces $S_0^-$ and $S_0^+$ and a tubular surface, $\Gamma_0$ , of radius $r_0$ centered around the dislocation line. . . . .	36
2.12	Schematic of two dislocation loops within an infinite elastic continuum.	39
2.13	Schematic of a dislocation loop within an infinite elastic continuum.	41
2.14	An element $d\boldsymbol{l}$ of dislocation line moves a distance $d\boldsymbol{x}$ , thus increasing the area swept by the dislocation by the amount $\delta S_0 = d\boldsymbol{x} \times d\boldsymbol{l}$ . . . . .	42
2.15	Principle of superposition used to define the image stress in a bounded solid with a dislocation [71, 72]. $\boldsymbol{\sigma}$ corresponds to the stress in the finite dislocated solid as shown on the left. $\boldsymbol{\sigma}^\infty$ corresponds to the stress in the infinite dislocated solid. This creates tractions $t_i^\infty$ at the boundary that would delimit the real finite solid. Finally, $\boldsymbol{\sigma}^I$ is the image stress in the finite solid free of dislocations. Note the traction boundary conditions used in this case. . . . .	44

2.16	Illustration of the core regularization proposed by Brown [74] in 1964. The self-stress at $\boldsymbol{x}$ is computed as the average of those at $\boldsymbol{x} \pm \epsilon \boldsymbol{m}$ , where $\boldsymbol{m}$ is the in-plane normal to the dislocation at $\boldsymbol{x}$ . . . . .	45
2.17	Illustration of the core regularization proposed by Hirth and Lothe [26]. The self-stress at $\boldsymbol{x}$ is computed using Equation (2.69) but excluding a those points $\boldsymbol{x}'$ that are a distance less than $\epsilon$ away from $\boldsymbol{x}$ . . . . .	45
3.1	Discretization of a curved dislocation into line segments (in red) in lattice-based simulations. The integration points are taken as the middles of the segments. The outward arrows indicate the only possible directions of motion of the segments. . . . .	49
3.2	Discretization of a curved dislocation into line segments (in red) in nodal simulations. . . . .	50
3.3	Circular prismatic loop. a) Regularized energy normalized by $\frac{\mu b^2 \rho^2}{8\pi(1-\nu)\epsilon}$ . b) Regularized Peach-Koehler force per unit length normalized by $\frac{\mu b^2}{8\pi(1-\nu)\epsilon}$ . Loop radius normalized by $\epsilon$ . . . . .	67
3.4	Convergence with respect to the number of monopoles for a circular prismatic loop. a) Regularized elastic energy normalized by $\frac{\mu b^2 \rho^2}{8\pi(1-\nu)\epsilon}$ . b) Regularized Peach-Koehler force normalized by $\frac{\mu b^2}{8\pi(1-\nu)\epsilon}$ . Loop radius normalized by $\epsilon$ . . . . .	75
3.5	Schematic of junction formation. Two intersecting glissile dislocation lines of Burgers vectors $\boldsymbol{b}_1$ and $\boldsymbol{b}_2$ zip up along a line of direction $\boldsymbol{\xi}$ on the intersection between their slip planes to form a sessile segment of Burgers vector $\boldsymbol{b}_3 = \boldsymbol{b}_1 + \boldsymbol{b}_2$ . . . . .	76
4.1	Discretization of the screw dislocation segment in the method of monopoles.	81
4.2	Discretization of the screw dislocation segment in the method of monopoles.	85
4.3	Circular prismatic dislocation loop in an elastic continuum. . . . .	88
4.4	Discretization of the circular dislocation loop in the method of monopoles.	89
4.5	Evolution of a circular prismatic dislocation loop under its self-stress in the method of monopoles. As expected, the dislocation shrinks under its self-stress while remaining circular. The grey lines indicate the trajectories of the monopoles. . . . .	90
4.6	Evolution of a circular prismatic dislocation loop under the action of an applied stress $\sigma_{33}^\infty > 0$ . The dislocation expands under the applied stress while remaining circular. The grey lines indicate the trajectories of the monopoles. . . . .	91

4.7	Accuracy of the algorithm in predicting the correct elements of line length. Test case of the expanding circular prismatic loop. . . . .	93
4.8	Splitting of a monopole into two new ones. The Burgers vector of each new monopole is the same as that of the parent monopole, while the element of line vector is half that of the parent monopole. . . . .	93
4.9	Evolution of a circular prismatic dislocation loop under the action of an applied stress $\sigma_{33}^{\infty} > 0$ where we have implemented the splitting algorithm described in the text. The grey lines indicate the trajectories of the monopoles. . . . .	95
5.1	BCC grain in elastic matrix. Snapshots of single loop nucleating from a randomly-located source and expanding under the action of an applied uniaxial stress until it reaches the impenetrable boundaries of the grain. . . . .	98
5.2	BCC grain in elastic matrix. Snapshots of multiple loops nucleating from a common randomly-located source and expanding under the action of an applied uniaxial stress until they reach the impenetrable boundaries of the grain. . . . .	99
5.3	BCC grain in elastic matrix. Snapshots of single loops nucleating from randomly-located sources on multiple parallel slip planes and expanding under the action of an applied uniaxial stress until they reach the impenetrable boundaries of the grain. . . . .	100
5.4	BCC grain in elastic matrix. Snapshots of multiple loops nucleating from randomly-located sources on multiple parallel slip planes and expanding under the action of an applied uniaxial stress until they reach the impenetrable boundaries of the grain. . . . .	101
5.5	BCC grain in elastic matrix. Snapshots of two loops nucleating from two different randomly-located sources on two slip systems and subsequently expanding under the action of an applied uniaxial stress until they reach the impenetrable boundaries of the grain. . . . .	103
5.6	BCC grain in elastic matrix. Snapshots of multiple loops nucleating from randomly-located sources on multiple slip planes and expanding under the action of an applied uniaxial stress until they reach the impenetrable boundaries of the grain. . . . .	104
5.7	Computed plastic strain plotted against the monotonically increasing remote stress for the dislocation ensemble displayed in Figure 5.6. . . . .	105

## Chapter 1

### INTRODUCTION

#### 1.1 Motivation

Thanks to recent advances in materials science and engineering, researchers are now able to design materials tailored to specific applications. Consequently, it has become possible to meet design criteria that heretofore seemed unachievable. A prime example is the use of metamaterials in electromagnetism. From the Greek *meta-* meaning "beyond", metamaterials are materials engineered to have electromagnetic properties not found in nature [1–3]. One such property is the ability to have a negative index of refraction over a range of frequencies [2–5]. To understand the implication of this property, consider an incident wave from air into water. Since the index of refraction of water is positive, the path of the refracted wave will be as shown in Figure 1.1a. However, if the wave travels from air into a metamaterial with negative index of refraction, the refracted wave will instead follow the trajectory shown in Figure 1.1b. An important application of this property is the ability to use metamaterials in the design of "superlenses", i.e. lenses which, unlike conventional glass lenses, have resolution beyond the diffraction limit [6–8]. Beyond lenses, metamaterials also have applications in high-gain small antennas, electromagnetic absorbers, and ideal cloaking devices [2, 3, 7, 9–11].

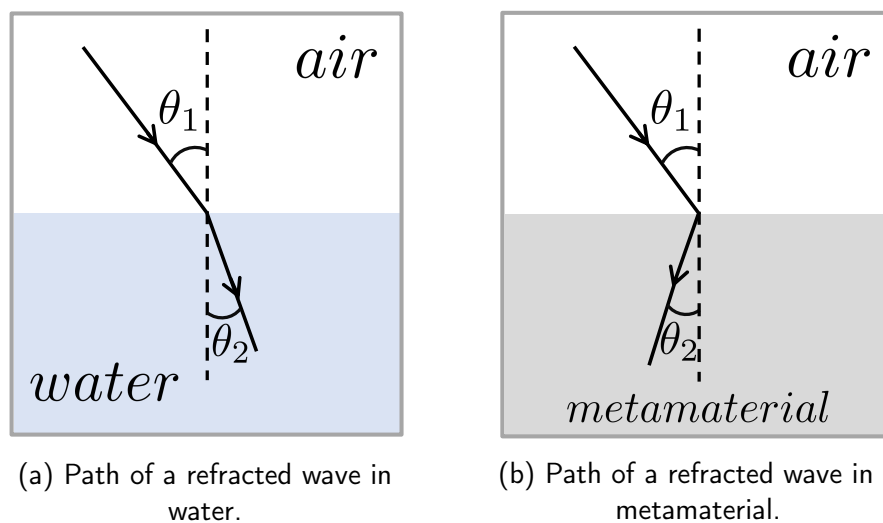


Figure 1.1: Difference in the path of a refracted wave in a metamaterial (with negative index of refraction) and in water (with positive index of refraction).

Another example of human-made materials for engineering purposes concerns the use of carbon fiber reinforced polymer (CFRP) in engineering structures where both strength and weight are important design parameters. Indeed, as shown in the *Ashby* plot of Figure 1.2, CFRP, or "composites" for short, have strength comparable to that of traditional metals while maintaining a lower density. For this reason, they have seen much use in the aerospace industry, where the airplane structure must be strong enough to withstand the loads experienced by the aircraft during flight while light enough that significant fuel savings can ensue. It is then no surprise that Boeing's *787 Dreamliner* and Airbus's *A350XWB* both have fuselage and wing structures made primarily of CFRP, making up 50% of the airplane's weight [12–14].

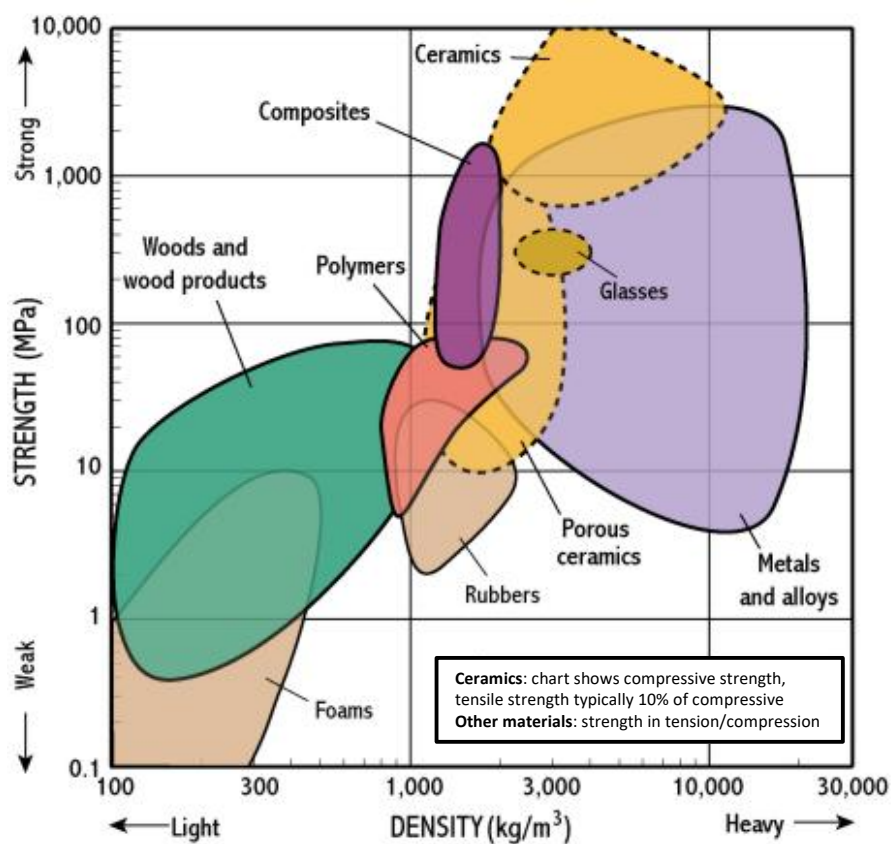


Figure 1.2: Classification of materials classes by their strength-to-weight ratio.

Image credit: [http://www-materials.eng.cam.ac.uk/mpsite/interactive\\_charts/strength-density/basic.html](http://www-materials.eng.cam.ac.uk/mpsite/interactive_charts/strength-density/basic.html)

It is evident from the above two examples that architected materials have a promising future in science and engineering. However, despite the now widespread use of composites in the *787 Dreamliner*, aluminum and titanium still make up 20

and 15% of the weight of the aircraft, respectively [12]. Furthermore, steel columns and beams are still prevalent structural elements in civil engineering. Finally, metals also have applications in medicine where titanium has become the material of choice in surgical implant procedures [15–17]. In other words, traditional materials and metals in particular are still ubiquitous in science and engineering and require just as much research. In this thesis, we deal with dislocations as line defects. Specifically, given the role of dislocations as agents of plastic deformation in metals, we propose a new approach to dislocation dynamics that offers significant computational advantages in terms of simplicity, robustness, and efficiency. However, before we lay out the details of this new approach, we first give a brief review of defects in crystals—Section 1.2. Section 1.3 expands on this topic further by specifically considering dislocations as line defects. Finally, the outline of the thesis is given in Section 1.4.

## 1.2 Perfect and Real Crystals

Metals and many important classes of nonmetallic solids are *crystalline*, i.e. the constituents atoms are arranged in a pattern or *unit cell* that repeats itself periodically over three-dimensional space [18–20]. This is illustrated in Figure 1.3 for the case of a simple cubic structure. When a crystalline solid has a structure as described above, it is said to be a *perfect* or *ideal crystal*. However, the regular, strictly periodic structure of a crystal as described above is merely an idealized picture [21]. In nature, even under conditions of ideal thermodynamic equilibrium, *real crystals* deviate considerably from the aforementioned ideal model. All deviations from the ideal crystalline structure are called *crystal defects* [21, 22]. These defects, which strongly influence the properties of the crystal, can be classified into four main categories according to their dimensionality: point defects, line defects, surface defects, and volume defects [18, 19, 21, 22].

### Point defects

Point defects are crystalline defects of dimension zero. Depending on the nature of the defect, they can be further classified as *intrinsic* or *extrinsic* [18].

Intrinsic point defects are characteristic of pure metals, i.e. metals comprising of only one element (*Cu*, *Zn*, *Ni*, etc.). Examples include *vacancies* and *self-interstitials*. A vacancy is a crystal lattice defect where an atom is absent from a site where one should be expected. This is highlighted in Figure 1.4a. A self-interstitial on the other hand is a point defect where an atom is occupying a site that would

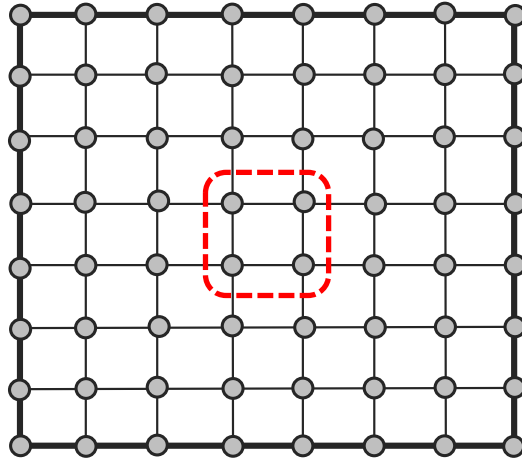
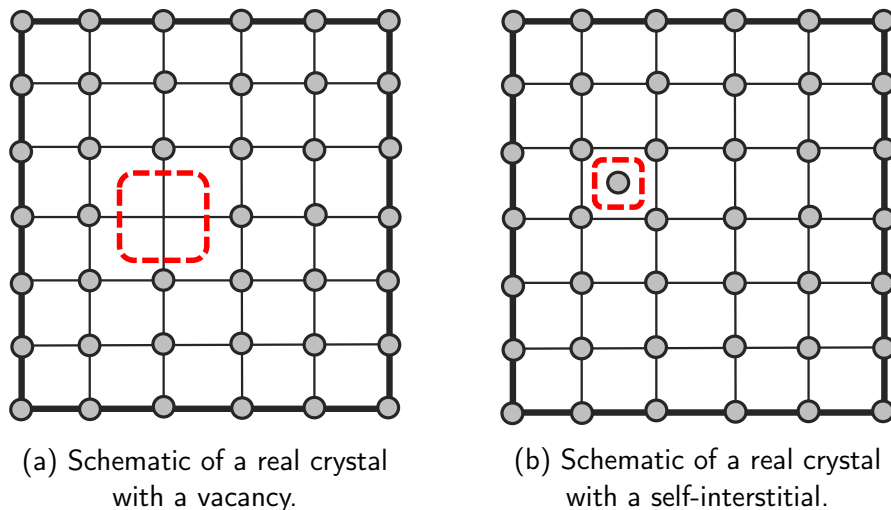


Figure 1.3: Schematic of a perfect crystal with a unit cell highlighted.

otherwise be free—see Figure 1.4b.



(a) Schematic of a real crystal with a vacancy.

(b) Schematic of a real crystal with a self-interstitial.

Figure 1.4: Intrinsic point defects in a crystal.

Extrinsic point defects on the other hand can only occur when a crystal contains foreign elements. Examples include *substitutional impurity atoms* and *interstitial impurity atoms*. A substitutional impurity atom is a lattice defect where a foreign (or "impurity") atom replaces (or "substitutes") a parent atom at a lattice site in the atomic structure [18]. An interstitial impurity atom is a point defect similar to a self-interstitial, but with the major distinction that the interstitial is a foreign atom. These concepts are illustrated in Figure 1.5a and 1.5b respectively.

It should be noted that the atomic lattice will typically be distorted in the vicinity

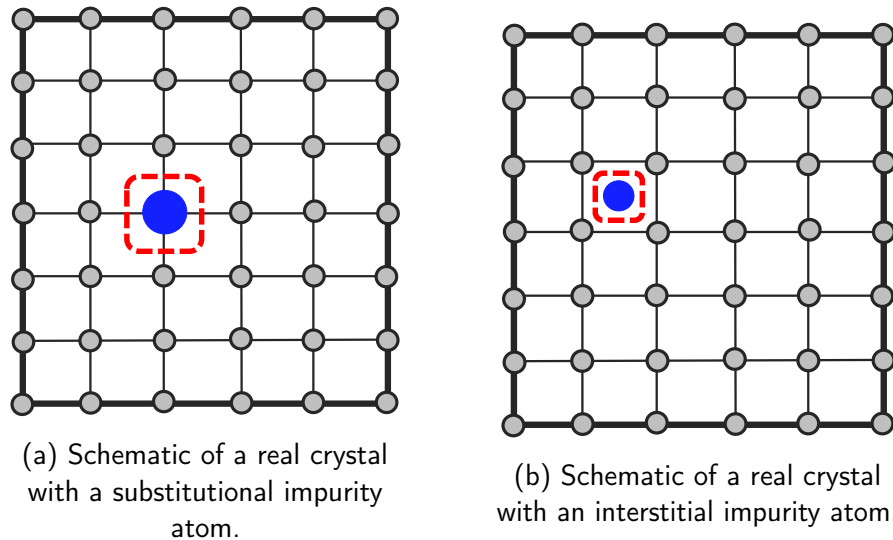


Figure 1.5: Extrinsic point defects in a crystal.

of these defects. However, this is not illustrated in the simplified schematics of Figures 1.4 and 1.5.

### Line defects

As suggested by the name, line defects are lattice defects of dimension one. In crystalline materials, these comprise of *dislocations* and *disclinations*. Unlike point defects which have short-range effects, dislocations and disclinations disturb the long-range order in a crystal [21]. Though recent research has evidenced the presence of disclinations in crystalline solids [23], these defects are commonly associated with liquid crystals [24, 25]. Indeed, disclinations—or "rotational dislocations" as they are sometimes called—do not appear as isolated defects in metals [19, 26], and we refer the interested reader to references [27–33] for further reading on the topic. As a result, we will only focus on dislocations as line defects in crystals. However, we defer this discussion until Section 1.3.

### Surface defects

These two-dimensional defects can be of many types, ranging from the mere presence of a crystal surface to stacking faults (irregularly packed atom layers), grain boundaries, and twin boundaries [18–22].

Since a perfect crystal is one in which atoms are arranged in a pattern that repeats itself periodically over space, one such crystal must necessarily be infinite. However, given that every crystal must be finite in size, there must be surfaces (i.e. 2-D

defects) that interrupt the infinite periodicity of the crystal, thus leading to surface defects [19, 21].

Moreover, crystalline solids usually consist of a large number of randomly oriented single crystals [18]. A grain boundary is the interface where two single crystals of different orientations join in such a manner that the material is continuous across the boundary [26]. Though Figure 1.6 illustrates this for straight grain boundaries, a grain boundary need not be straight. However, straight grain boundaries are more energetically favorable in thermal equilibrium since they minimize the boundary area and thus the boundary energy [26].

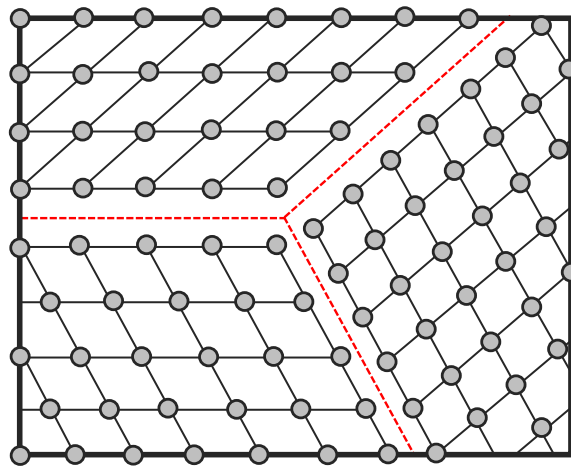


Figure 1.6: Schematic of grain boundaries separating three single crystals of different orientations.

Finally, a twin is a crystal with consistently mutually misoriented regions (twin components) whose atomic structure is related geometrically by some symmetry operation (e.g. reflection in a plane) [21]. In general, twins are of two classes: *growth twins* and *deformation twins*. Growth twins arise during crystal growth and deformation twins arise through mechanical stress [22]. Specifically, deformation twinning is the process through which a region of the crystal undergoes homogeneous shear that produces the original crystal structure in a new orientation [18]. As a result, the twin component of the resulting crystal is a mirror image of the parent crystal through the *twin* or *composition plane*. This process is represented schematically in Figure 1.7.

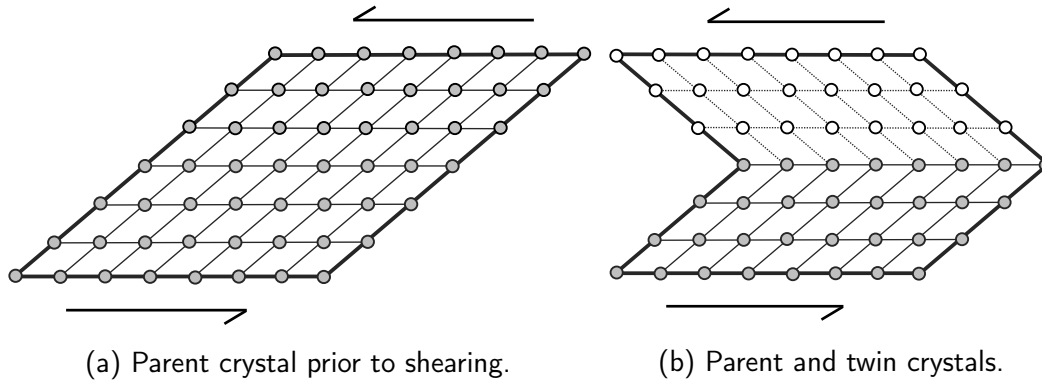


Figure 1.7: (Deformation) twin boundary in a crystal.

### Volume defects

Volume defects are three-dimensional defects that include *voids* (or clusters of vacancies), *precipitates* (or cluster of impurities), *inclusions*, and similar macroscopic formations [18, 21]. Though considered defects, some of these can be intentional as is the case in the development of high-strength alloys through the interaction between dislocations and precipitates.

### 1.3 More on Dislocations

Given that the subject matter of this thesis deals with dislocations, we return to these line defects to elaborate on the discussion started in Section 1.2.

#### Background on dislocations

Dislocations first appeared as an abstract mathematical concept in a 1907 paper by Volterra [33]. However, it would take researchers more than two decades to fully appreciate the role of these line defects in the plastic deformation of crystals.

To start, consider the crystal on the left in Figure 1.8 with a defect as shown. Suppose we wish to "push" the defect outside the crystal through shear so as to obtain the configuration shown on the right.

In a perfect crystal, the sliding of one plane of atoms over an adjacent one would have to be a rigid cooperative motion of all atoms from one position of the perfect lattice to another [18]. Frenkel [34] first estimated the shear stress required for this process in 1926. Given the periodicity of the lattice, he assumed a periodic shear stress of form [18, 26, 35]

$$\tau(x) = \tau_{\text{theor}} \sin \frac{2\pi x}{b}, \quad (1.1)$$

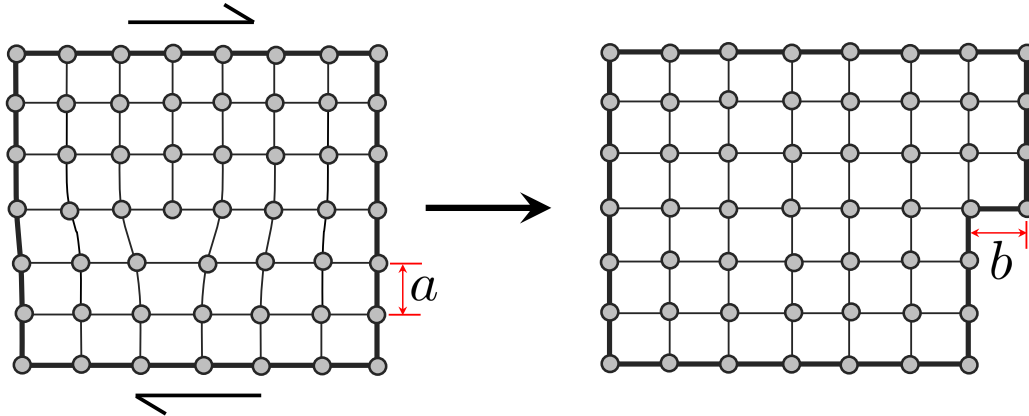


Figure 1.8: Plastic deformation of a single crystal through shearing.

where  $b$  is the magnitude of a simple lattice-translation vector (see Figure 1.8),  $x$  is the shear translation of the two rows away from the low-energy equilibrium position, and  $\tau_{\text{theor}}$  is the theoretical maximum shear stress of the crystal.

In the limit of small shear strain  $x/a$ , where  $a$  is the spacing between two adjacent rows of atoms (see Figure 1.8), Hooke's law dictates that

$$\tau(x) = \mu \frac{x}{a}, \quad (1.2)$$

where  $\mu$  is the shear modulus of the crystal.

Comparing equations (1.1) and (1.2) in the small strain limit, one obtains

$$\mu \frac{x}{a} = \tau_{\text{theor}} \sin \frac{2\pi x}{b} \cong \tau_{\text{theor}} \frac{2\pi x}{b},$$

from which it follows that

$$\tau_{\text{theor}} = \frac{\mu}{2\pi} \frac{b}{a}$$

or, since  $b \cong a$ ,

$$\tau_{\text{theor}} \cong \frac{\mu}{2\pi}. \quad (1.3)$$

Using more realistic expressions for the shear stress as a function of shear displacements, later estimates placed the theoretical value of the maximum shear stress between  $\mu/30$  and  $\mu/5$  at room temperature [26]. However, except for *whiskers* which are nearly free of defects, experimental observations in real, well-annealed crystals showed that the stress required for plastic deformation is at least several orders of magnitude smaller than the above estimates, between  $10^{-9}\mu$  and  $10^{-4}\mu$  [18, 20, 26, 35]. It wasn't until 1934 with the independent works of Taylor, Polanyi,

and Orowan [36–39] that dislocations were found to be the source of plastic deformation in crystalline materials. More specifically, rather than an entire row of atoms sliding rigidly over another, dislocations allow nearby atoms (and only these) to move one interatomic distance as the imperfection progressively advances inside the crystal (see Figure 1.9). As a result, much lower shear stresses are needed for plastic deformation, thus explaining the discrepancies between the theoretical and experimental values of the maximum shear stress in crystalline solids.

Today, dislocations are known to affect the mechanical, electrical, and even optical properties of crystals [40, 41]. Therefore, understanding the nature of these linear defects is of great importance in these various fields.

### **Burgers vector and Burgers circuit**

As a one-dimensional crystal defect, a dislocation is uniquely characterized by a line direction and a "slip" vector called the *Burgers vector* [19, 20, 26]. This vector is the most important property of a dislocation and is constant along the dislocation line—except possibly in the highly strained regions near the center of the dislocation where the atomicity of the structure cannot be neglected—and remains so when the dislocation travels through the crystal [20, 35]. There are several equivalent definitions of the Burgers vector of a dislocation with some more useful than others depending on the context. For example, in Chapter 2, we'll encounter a definition more appropriate for that context. In the meantime, the most useful definition is given in terms of what is commonly referred to as the *Burgers circuit* [18–20, 26, 35].

A Burgers circuit consists of any sequence of atom-to-atom steps and forms a closed loop when drawn in a perfect crystal. However, when the same Burgers circuit encloses a dislocation, it does not end at the starting atom and thus does not form a closed loop. The vector pointing from the starting atom to the ending atom, needed to complete the loop, is the Burgers vector of the dislocation. This is illustrated in Figure 1.10, where  $\mathbf{b}$  represents the Burgers vector.

The convention used in the above characterization of the Burgers vector is sometimes referred to as the *SF/RH* Burgers circuit, meaning "Start to Finish; Right Hand" convention. An equivalent definition can be stated starting with a closed loop in a dislocated crystal, and retracing the same circuit in a perfect crystal. In this case, the vector pointing from the ending atom to the starting atom needed to complete the loop is the Burgers vector of the dislocation—see Figure 1.11. Not

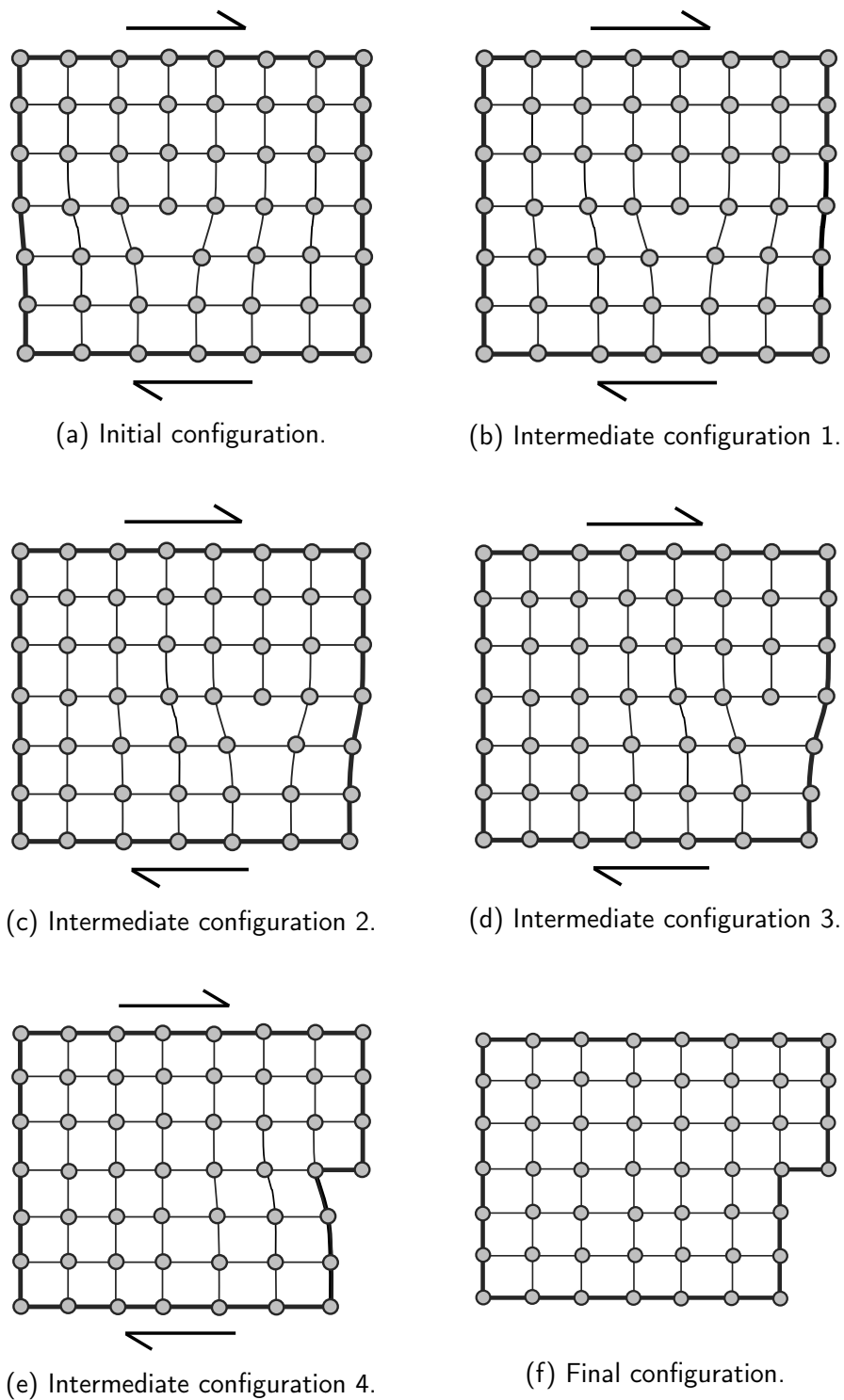


Figure 1.9: Sequence showing the role of dislocations in the plastic deformation of crystals.

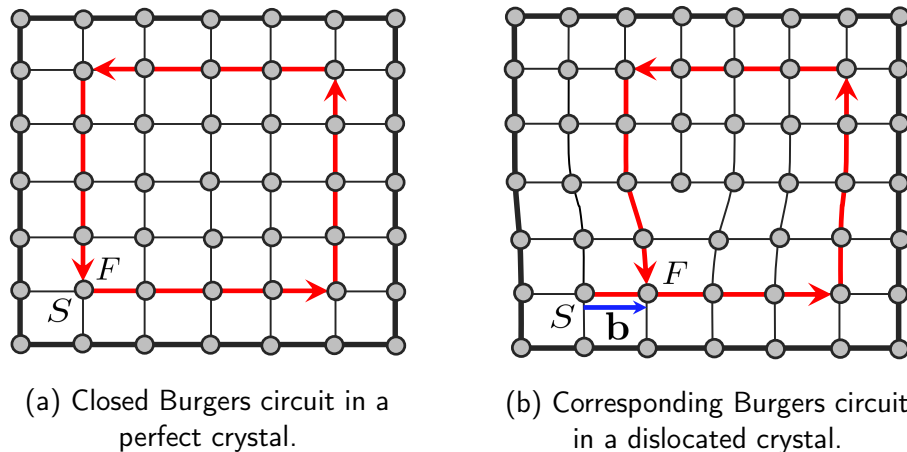


Figure 1.10: *SF/RH* Burgers circuit and Burgers vector in a crystal with a dislocation. The positive sense of dislocation line is taken out of the page.

surprisingly, this latter convention is known as the *FS/RH* characterization of the Burgers circuit. Nevertheless, as stated earlier, these two definitions are equivalent, as can be evidenced by the identical Burgers vectors in Figures 1.10b and 1.11b.

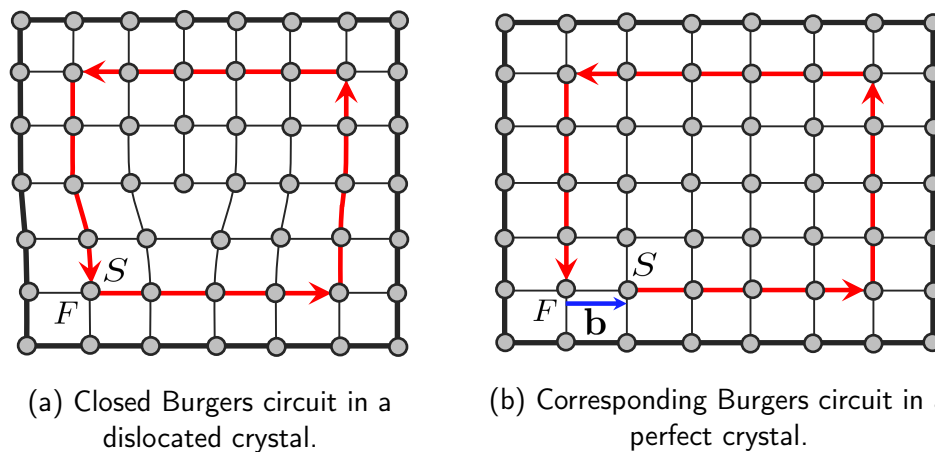


Figure 1.11: *FS/RH* Burgers circuit and Burgers vector in a crystal with a dislocation. The positive sense of dislocation line is taken out of the page.

### Equivalent Burgers Circuits

Using the *FS/RH* convention, consider the two Burgers circuits shown in the dislocated crystal of Figure 1.12a. Following the above example, we subsequently draw corresponding circuits in the perfect crystal. As can be seen from Figure 1.12b, both circuits result in the same Burgers vector, i.e.  $\mathbf{b}_1 = \mathbf{b}_2$ . When this is the case, the circuits are said to be *equivalent*. More precisely, two Burgers circuits

are said to be equivalent if one can be translated or deformed to coincide with the other without cutting through any "bad" material during this process [20, 26].

We can now prove the statement made earlier that the Burgers vector is constant along the dislocation line. In doing so, we consider a Burgers circuit around the dislocation. This circuit can be translated and deformed (through "good" material) along the dislocation line. By virtue of equivalent Burgers circuits, the resulting Burgers vectors should be identical to that of the original circuit. Thus, the Burgers vector is conserved along the dislocation.

Another important consequence of the equivalence of Burgers circuits is the fact that *a dislocation cannot end inside a crystal. It must either form a closed loop, meet with other dislocations to form a node, or end at the surface of the crystal or at grain boundaries* [18, 20, 26]. Indeed, consider a crystal with a single dislocation of nonzero Burgers vector and suppose that this dislocation ends inside the crystal. Then, the original Burgers circuit can be translated and deformed so that it remains a closed loop while enclosing only "good" parts of the crystal, resulting in a zero Burger vector. By equivalence of Burgers circuits, the corresponding Burgers vectors should be identical, i.e. both zero in this case. But this contradicts the initial assumption that the dislocation had a nonzero Burgers vector.

We end our discussion of equivalent Burgers circuits by looking at the relationship between Burgers vectors for dislocations meeting at a node. To this end, we consider the dislocations of Figure 1.13 with their respective Burgers vectors and line directions as shown. We further assume that the host crystal is otherwise free of other defects. Then, the Burgers circuits  $\mathcal{A}$  and  $\mathcal{B}$  are equivalents and we have that

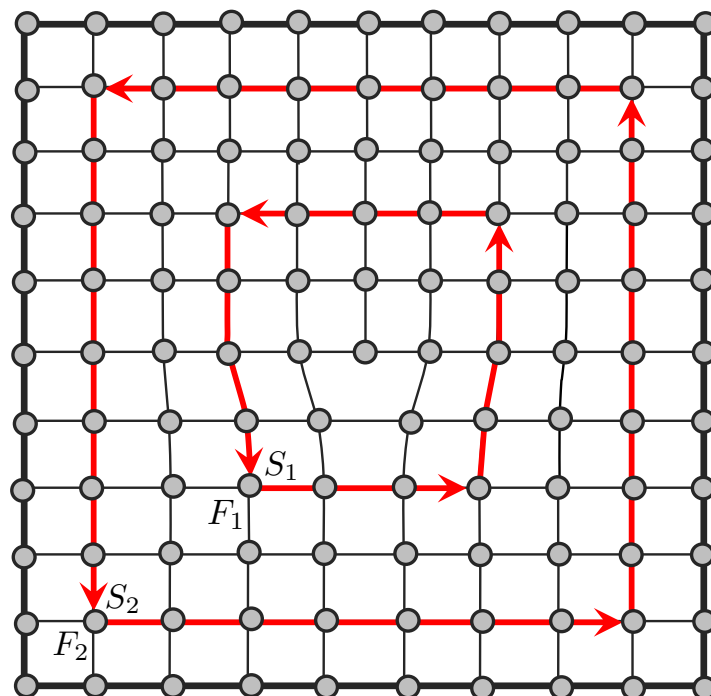
$$\mathbf{b}_1 = \mathbf{b}_2 + \mathbf{b}_3.$$

If the line direction  $\xi_1$  of the first dislocation is reversed, then the corresponding Burgers vector  $\mathbf{b}_1$  is also reversed. This follows immediately from considering a Burgers circuit oriented in the opposite direction to that shown in Figure 1.13. In this case, equivalence of Burgers circuit gives

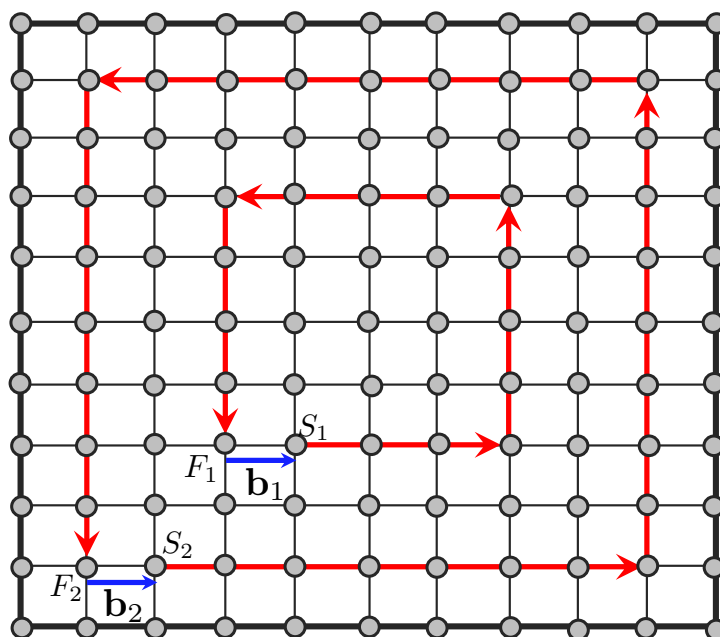
$$\mathbf{b}_1 + \mathbf{b}_2 + \mathbf{b}_3 = \mathbf{0}$$

or, more generally, for  $n$  branching dislocations all oriented away from the node,

$$\sum_{i=1}^n \mathbf{b}_i = \mathbf{0}. \quad (1.4)$$



(a) Two Burgers circuit in a dislocated crystal.



(b) Corresponding circuits in a perfect crystal.

Figure 1.12: Equivalent Burgers circuits and corresponding (identical) Burgers vectors in a dislocated crystal using the *FS/RH* convention. The positive sense of dislocation line is taken out of the page.

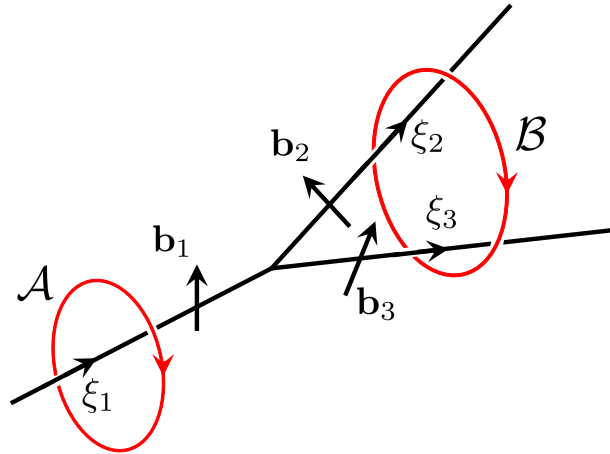


Figure 1.13: Conservation of Burgers vector at a dislocation node.

This is known as *Frank's theorem* for conservation of Burgers vector at a dislocation node [20]. Notice the analogy to Kirchhoff's law of electrical currents.

### Edge, screw, and mixed dislocations

Recall that a dislocation is uniquely characterized by a line direction  $\xi$  and a Burgers vector  $b$ . Depending on the orientations of these two, a dislocation can be of *edge*, *screw*, or *mixed* character [18–20, 26, 35].

A dislocation is said to be of edge character when its Burgers vector is perpendicular to the dislocation line. Mathematically, this is equivalent to saying that  $b \cdot \xi = 0$ . In fact, these are the dislocations that were postulated by Taylor, Orowan, and Polanyi in 1934 [36–39] in their explanation of the discrepancies between the theoretical and experimental values for the maximum shear stress of metals. As such, figures 1.8, 1.9, 1.10b, 1.11a, and 1.12a are all illustrations of edge-type dislocations, where the dislocation line is pointing into the page and the Burgers vector is as shown. Furthermore, Figure 1.14a illustrates an edge dislocation in a continuum.

When the dislocation line is parallel to the Burgers vector, the dislocation is said to be of screw type. This is equivalent to saying that the cross-product of  $b$  and  $\xi$  is zero, or  $b \times \xi = \mathbf{0}$ . Because it is typically difficult to illustrate these dislocations using crystal lattices, we have not attempted to do so here. For this, the reader is referred to figures 1.20 and 2.2 of references [18] and [20] respectively. Instead, we have reproduced in Figure 1.14b the illustration from [19] for a screw dislocation in an elastic continuum.

Generally, however, a dislocation is neither completely edge or screw. Instead, it is curved and usually comprises of edge and screw components together. In this case, the dislocation is said to be of mixed type as illustrated in Figure 1.15a. At every location along the dislocation, the Burgers vector can be decomposed—see Figure 1.15b—into screw and edge components given respectively by

$$\mathbf{b}_s = (\mathbf{b} \cdot \boldsymbol{\xi})\boldsymbol{\xi} \quad (1.5)$$

and

$$\mathbf{b}_e = \mathbf{b} - \mathbf{b}_s. \quad (1.6)$$

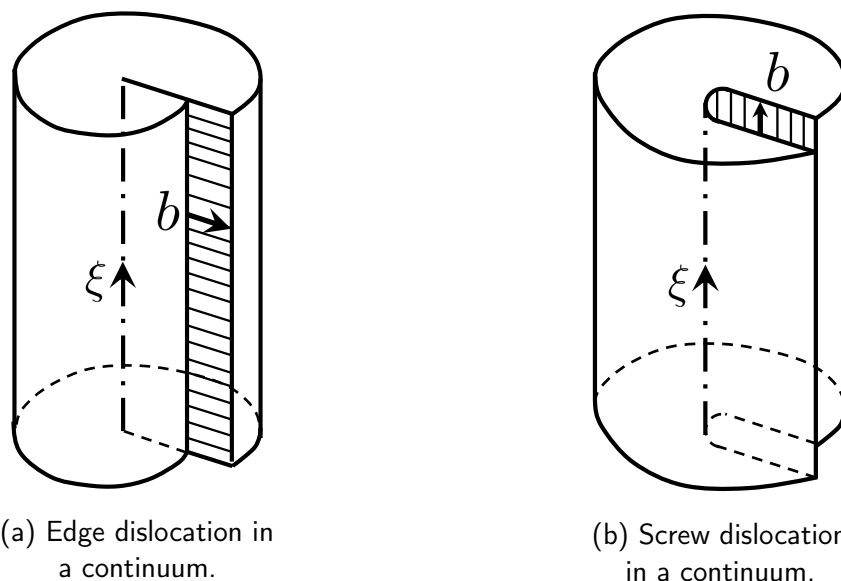


Figure 1.14: Illustration of edge and screw dislocations in a continuum. The dislocation line is shown in the dash-dot pattern with direction  $\boldsymbol{\xi}$ .

#### 1.4 Outline of the Thesis

In the preceding, we have introduced dislocations as line defects in crystalline materials. In doing so, our presentation relied heavily on the atomic crystal structure to illustrate the relevant concepts. However, in what follows, and as is typically done in line dislocation dynamics simulations, it'll be more convenient to look at dislocations as defects in an elastic continuum. To this end, Chapter 2 is devoted to the continuum theory of dislocations. In this chapter, we derive expressions for the elastic field of straight and curved dislocations. This sets the stage for Chapter 3, where we lay out the theory of the aforementioned novel

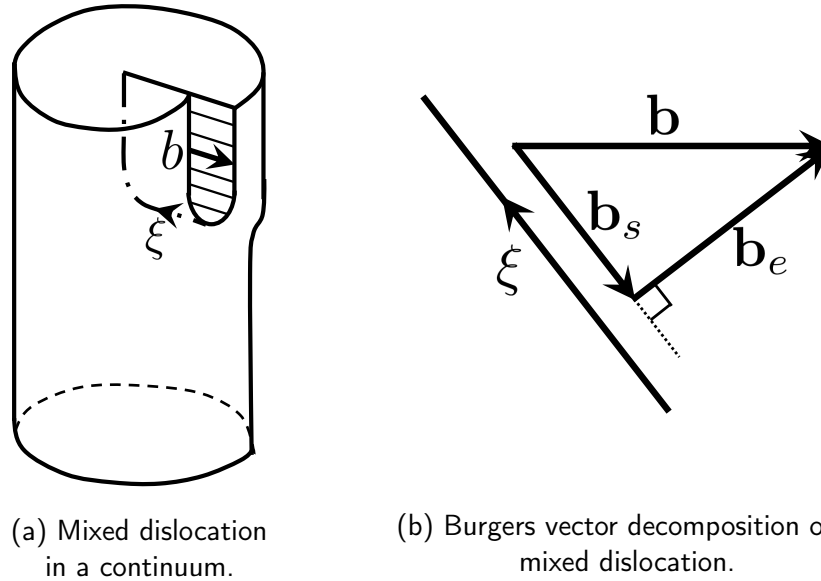


Figure 1.15: Illustration of a mixed dislocation in a continuum. The dislocation line is shown in the dash-dot pattern with direction  $\xi$ .

approach which we call *the method of monopoles*. In an effort to show the validity of this approach, Chapter 4 deals with verification examples. It is shown that the method of monopoles gives results consistent with the expected behavior for these canonical examples. Building on this success, Chapter 5 investigates increasingly complex examples, this with the ultimate goal of simulating the plastic deformation of a body-centered cubic grain in an elastic matrix. Finally, Chapter 6 contains the main conclusions of this work and provides some future research directions building on this new approach.

## CONTINUUM THEORY OF DISLOCATIONS

## 2.1 Introduction

The phrase "continuum theory of dislocations" is ambiguous as sometimes it implies the theory of isolated dislocations in an elastic continuum and sometimes the theory of continuous distributions of infinitesimal dislocations [42]. This chapter is concerned with the former, while the latter will be discussed in Chapter 3. Recall that in Chapter 1 we defined the Burgers vector of a dislocation schematically in terms of the Burgers circuit while making use of the crystal structure of the solid. In this chapter, we consider the solid to be an elastic continuum and as a result, a different—yet equivalent—definition of the Burgers vector of a dislocation must be given. More specifically, given a line  $L$  inside an elastic continuum,  $L$  is said to be a dislocation of Burgers vector  $\mathbf{b}$  if the displacement field  $\mathbf{u}$  around  $L$  is such that [26, 43]

$$\mathbf{b} = \oint_C \frac{\partial \mathbf{u}}{\partial l} dl, \quad (2.1)$$

where  $dl$  is the infinitesimal element of line around the closed loop  $C$ . This is illustrated in Figure 2.1 where, as before,  $\xi$  is the dislocation line direction. It is worth noting that Figure 2.1 and Equation (2.1) make use of the *SF/RH* convention for the direction of the Burgers vector with respect to the dislocation line.

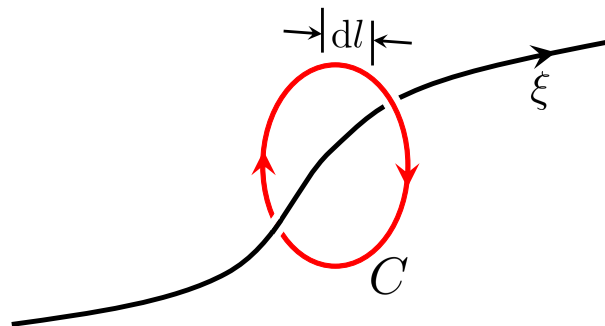


Figure 2.1: Schematic illustrating the definition of the Burgers vector of a dislocation in an elastic continuum.

As mentioned in the above definition, the variable  $\mathbf{u}$  is the displacement field inside the body due to the dislocation. More generally, the effect of a dislocation on the

properties of a solid is associated primarily with the internal strain and stress fields and with the strain energy of the dislocation [26]. However, before we can derive these elastic fields, it is necessary to review the relevant elements of classical linear elasticity theory. This is the subject of Section 2.2. This theory is then applied in Sections 2.3 and 2.4 to obtain the elastic field of straight and curved dislocations respectively. Finally, Section 2.5 is devoted to forces on dislocations.

## 2.2 Review of Classical Linear Elasticity Theory

Linear elasticity is a specialization of continuum mechanics to a subclass of materials in which the stress tensor in any element is determined exclusively by the strain tensor in the same element and, furthermore, the relationship between these two tensors is a linear one [44]. In other words, in classical linear elasticity, the stress tensor at a point inside the body is a linear function of the strain tensor at the same point. This is known as (*generalized*) *Hooke's law*. There are several references on the subject of linear elasticity. Classic ones include references [45–48]. However, [49–51] were also found to be excellent references. As a result of this vast literature, we do not attempt to give here an extensive survey of the topic. Interested readers should consult the references just mentioned for that purpose. Instead, we only revisit those equations as given in [44] and [26] that will be relevant to subsequent sections of this chapter. Finally, here and throughout this thesis, we will use index notation and Einstein's summation convention on repeated indices.

In classical linear elasticity theory, the displacement field is the variable of interest. This is denoted by  $\mathbf{u}$  or, using index notation,  $u_i$  where  $i = 1, 2, 3$ . The position of a material point inside the body is denoted by  $\mathbf{x}$  or simply  $x_i$ . In linear elasticity theory, deformations are small enough that the components of  $\mathbf{u}$  and  $\mathbf{x}$  can be taken with respect to the undeformed or deformed configurations. Furthermore, the theory also assumes that the distortions  $\partial u_i / \partial x_j$  are small, leading to the following expression for the strain tensor  $\varepsilon$  at a point inside the body:

$$\varepsilon_{ij} = \frac{1}{2} \left( \frac{\partial u_i}{\partial x_j} + \frac{\partial u_j}{\partial x_i} \right)$$

or

$$\varepsilon_{ij} = \frac{1}{2} (u_{i,j} + u_{j,i}) , \quad (2.2)$$

where we have used the comma to represent differentiation with respect to the corresponding component of  $\mathbf{x}$ .

Notice that

$$\varepsilon_{ij} = \varepsilon_{ji} \quad (2.3)$$

follows immediately from the above definition. Hence, the strain tensor is *symmetric*.

The stress tensor  $\sigma$  on the other hand is such that  $\sigma_{ij}$  gives the  $i$ th component of the force per unit area on a plane whose outward normal is parallel to the positive  $x_j$  direction—see Figure 2.2.

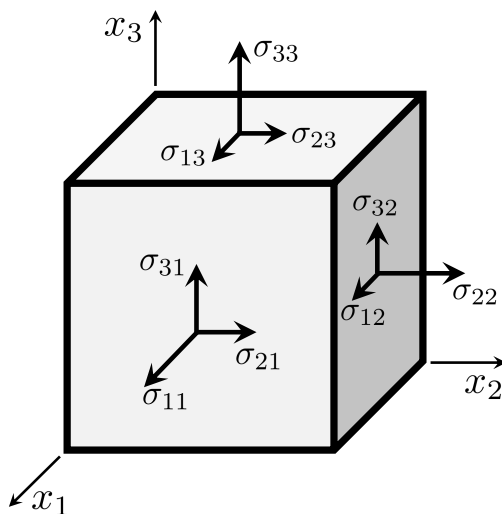


Figure 2.2: Stress distribution on an infinitesimal volume element.

Given a body  $B$  of density  $\rho$  with body force per unit volume  $\mathbf{f}$ , the stress state at every point inside  $B$  must satisfy

$$\sigma_{ij,j} + f_i = \rho \ddot{u}_i, \quad (2.4)$$

where  $\ddot{u}_i = \partial^2 u_i / \partial t^2$  is the acceleration of the material point. As given, Equation (2.4) is the *momentum conservation equation*.

For problems in elastostatics, i.e. where  $\ddot{u}_i = 0$ , Equation (2.4) reduces to

$$\sigma_{ij,j} + f_i = 0, \quad (2.5)$$

which is the *equilibrium equation* for classical elasticity.

If no internal torques are present, conservation of angular momentum requires that

$$\sigma_{ij} = \sigma_{ji}, \quad (2.6)$$

which implies that the stress tensor is also symmetric.

Furthermore, at an external surface of the body, we either have

$$\sigma_{ij}n_j = \bar{t}_i, \quad (2.7)$$

where  $\mathbf{n}$  is the outward normal to the surface and  $\bar{\mathbf{t}}$  the applied traction per unit area, or

$$u_i = \bar{u}_i, \quad (2.8)$$

where  $\bar{\mathbf{u}}$  is the prescribed displacement at the surface of the body.

The union of all traction boundary surfaces is usually denoted by  $\partial B_2$  and that of all displacement boundary surfaces by  $\partial B_1$  so that  $\partial B = \partial B_1 \cup \partial B_2$  with  $\partial B_1 \cap \partial B_2 = \emptyset$ —see Figure 2.3.

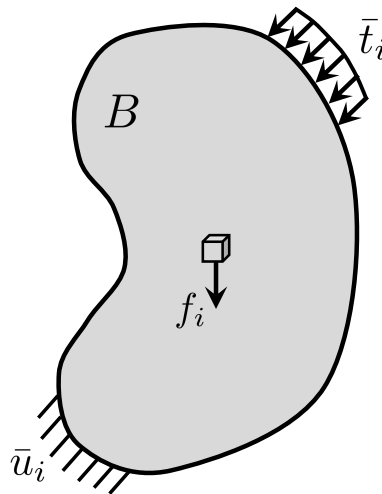


Figure 2.3: Body under displacement boundary conditions  $\bar{u}_i$  on its boundary  $\partial B_1$  and traction boundary conditions  $\bar{t}_i$  on its boundary  $\partial B_2$ . Note that if no traction or displacement is prescribed at a boundary, this is equivalent to having a traction of  $\bar{t}_i = 0$  at said boundary.

Next, recall that linear elasticity is characterized by a linear relationship between the stress and strain tensors. Specifically, we write

$$\sigma_{ij} = C_{ijkl}\varepsilon_{kl}, \quad (2.9)$$

where  $C_{ijkl}$  are the elastic constants of the material.

It immediately follows from Equations (2.3) and (2.6) that

$$C_{ijkl} = C_{jikl} = C_{ijlk} = C_{jilk},$$

and we say that the elastic modulus tensor has *minor symmetry*. Though we don't prove it here, the elastic modulus tensor also has *major symmetry*, viz

$$C_{ijkl} = C_{klij} .$$

As a result of these symmetries, the number of independent elastic constants decreases from 81 to 21 .

For an isotropic material, this is further reduced to only two elastic constants called *Lamé* constants. In this case, we have

$$C_{ijkl} = \lambda \delta_{ij} \delta_{kl} + \mu (\delta_{ik} \delta_{jl} + \delta_{il} \delta_{jk}) , \quad (2.10)$$

where  $\delta_{ij}$  is the Kronecker delta, being 1 when  $i = j$  and zero otherwise. The usual elastic constants can be expressed in terms of  $\lambda$  and  $\mu$  as follows:

- ◇ Young's modulus:  $E = \mu (3\lambda + 2\mu) / (\lambda + \mu)$  ,
- ◇ Poisson's ratio:  $\nu = \lambda / [2(\lambda + \mu)]$  ,
- ◇ Shear modulus:  $\mu$  ,
- ◇ Bulk modulus (or inverse compressibility):  $\kappa = \lambda + \frac{2}{3}\mu$  .

It should be noted that each of the above moduli can be similarly expressed in terms of any other two. The resulting table can be found on pages xxvii and 74 of references [51] and [50] respectively.

Using Equation (2.10), Hooke's law for isotropic solids becomes

$$\sigma_{ij} = \lambda \varepsilon_{kk} \delta_{ij} + 2\mu \varepsilon_{ij} . \quad (2.11)$$

Alternatively, strains can be expressed in terms of stresses as

$$\varepsilon_{ij} = \frac{1 + \nu}{E} \sigma_{ij} - \frac{\nu}{E} \sigma_{kk} \delta_{ij} . \quad (2.12)$$

The strain-energy density function, which represents the energy per unit volume associated with the deformation of the solid, is given by

$$W = \frac{1}{2} \sigma_{ij} \varepsilon_{ij} = \frac{1}{2} C_{ijkl} \varepsilon_{ij} \varepsilon_{kl} . \quad (2.13)$$

To summarize, the classical problem of static linear elasticity consists of solving the field Equations (2.5), (2.2), and (2.9) for the displacement field  $\mathbf{u}$ , the stress and strain tensors  $\boldsymbol{\sigma}$  and  $\boldsymbol{\varepsilon}$  subject to the boundary conditions (2.8) and (2.7) on  $\partial B_1$  and  $\partial B_2$  respectively—see Figure 2.3. Next, we look at two special cases arising from these boundary-value problems.

### Plane strain

In this section, we consider so-called *plane strain* problems in an isotropic medium. These are problems for which it is known a priori—or assumed—that the displacement field depends only on two components of position, with the displacement along the third component being identically zero. For instance, for a plane strain problem along the  $x_3$  axis, the displacement field is of the form

$$u_1 = u_1(x_1, x_2), \quad u_2 = u_2(x_1, x_2), \quad u_3 \equiv 0. \quad (2.14)$$

Consequently,

$$\varepsilon_{13} = 0, \quad \varepsilon_{23} = 0, \quad \varepsilon_{33} = 0. \quad (2.15)$$

When combined with Equation (2.11), (2.15) implies that

$$\sigma_{33} = \lambda(\varepsilon_{11} + \varepsilon_{22}), \quad \sigma_{13} = 0, \quad \sigma_{23} = 0. \quad (2.16)$$

Therefore, for a body in static equilibrium with no body forces, (2.5) becomes

$$\sigma_{11,1} + \sigma_{12,2} = 0, \quad (2.17a)$$

$$\sigma_{12,1} + \sigma_{22,2} = 0, \quad (2.17b)$$

where we have used symmetry of the stress tensor to write  $\sigma_{12,1}$  instead of  $\sigma_{21,1}$  in Equation (2.17b).

Equations (2.17) are satisfied automatically if there exists a function  $\Psi$  such that

$$\sigma_{11} = \Psi_{,22}, \quad \sigma_{22} = \Psi_{,11}, \quad \sigma_{12} = -\Psi_{,12}. \quad (2.18)$$

Such a function  $\Psi$  is commonly referred to as the *Airy stress potential*.

On the other hand, one can use Equation (2.2) to easily show that

$$\varepsilon_{11,22} + \varepsilon_{22,11} = 2\varepsilon_{12,12}. \quad (2.19)$$

Inserting (2.12) into (2.19) and making use of relations (2.18) to simplify while keeping in mind that  $\lambda = \nu E / [(1 + \nu)(1 - 2\nu)]$ , one arrives at

$$\frac{\partial^4 \Psi}{\partial x_1^4} + 2 \frac{\partial^4 \Psi}{\partial x_1^2 \partial x_2^2} + \frac{\partial^4 \Psi}{\partial x_2^4} = 0,$$

or

$$\left( \frac{\partial^2}{\partial x_1^2} + \frac{\partial^2}{\partial x_2^2} \right)^2 \Psi = 0. \quad (2.20)$$

Solving the above biharmonic equation yields the stresses  $\sigma_{11}$ ,  $\sigma_{22}$ , and  $\sigma_{12}$ , which in turn yield the corresponding strains through Equation (2.12). The displacements  $u_1$  and  $u_2$  follow from direct integration of the strains.

### Antiplane strain

We now consider an isotropic solid in a state of *antiplane strain*. In this case, two components of the displacement field are identically zero, with the nonzero component depending only on the position components along which the displacements are zero. For instance, for a state of antiplane strain along the  $x_3$  axis, the displacement field is of the form

$$u_1 \equiv 0, \quad u_2 \equiv 0, \quad u_3 = u_3(x_1, x_2). \quad (2.21)$$

Consequently, all strain components are zero except for  $\varepsilon_{13}$  and  $\varepsilon_{23}$  which in this case are given respectively by

$$\varepsilon_{13} = \frac{1}{2}u_{3,1} \quad \text{and} \quad \varepsilon_{23} = \frac{1}{2}u_{3,2}. \quad (2.22)$$

Accordingly, the nonzero components of stress are

$$\sigma_{13} = 2\mu\varepsilon_{13} = \mu u_{3,1} \quad \text{and} \quad \sigma_{23} = 2\mu\varepsilon_{23} = \mu u_{3,2}. \quad (2.23)$$

Hence, assuming no body forces in the solid, equilibrium equation (2.5) simplifies to

$$\nabla^2 u_3 = 0. \quad (2.24)$$

Thus, the antiplane strain problem reduces to solving Laplace's equation for  $u_3$  together with the relevant boundary conditions.

## 2.3 Straight Dislocations

Armed with the above review, we now proceed to derive the elastic field of straight dislocations in an isotropic medium, starting with those of screw type.

### Screw dislocations

Recall that a screw dislocation is one for which the Burgers vector is parallel to the dislocation line. In order to derive the corresponding elastic field, we'll make use of Figure 2.4 illustrating such a dislocation in an infinite medium with respect to a cartesian coordinate system.

- **Stress and displacement fields**

We start by noticing that the displacement components  $u_1$  and  $u_2$  are identically zero and that  $u_3$  is only a function of  $x_1$  and  $x_2$ . Therefore, we have a state of

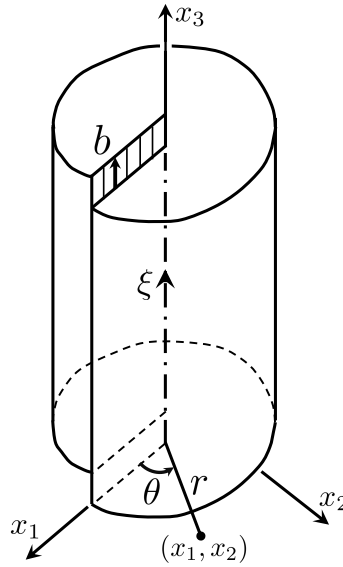


Figure 2.4: Screw dislocation along the positive  $x_3$  axis in a cartesian coordinate system.

antiplane strain as discussed in Section 2.2. Furthermore,  $u_3$  is only a function of the angle  $\theta$  as shown in Figure 2.4 and increases uniformly from zero to  $b$  as  $\theta$  increases from 0 to  $2\pi$ . The simplest form of  $u_3$  satisfying the above requirement is [18–20, 26, 35, 42, 44]

$$u_3 = \frac{b}{2\pi}\theta. \quad (2.25)$$

In cartesian coordinates, this becomes

$$u_3 = \frac{b}{2\pi} \tan^{-1} \left( \frac{x_2}{x_1} \right). \quad (2.26)$$

One can easily verify that  $\nabla^2 u_3 = 0$  as required by Equation (2.24). The nonzero components of the strain tensor follow from (2.22) as

$$\varepsilon_{13} = -\frac{b}{4\pi} \frac{x_2}{x_1^2 + x_2^2}, \quad (2.27a)$$

$$\varepsilon_{23} = \frac{b}{4\pi} \frac{x_1}{x_1^2 + x_2^2}. \quad (2.27b)$$

Using Equation (2.23), we obtain the corresponding nonzero stresses as

$$\sigma_{13} = -\frac{\mu b}{2\pi} \frac{x_2}{x_1^2 + x_2^2}, \quad (2.28a)$$

$$\sigma_{23} = \frac{\mu b}{2\pi} \frac{x_1}{x_1^2 + x_2^2}. \quad (2.28b)$$

The above derivation can also be done in polar coordinates, in which case Equations (2.26), (2.27), and (2.28) take the much simpler form

$$u_z = \frac{b\theta}{2\pi}, \quad (2.29a)$$

$$\varepsilon_{\theta z} = \varepsilon_{z\theta} = \frac{b}{4\pi r}, \quad (2.29b)$$

$$\sigma_{\theta z} = \sigma_{z\theta} = \frac{\mu b}{2\pi r}, \quad (2.29c)$$

with all other components of displacement, stress, and strain being zero.

### • Strain energy

We first notice that as  $r \rightarrow 0$ , the strain  $\varepsilon_{\theta z}$  and stress  $\sigma_{\theta z}$  diverge to infinity. Since solids cannot withstand infinite stresses, a hole of radius  $r_0$  must be inserted inside the infinite cylinder of Figure 2.4, the result of which is shown in Figure 2.5. However, since real crystals are not hollow, as we approach the center of the dislocation, linear elasticity theory ceases to be valid and a non-linear, atomistic model must be used instead [18, 26, 42]. This region around the dislocation where linear elasticity ceases to be valid is called the *core* of the dislocation. It is common to assume a value of  $r_0$  on the order of the Burgers vector magnitude  $b$  [18, 26, 44]. Therefore, in computing the strain energy of the screw dislocation, we will focus on the region outside this core and consider the hollow cylinder shown in Figure 2.5.

The strain energy per unit length inside the infinite hollow cylinder can be easily computed using polar coordinates. Using Equations (2.13), (2.29b), and (2.29c), it is found to be

$$\begin{aligned} \frac{W}{L} &= \int_{r_0}^R \int_0^{2\pi} \frac{1}{2} (\sigma_{\theta z} \varepsilon_{\theta z} + \sigma_{z\theta} \varepsilon_{z\theta}) r d\theta dr \\ &= \int_{r_0}^R \sigma_{\theta z} \varepsilon_{\theta z} 2\pi r dr \\ &= \frac{\mu b^2}{4\pi} \ln \left( \frac{R}{r_0} \right). \end{aligned} \quad (2.30)$$

As expected,  $W/L$  diverges as  $r_0 \rightarrow 0$ . However, it also diverges as  $R \rightarrow \infty$ . As a result, one cannot associate with the dislocation a definite characteristic energy. In fact, the energy depends on the size of the crystal. For a single dislocation,  $R$  is typically taken to be the distance from the dislocation to the nearest free surface. For a crystal containing many dislocations of both signs,  $R$  is taken to be half the average distance between the dislocations [26, 42].

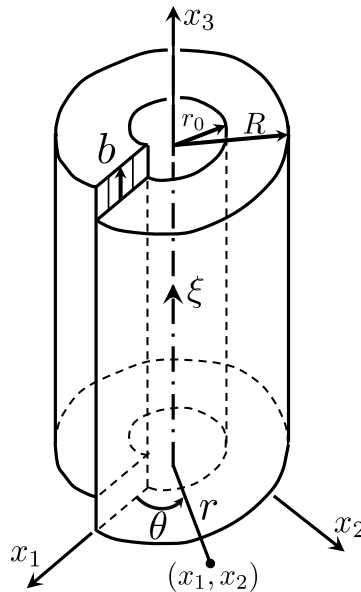


Figure 2.5: Screw dislocation along the positive  $x_3$  axis in a hollow cylinder used to compute the strain energy of the dislocation.

### Edge dislocations

We recall that in an edge dislocation, the Burgers vector is perpendicular to the dislocation line. In deriving the corresponding elastic field, we'll make use of Figure 2.6 illustrating such a dislocation in an infinite medium.

- **Stress and displacement fields**

For the dislocation depicted in Figure 2.6, the displacement component  $u_3$  is everywhere zero, as are all derivatives taken with respect to  $x_3$ . Hence, we have a state of plane strain as described in Section 2.2. To this end, solving the elastic field reduces to solving the biharmonic Equation (2.20) with the appropriate boundary conditions. We summarize below the derivation of [26], which starts by setting

$$\Phi = \nabla^2 \Psi. \quad (2.31)$$

Then  $\Phi$  satisfies Laplace equation. In polar coordinates, this means that

$$\left( \frac{\partial^2}{\partial r^2} + \frac{1}{r} \frac{\partial}{\partial r} + \frac{1}{r^2} \frac{\partial^2}{\partial \theta^2} \right) \Phi = 0. \quad (2.32)$$

It is well known that the harmonic Equation (2.32) is separable [26, 44] and thus

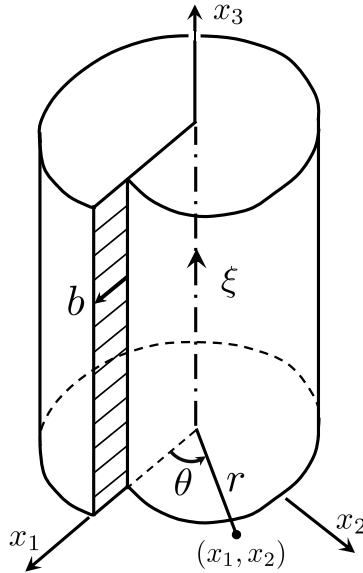


Figure 2.6: Edge dislocation along the positive  $x_3$  axis in a cartesian coordinate system.

has a single-valued solution of the form

$$\Phi = \alpha_0 + \beta_0 \ln r + \sum_{n=1}^{\infty} [(\alpha_n r^n + \beta_n r^{-n}) \sin n\theta + (\gamma_n r^n + \delta_n r^{-n}) \cos n\theta] . \quad (2.33)$$

Though we skip the details here, it can be shown using the appropriate boundary conditions that the simplest solution of the form (2.33) is

$$\Phi = \beta_1 r^{-1} \sin \theta , \quad (2.34)$$

so that combining Equations (2.31) and (2.34) gives

$$\left( \frac{\partial^2}{\partial r^2} + \frac{1}{r} \frac{\partial}{\partial r} + \frac{1}{r^2} \frac{\partial^2}{\partial \theta^2} \right) \Psi = \beta_1 r^{-1} \sin \theta . \quad (2.35)$$

A solution of the above equation is

$$\Psi = \frac{\beta_1}{2} r \sin \theta \ln r . \quad (2.36)$$

With the requirement that a complete circuit around the dislocation must yield a displacement of  $b$  along the  $x_1$ -direction, we find that

$$\beta_1 = -\frac{\mu b}{\pi(1-\nu)} .$$

Therefore, the solution of the biharmonic Equation (2.20) for the edge dislocation is

$$\Psi = -\frac{\mu b}{2\pi(1-\nu)} r \sin \theta \ln r. \quad (2.37)$$

The nonzero components of the stress tensor follow as [19, 26, 35, 44]

$$\sigma_{rr} = \frac{1}{r^2} \frac{\partial^2 \Psi}{\partial \theta^2} + \frac{1}{r} \frac{\partial \Psi}{\partial r} = -\frac{\mu b}{2\pi(1-\nu)} \frac{1}{r} \sin \theta, \quad (2.38a)$$

$$\sigma_{\theta\theta} = \frac{\partial^2 \Psi}{\partial r^2} = -\frac{\mu b}{2\pi(1-\nu)} \frac{1}{r} \sin \theta, \quad (2.38b)$$

$$\sigma_{r\theta} = \sigma_{\theta r} = -\frac{\partial}{\partial r} \left( \frac{1}{r} \frac{\partial \Psi}{\partial \theta} \right) = \frac{\mu b}{2\pi(1-\nu)} \frac{1}{r} \cos \theta, \quad (2.38c)$$

$$\sigma_{zz} = \nu(\sigma_{rr} + \sigma_{\theta\theta}) = -\frac{\mu b}{\pi(1-\nu)} \frac{\nu}{r} \sin \theta. \quad (2.38d)$$

The corresponding strains follow from Hooke's law and the displacements from integration of the strains. The latter are found to be

$$u_r = \frac{b}{2\pi} \left[ -\frac{1-2\nu}{2(1-\nu)} \sin \theta \ln r + \frac{\sin \theta}{4(1-\nu)} + \theta \cos \theta \right], \quad (2.39a)$$

$$u_{\theta\theta} = \frac{b}{2\pi} \left[ -\frac{1-2\nu}{2(1-\nu)} \cos \theta \ln r - \frac{\cos \theta}{4(1-\nu)} - \theta \sin \theta \right]. \quad (2.39b)$$

The equivalent counterparts in cartesian coordinates are

$$\Psi = -\frac{\mu b}{4\pi(1-\nu)} x_2 \ln(x_1^2 + x_2^2), \quad (2.40)$$

$$\sigma_{11} = \Psi_{,22} = -\frac{\mu b}{2\pi(1-\nu)} \frac{x_2(3x_1^2 + x_2^2)}{(x_1^2 + x_2^2)^2}, \quad (2.41a)$$

$$\sigma_{22} = \Psi_{,11} = \frac{\mu b}{2\pi(1-\nu)} \frac{x_2(x_1^2 - x_2^2)}{(x_1^2 + x_2^2)^2}, \quad (2.41b)$$

$$\sigma_{12} = \sigma_{21} = -\Psi_{,12} = \frac{\mu b}{2\pi(1-\nu)} \frac{x_1(x_1^2 - x_2^2)}{(x_1^2 + x_2^2)^2}, \quad (2.41c)$$

$$\sigma_{33} = \nu(\sigma_{11} + \sigma_{22}) = -\frac{\mu b \nu}{\pi(1-\nu)} \frac{x_2}{x_1^2 + x_2^2}, \quad (2.41d)$$

and

$$u_1 = \frac{b}{2\pi} \left[ \tan^{-1} \left( \frac{x_2}{x_1} \right) + \frac{x_1 x_2}{2(1-\nu)(x_1^2 + x_2^2)} \right], \quad (2.42a)$$

$$u_2 = -\frac{b}{2\pi} \left[ \frac{1-2\nu}{4(1-\nu)} \ln(x_1^2 + x_2^2) + \frac{x_1^2 - x_2^2}{4(1-\nu)(x_1^2 + x_2^2)} \right]. \quad (2.42b)$$

- **Strain energy**

For the same reasons as in the screw case, we will compute the elastic energy inside a hollow cylinder of inner radius  $r_0$  and outer radius  $R$  as depicted in Figure 2.7. Using Equation (2.38) and Hooke's law, we find

$$\begin{aligned}
 \frac{W}{L} &= \int_{r_0}^R \int_0^{2\pi} \frac{1}{2} \{ \sigma_{rr} \varepsilon_{rr} + \sigma_{\theta\theta} \varepsilon_{\theta\theta} + \sigma_{r\theta} \varepsilon_{r\theta} + \sigma_{\theta r} \varepsilon_{\theta r} \} r d\theta dr \\
 &= \int_{r_0}^R \int_0^{2\pi} \frac{1}{2} \left\{ \sigma_{rr} \frac{1+\nu}{E} [(1-\nu) \sigma_{rr} - \nu \sigma_{\theta\theta}] \right. \\
 &\quad \left. + \sigma_{\theta\theta} \frac{1+\nu}{E} [(1-\nu) \sigma_{\theta\theta} - \nu \sigma_{rr}] + 2\sigma_{r\theta} \frac{\sigma_{r\theta}}{2\mu} \right\} r d\theta dr \\
 &= \frac{\mu b^2}{4\pi(1-\nu)} \ln \left( \frac{R}{r_0} \right).
 \end{aligned} \tag{2.43}$$

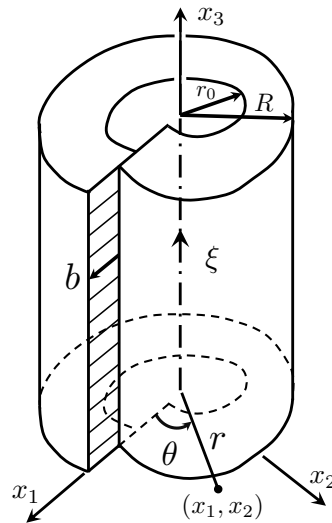


Figure 2.7: Edge dislocation along the positive  $x_3$  axis in a hollow cylinder used to compute the strain energy of the dislocation.

### General straight dislocations

We now turn to the treatment of a general straight dislocation. In doing so, we remember that the Burgers vector of such a dislocation can always be decomposed into edge and screw components—see Figure 2.8.

- **Stress and displacement fields**

Recall from Equation (1.6) that the screw component of the dislocation is

$$\mathbf{b}_s = (\mathbf{b} \cdot \boldsymbol{\xi}) \boldsymbol{\xi},$$

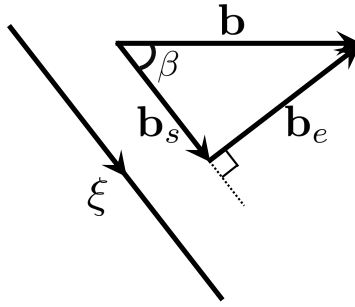


Figure 2.8: Mixed dislocation in an infinite medium with its Burgers vector inclined at an angle  $\beta$  to the dislocation line.

or, in light of Figure 2.8,

$$\mathbf{b}_s = (b \cos \beta) \boldsymbol{\xi}, \quad (2.44)$$

where  $b$  is the magnitude of the Burgers vector  $\mathbf{b}$ .

Thus, the magnitude of the screw component of the Burgers vector is

$$b_s = b \cos \beta \quad (2.45)$$

and, since  $\mathbf{b}_s \perp \mathbf{b}_e$  with  $\mathbf{b} = \mathbf{b}_s + \mathbf{b}_e$ , it follows that

$$b_e = b \sin \beta. \quad (2.46)$$

By the *superposition principle* of linear elasticity [45–51], the elastic field of a mixed dislocation can be obtained by superposition (or addition) of the elastic fields corresponding to the pure edge and pure screw dislocations. Therefore, using Equations (2.26), (2.28), (2.41), and (2.42), the elastic field for the mixed

dislocation along the positive  $x_3$ -axis follows as

$$\sigma_{11} = -\frac{\mu b_e}{2\pi(1-\nu)} \frac{x_2(3x_1^2 + x_2^2)}{(x_1^2 + x_2^2)^2}, \quad (2.47a)$$

$$\sigma_{22} = \frac{\mu b_e}{2\pi(1-\nu)} \frac{x_2(x_1^2 - x_2^2)}{(x_1^2 + x_2^2)^2}, \quad (2.47b)$$

$$\sigma_{33} = -\frac{\mu b_e \nu}{\pi(1-\nu)} \frac{x_2}{x_1^2 + x_2^2}, \quad (2.47c)$$

$$\sigma_{23} = \frac{\mu b_s}{2\pi} \frac{x_1}{x_1^2 + x_2^2}, \quad (2.47d)$$

$$\sigma_{13} = -\frac{\mu b_s}{2\pi} \frac{x_2}{x_1^2 + x_2^2}, \quad (2.47e)$$

$$\sigma_{12} = \frac{\mu b_e}{2\pi(1-\nu)} \frac{x_1(x_1^2 - x_2^2)}{(x_1^2 + x_2^2)^2}, \quad (2.47f)$$

$$u_1 = \frac{b_e}{2\pi} \left[ \tan^{-1} \left( \frac{x_2}{x_1} \right) + \frac{x_1 x_2}{2(1-\nu)(x_1^2 + x_2^2)} \right], \quad (2.48a)$$

$$u_2 = -\frac{b_e}{2\pi} \left[ \frac{1-2\nu}{4(1-\nu)} \ln(x_1^2 + x_2^2) + \frac{x_1^2 - x_2^2}{4(1-\nu)(x_1^2 + x_2^2)} \right], \quad (2.48b)$$

$$u_3 = \frac{b_s}{2\pi} \tan^{-1} \left( \frac{x_2}{x_1} \right), \quad (2.48c)$$

where  $b_s$  and  $b_e$  are given in Equations (2.45) and (2.46).

The corresponding strain components follow from Equation (2.47) and Hooke's law, or by differentiation of the displacements using Equations (2.48) and (2.2).

### • Strain energy

The strain energy of a mixed dislocation can likewise be obtained by adding the respective edge and screw counterparts. As a result, for an infinite hollow cylinder of inner radius  $r_0$  and outer radius  $R$ , the strain energy per unit length of a mixed dislocation along the axis of the cylinder is given by

$$\frac{W}{L} = \frac{\mu b_s^2}{4\pi} \ln \left( \frac{R}{r_0} \right) + \frac{\mu b_e^2}{4\pi(1-\nu)} \ln \left( \frac{R}{r_0} \right),$$

i.e.

$$\frac{W}{L} = \frac{\mu (b \cos \beta)^2}{4\pi} \ln \left( \frac{R}{r_0} \right) + \frac{\mu (b \sin \beta)^2}{4\pi(1-\nu)} \ln \left( \frac{R}{r_0} \right),$$

or

$$\frac{W}{L} = E(\beta) \ln \left( \frac{R}{r_0} \right), \quad (2.49)$$

where  $E(\beta)$  is the so-called *prelogarithmic energy factor* [26] and is given by

$$E(\beta) = \frac{\mu b^2}{4\pi} \left( \cos^2 \beta + \frac{\sin^2 \beta}{1 - \nu} \right). \quad (2.50)$$

## 2.4 Curved Dislocations

So far, our treatment of dislocations has focused only on straight dislocations. However, dislocations as they are observed in metals need not be straight [52, 53]. As a result, we summarize below the continuum theory of dislocations as it pertains to curved dislocations. In doing so, it'll be necessary to review the *Green's tensor* of linear elasticity.

### Green's tensor of linear elasticity

The Green's function method provides a convenient framework to deriving the elastic field of dislocations and point force arrays in arbitrary solids. Indeed, if the response of a body to a point force is known, the deformation caused by any distribution of forces can be obtained by integration [26].

By definition, the Green's function tensor  $G_{ij}(\mathbf{x}, \mathbf{x}')$  is the tensor field that gives the displacement at the point  $\mathbf{x}$  along the  $x_i$ -direction in response to a unit point force applied at the point  $\mathbf{x}'$  along the  $x_j$ -direction [26, 44, 54]. For an infinite homogeneous body, translation invariance requires that [54]

$$G_{ij}(\mathbf{x}, \mathbf{x}') = G_{ij}(\mathbf{x} - \mathbf{x}') = G_{ij}(\mathbf{x}' - \mathbf{x}) = G_{ji}(\mathbf{x} - \mathbf{x}'), \quad (2.51)$$

so that

$$G_{ij,k}(\mathbf{x} - \mathbf{x}') = -G_{ij,k'}(\mathbf{x} - \mathbf{x}') = -G_{ij,k}(\mathbf{x}' - \mathbf{x}), \quad (2.52)$$

and

$$G_{ij,kl}(\mathbf{x} - \mathbf{x}') = G_{ij,k'l'}(\mathbf{x} - \mathbf{x}') = G_{ij,kl}(\mathbf{x}' - \mathbf{x}). \quad (2.53)$$

In Equations (2.52) and (2.53), the unprimed and primed subscripts denote differentiation with respect to  $\mathbf{x}$  and  $\mathbf{x}'$  respectively. In general, analytical solutions for  $G_{ij}$  cannot be found for anisotropic media. However, for the special case of an infinite isotropic solid, a closed form expression for  $G_{ij}$  can be obtained [44, 54].

In deriving the general differential equation for  $G_{ij}$ , we follow the approach of Bacon *et al.* [54] and consider the schematic of Figure 2.9 illustrating a point force  $F_i$  at a point  $\mathbf{x}'$  inside an anisotropic solid.

In light of the definition of the Green's tensor, we have that

$$u_k(\mathbf{x}) = G_{kp}(\mathbf{x} - \mathbf{x}')F_p, \quad (2.54)$$

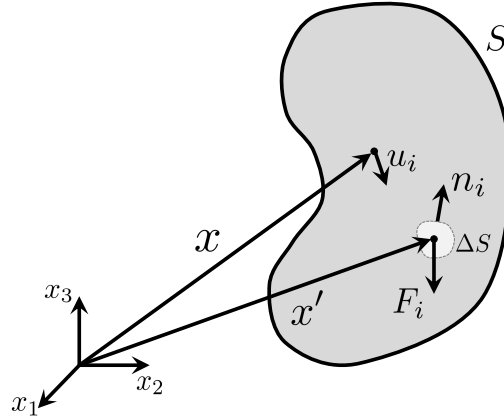


Figure 2.9: Displacement at the point  $\boldsymbol{x}$  due to a point force at  $\boldsymbol{x}'$  inside an anisotropic solid with boundary  $S$ . Here  $\Delta S$  is any surface enclosing  $\boldsymbol{x}'$ .

from which it follows that

$$u_{k,l}(\boldsymbol{x}) = G_{kp,l}(\boldsymbol{x} - \boldsymbol{x}')F_p. \quad (2.55)$$

By Equations (2.9) and (2.2) and the symmetry of the elastic modulus tensor, the corresponding stress state at  $\boldsymbol{x}$  is given by

$$\begin{aligned} \sigma_{ij}(\boldsymbol{x}) &= \frac{1}{2}C_{ijkl}(u_{k,l} + u_{l,k}) \\ &= C_{ijkl}u_{k,l} \\ &= C_{ijkl}G_{kp,l}(\boldsymbol{x} - \boldsymbol{x}')F_p. \end{aligned} \quad (2.56)$$

Thus, in the absence of other sources of stress, the point  $\boldsymbol{x}'$  is in static equilibrium if

$$F_i + \iint_{\Delta S} \sigma_{ij}(\boldsymbol{x})dS_j = 0,$$

i.e., if

$$F_i + \iint_{\Delta S} C_{ijkl}G_{kp,l}(\boldsymbol{x} - \boldsymbol{x}')F_p dS_j = 0, \quad (2.57)$$

where  $\Delta S$  is any surface enclosing the point  $\boldsymbol{x}'$  and we write  $dS_j$  to mean  $n_j dS$ , with  $dS$  being the elemental area and  $\boldsymbol{n}$  the outward normal to the surface  $\Delta S$  as shown in Figure 2.9.

Using the divergence theorem [55–57], Equation (2.57) can be written as

$$F_i + \iiint_{\Delta V} C_{ijkl}G_{kp,lj}(\boldsymbol{x} - \boldsymbol{x}')F_p dV = 0, \quad (2.58)$$

where  $\Delta V$  is the volume enclosed by  $\Delta S$ .

Recalling the sifting property of the Dirac Delta distribution [58–61]

$$\iiint_V f(\mathbf{x})\delta(\mathbf{x} - \mathbf{x}')dV = \begin{cases} f(\mathbf{x}') & \text{if } \mathbf{x} \in V \\ 0 & \text{else.} \end{cases}, \quad (2.59)$$

we can rewrite (2.58) as

$$\iiint_{\Delta V} [F_i\delta(\mathbf{x} - \mathbf{x}') + C_{ijkl}G_{kp,lj}(\mathbf{x} - \mathbf{x}')F_p] dV = 0,$$

or

$$\iiint_{\Delta V} [\delta_{ip}\delta(\mathbf{x} - \mathbf{x}') + C_{ijkl}G_{kp,lj}(\mathbf{x} - \mathbf{x}')] F_p dV = 0. \quad (2.60)$$

Because Equation (2.60) must hold true for any point force  $F_p$ , we arrive at the differential equation for the Green's tensor of linear elasticity, namely

$$C_{ijkl}G_{kp,lj}(\mathbf{x} - \mathbf{x}') + \delta_{ip}\delta(\mathbf{x} - \mathbf{x}') = 0. \quad (2.61)$$

To derive the displacements in terms of the Green's tensor, we notice that using Equation (2.53), we can rewrite Equation (2.61) as

$$C_{ijkl}G_{kp,l'j'}(\mathbf{x} - \mathbf{x}') + \delta_{ip}\delta(\mathbf{x} - \mathbf{x}') = 0. \quad (2.62)$$

On the other hand, static equilibrium—Equation (2.5)—at  $\mathbf{x}'$  can be written in terms of displacements as

$$C_{ijkl}u_{k,l'j'}(\mathbf{x}') + f_i(\mathbf{x}') = 0. \quad (2.63)$$

Next, multiply Equations (2.62) and (2.63) by  $u_i(\mathbf{x}')$  and  $G_{ip}(\mathbf{x} - \mathbf{x}')$  respectively, subtract the resulting expressions, and integrate the difference over any volume  $V$  of the solid containing  $\mathbf{x}$ . The result is

$$\begin{aligned} u_p(\mathbf{x}) &= \iiint_V G_{ip}(\mathbf{x} - \mathbf{x}')f_i(\mathbf{x}')dV' \\ &+ \iiint_V C_{ijkl}G_{ip}(\mathbf{x} - \mathbf{x}')u_{k,l'j'}(\mathbf{x}')dV' \\ &- \iiint_V C_{ijkl}G_{kp,l'j'}(\mathbf{x} - \mathbf{x}')u_i(\mathbf{x}')dV'. \end{aligned}$$

However, using the major symmetry of the modulus tensor, it follows that

$$\begin{aligned} &C_{ijkl} [ G_{ip}(\mathbf{x} - \mathbf{x}')u_{k,l'j'}(\mathbf{x}') - G_{kp,l'j'}(\mathbf{x} - \mathbf{x}')u_i(\mathbf{x}') ] \\ &= C_{ijkl} [ G_{ip}(\mathbf{x} - \mathbf{x}')u_{k,l'}(\mathbf{x}') - G_{kp,l'}(\mathbf{x} - \mathbf{x}')u_i(\mathbf{x}') ]_{,j'} \end{aligned}$$

and so

$$\begin{aligned}
 u_p(\mathbf{x}) &= \iiint_V G_{ip}(\mathbf{x} - \mathbf{x}') f_i(\mathbf{x}') dV' \\
 &+ \iiint_V C_{ijkl} [G_{ip}(\mathbf{x} - \mathbf{x}') u_{k,l'}(\mathbf{x}')]_{,j'} dV' \\
 &- \iiint_V C_{ijkl} [G_{kp,l'}(\mathbf{x} - \mathbf{x}') u_i(\mathbf{x}')]_{,j'} dV'.
 \end{aligned}$$

Assuming that the integrands and their derivatives are continuous and single-valued, one can apply the divergence theorem to obtain

$$\begin{aligned}
 u_p(\mathbf{x}) &= \iiint_V G_{ip}(\mathbf{x} - \mathbf{x}') f_i(\mathbf{x}') dV' \\
 &+ \oint_S C_{ijkl} G_{ip}(\mathbf{x} - \mathbf{x}') u_{k,l'}(\mathbf{x}') dS'_j \\
 &- \oint_S C_{ijkl} G_{kp,l'}(\mathbf{x} - \mathbf{x}') u_i(\mathbf{x}') dS'_j,
 \end{aligned} \tag{2.64}$$

where  $S$  is the surface enclosing the volume  $V$ .

For an infinite homogeneous body, the surface integrals may be assumed to vanish at infinity. We get

$$u_p(\mathbf{x}) = \iiint_V G_{ip}(\mathbf{x} - \mathbf{x}') f_i(\mathbf{x}') dV'.$$

Furthermore, using translation invariance of the Green's tensor as given through Equation (2.51), the displacement equation simplifies to

$$u_p(\mathbf{x}) = \iiint_V G_{pi}(\mathbf{x} - \mathbf{x}') f_i(\mathbf{x}') dV'. \tag{2.65}$$

### Stress and displacement fields

We now make use of Equation (2.64) to derive the elastic field of a curved dislocation line in an infinite solid. In Figure 2.10,  $S_0$  is any area bounded by the dislocation  $L$ , with outward normal as shown. Though we assume that the dislocation lies in an infinite solid, we use Equation (2.64) instead of Equation (2.65) because introducing the dislocation creates a discontinuity in the displacements—see Equation (2.1)—and as a result, the divergence theorem cannot be applied. Thus, it is necessary to consider a volume  $V$  within which the integrands of Equation (2.64) are differentiable and single-valued. To this end, we consider the domain consisting of the entire space except for a volume around the dislocation bounded

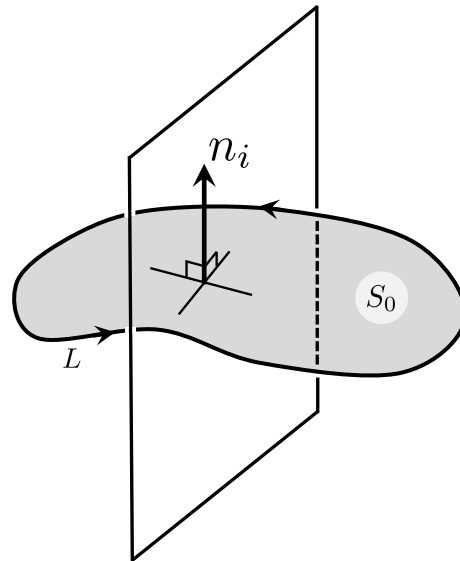


Figure 2.10: Schematic of a (closed) curved dislocation  $L$  in an infinite solid.  $S_0$  is an arbitrary surface bounded by the dislocation.

by the tubular region of radius  $r_0$  and the surfaces  $S_0^+$  and  $S_0^-$  across which the displacements  $u_i$  changes discontinuously by  $b_i$ . This is illustrated in Figure (2.11), which is the front view of the cross-section shown in Figure (2.10).

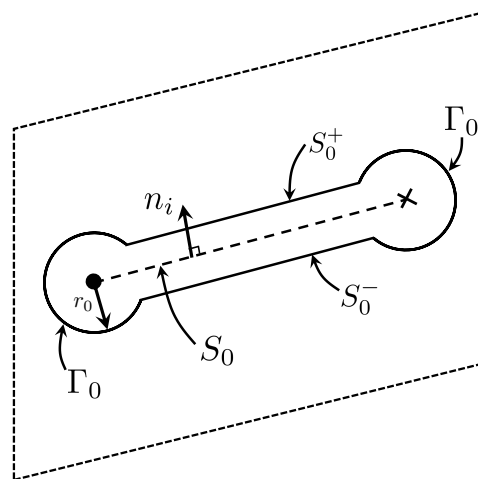


Figure 2.11: Schematic of the surface cap used for determination of the displacement field of a curved dislocation. The cap consists of the cut faces  $S_0^-$  and  $S_0^+$  and a tubular surface,  $\Gamma_0$ , of radius  $r_0$  centered around the dislocation line.

Assuming no body forces in the infinite solid, the displacement field in the region

outside the cap is continuous, and as a result we can use Equation (2.64) to write the displacement due to the dislocation as

$$\begin{aligned} u_p(\mathbf{x}) = & \iint_{S_0^-} C_{ijkl} G_{ip}(\mathbf{x} - \mathbf{x}') u_{k,l'}(\mathbf{x}') dS'_j - \iint_{S_0^-} C_{ijkl} G_{kp,l'}(\mathbf{x} - \mathbf{x}') u_i(\mathbf{x}') dS'_j \\ & + \iint_{S_0^+} C_{ijkl} G_{ip}(\mathbf{x} - \mathbf{x}') u_{k,l'}(\mathbf{x}') dS'_j - \iint_{S_0^+} C_{ijkl} G_{kp,l'}(\mathbf{x} - \mathbf{x}') u_i(\mathbf{x}') dS'_j \\ & + \iint_{\Gamma_0} C_{ijkl} G_{ip}(\mathbf{x} - \mathbf{x}') u_{k,l'}(\mathbf{x}') dS'_j - \iint_{\Gamma_0} C_{ijkl} G_{kp,l'}(\mathbf{x} - \mathbf{x}') u_i(\mathbf{x}') dS'_j. \end{aligned}$$

Since the dislocation deformation and the Green's tensor satisfy the same homogeneous boundary conditions, it can be argued—see [44, 54]—that the contribution from the tubular region vanishes in the limit  $r_0 \rightarrow 0$ . We get

$$\begin{aligned} u_p(\mathbf{x}) = & \iint_{S_0^-} C_{ijkl} G_{ip}(\mathbf{x} - \mathbf{x}') u_{k,l'}(\mathbf{x}') dS'_j - \iint_{S_0^-} C_{ijkl} G_{kp,l'}(\mathbf{x} - \mathbf{x}') u_i(\mathbf{x}') dS'_j \\ & + \iint_{S_0^+} C_{ijkl} G_{ip}(\mathbf{x} - \mathbf{x}') u_{k,l'}(\mathbf{x}') dS'_j - \iint_{S_0^+} C_{ijkl} G_{kp,l'}(\mathbf{x} - \mathbf{x}') u_i(\mathbf{x}') dS'_j. \end{aligned}$$

As  $r_0 \rightarrow 0$ , the cut surfaces  $S_0^-$  and  $S_0^+$  collapse onto  $S_0$ . Since the integrand in the first surface integral of Equation (2.64) is continuous across  $S_0$ , and given that the outward normal of the surfaces  $S_0^+$  and  $S_0^-$  are exact opposite, it follows that

$$\iint_{S_0^-} C_{ijkl} G_{ip}(\mathbf{x} - \mathbf{x}') u_{k,l'}(\mathbf{x}') dS'_j + \iint_{S_0^+} C_{ijkl} G_{ip}(\mathbf{x} - \mathbf{x}') u_{k,l'}(\mathbf{x}') dS'_j = 0$$

in the limit  $r_0 \rightarrow 0$ . As such, we have

$$\begin{aligned} u_p(\mathbf{x}) = & - \iint_{S_0^-} C_{ijkl} G_{kp,l'}(\mathbf{x} - \mathbf{x}') u_i(\mathbf{x}') n_j dS' \\ & + \iint_{S_0^+} C_{ijkl} G_{kp,l'}(\mathbf{x} - \mathbf{x}') u_i(\mathbf{x}') n_j dS' \\ = & -C_{ijkl} \left[ \iint_{S_0^-} u_i(\mathbf{x}') G_{kp,l'}(\mathbf{x} - \mathbf{x}') n_j dS' \right. \\ & \left. - \iint_{S_0^+} u_i(\mathbf{x}') G_{kp,l'}(\mathbf{x} - \mathbf{x}') n_j dS' \right], \end{aligned}$$

where the outward normal vector  $n_j$  is that of the surface  $S_0$ , which is the same as that of  $S_0^-$  and the opposite of that of  $S_0^+$ .

In the limit  $r_0 \rightarrow 0$ , i.e. as the surfaces  $S_0^-$  and  $S_0^+$  collapse on  $S_0$ , the relative displacement of  $S_0^-$  with respect to  $S_0^+$  is  $u_i(S_0^-) - u_i(S_0^+) = b_i$ . It follows that

$$u_p(\mathbf{x}) = -C_{ijkl} b_i \iint_{S_0} G_{kp,l'}(\mathbf{x} - \mathbf{x}') dS'_j. \quad (2.66)$$

This is known as *Volterra's equation* for the displacement field of a dislocation in an infinite medium as a function of the Green's tensor [26, 43, 44, 54, 62].

The distortions follow from differentiation of the displacements as

$$u_{p,q}(\mathbf{x}) = -b_i C_{ijkl} \iint_{S_0} G_{kp,l'q}(\mathbf{x} - \mathbf{x}') dS'_j.$$

However, using Equations (2.52) and (2.53), this becomes

$$u_{p,q}(\mathbf{x}) = b_i C_{ijkl} \iint_{S_0} G_{kp,l'q'}(\mathbf{x} - \mathbf{x}') dS'_j. \quad (2.67)$$

The strains and stresses then follow easily from Equations (2.2) and (2.9). We would like to emphasize that the surface  $S_0$  in the above equations is any arbitrary surface bounded the dislocation line  $L$ . By a judicious application of Stockes' theorem [55–57], Mura [62] showed that (2.67) can be written as line integral, viz.

$$u_{p,q}(\mathbf{x}) = -b_i C_{ijkl} \epsilon_{rjq} \oint_L G_{kp,l}(\mathbf{x} - \mathbf{x}') dx'_r, \quad (2.68)$$

so that

$$\sigma_{mn}(\mathbf{x}) = C_{mnpq} u_{p,q}(\mathbf{x}) = -b_i C_{mnpq} C_{ijkl} \epsilon_{rjq} \oint_L G_{kp,l}(\mathbf{x} - \mathbf{x}') dx'_r, \quad (2.69)$$

where

$$\epsilon_{ijk} = \begin{cases} 1 & \text{if } (i, j, k) \text{ is an even permutation of } (1, 2, 3), \\ -1 & \text{if } (i, j, k) \text{ is an odd permutation of } (1, 2, 3), \\ 0 & \text{else.} \end{cases}$$

In other words, the stress field does not depend on the surface  $S_0$  but only on the dislocation line  $L$ .

In principle, Equations (2.66) and (2.68) are valid for arbitrary infinite anisotropic media. However, in practice, their use is often limited to isotropic materials as the Green's tensor for a general anisotropic solid cannot be obtained analytically. For isotropic solids, we have [26, 43, 44, 54, 63]

$$G_{ij}(\mathbf{x} - \mathbf{x}') = \frac{1}{8\pi\mu|\mathbf{x} - \mathbf{x}'|} \left[ 2\delta_{ij} - \frac{\delta_{ij} - T_i T_j}{2(1 - \nu)} \right], \quad (2.70)$$

where

$$T_i = \frac{x_i - x'_i}{|\mathbf{x} - \mathbf{x}'|}.$$

In this case, the displacements and stresses take the following forms, known respectively as Burgers' equation [64] and Peach-Koehler stress formula [65]:

$$u_m(\mathbf{x}) = -\frac{b_m}{4\pi} \iint_{S_0} \frac{\partial}{\partial x'_j} \left( \frac{1}{R} \right) dS_j - \frac{b_i}{4\pi} \oint_L \epsilon_{mik} \frac{1}{R} dx'_k - \frac{b_i}{8\pi(1-\nu)} \oint_L \epsilon_{ijk} \frac{\partial^2 R}{\partial x'_m \partial x'_j} dx'_k \quad (2.71)$$

and

$$\sigma_{\alpha\beta}(\mathbf{x}) = -\frac{\mu}{4\pi} \oint_L b_m \epsilon_{im\alpha} \frac{\partial}{\partial x'_i} \left( \frac{1}{R} \right) dx'_\beta - \frac{\mu}{4\pi} \oint_L b_m \epsilon_{im\beta} \frac{\partial}{\partial x'_i} \left( \frac{1}{R} \right) dx'_\alpha - \frac{\mu}{4\pi(1-\nu)} \oint_L b_m \epsilon_{imk} \left[ \frac{\partial^3 R}{\partial x'_i \partial x'_\alpha \partial x'_\beta} - 2\delta_{\alpha\beta} \frac{\partial}{\partial x'_i} \left( \frac{1}{R} \right) \right] dx'_k, \quad (2.72)$$

where

$$R = |\mathbf{x} - \mathbf{x}'|.$$

### Strain energy of a dislocation loop

In order to derive the strain energy of a curved dislocation, we consider the more general case of the interaction energy between two dislocation loops. As such, we consider the dislocations lines  $L_1$  and  $L_2$  and the arbitrary areas  $S_1$  and  $S_2$  that they respectively enclose—see Figure 2.12.

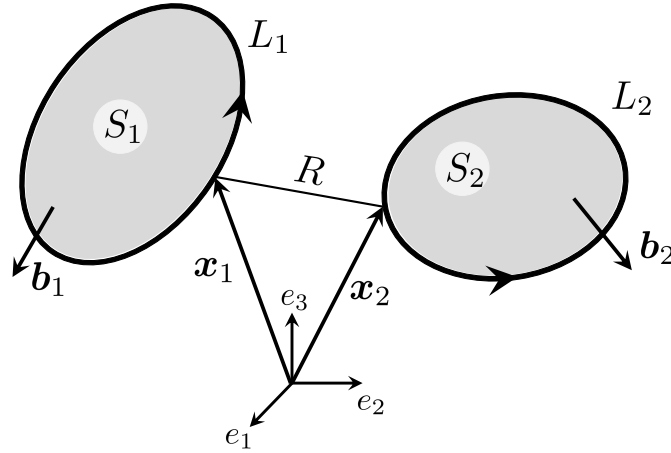


Figure 2.12: Schematic of two dislocation loops within an infinite elastic continuum.

Following Hirth and Lothe [26], the interaction energy between the two dislocations is given by

$$W_{12} = \iint_{S_1} b_{1\alpha} \sigma_{2\alpha\beta}(\mathbf{x}_1) dS_{1\beta}, \quad (2.73)$$

where

- ◇  $b_{1\alpha}$  is the  $\alpha$ -component of the Burgers vector  $\mathbf{b}_1$  of the dislocation  $L_1$ ,
- ◇  $\sigma_{2\alpha\beta}(\mathbf{x}_1)$  is the  $\alpha\beta$ -component of the stress tensor at the point  $\mathbf{x}_1$  on the dislocation  $L_1$  due to the dislocation  $L_2$ , and
- ◇  $dS_{1\beta}$  is the  $\beta$ -component of the elemental area of the arbitrary surface  $S_1$  enclosed by the dislocation  $L_1$ .

Not surprisingly, this can also be expressed as

$$W_{12} = \iint_{S_1} b_{2\alpha} \sigma_{1\alpha\beta}(\mathbf{x}_2) dS_{2\beta},$$

with the variables  $b_{2\alpha}$ ,  $\sigma_{1\alpha\beta}(\mathbf{x}_2)$ , and  $dS_{2\beta}$  defined similarly as above.

Inserting Equation (2.72) into (2.73) while noting that  $\partial R/\partial x_{1i} = -\partial R/\partial x_{2i}$ , where now  $R = |\mathbf{x}_1 - \mathbf{x}_2|$ , we get

$$\begin{aligned} W_{12} = & \frac{\mu}{4\pi} \iint_{S_1} \oint_{L_2} b_{1\alpha} b_{2m} \epsilon_{im\alpha} \frac{\partial}{\partial x_{1i}} \left( \frac{1}{R} \right) dx_{2\beta} dS_{1\beta} \\ & + \frac{\mu}{4\pi} \iint_{S_1} \oint_{L_2} b_{1\alpha} b_{2m} \epsilon_{im\beta} \frac{\partial}{\partial x_{1i}} \left( \frac{1}{R} \right) dx_{2\alpha} dS_{1\beta} \\ & + \frac{\mu}{4\pi(1-\nu)} \iint_{S_1} \oint_{L_2} b_{1\alpha} b_{2m} \epsilon_{imk} \frac{\partial^3 R}{\partial x_{1i} \partial x_{1\alpha} \partial x_{1\beta}} dx_{2k} dS_{1\beta} \\ & - \frac{\mu}{2\pi(1-\nu)} \iint_{S_1} \oint_{L_2} b_{1\alpha} b_{2m} \epsilon_{imk} \delta_{\alpha\beta} \frac{\partial}{\partial x_{1i}} \left( \frac{1}{R} \right) dx_{2k} dS_{1\beta}. \end{aligned} \quad (2.74)$$

Though we do not include the details here, one can use Stokes' theorem to simplify the above expression. We obtain [26, 42]

$$\begin{aligned} W_{12} = & -\frac{\mu}{2\pi} \oint_{L_1} \oint_{L_2} \frac{(\mathbf{b}_1 \times \mathbf{b}_2) \cdot (\mathbf{dl}_1 \times \mathbf{dl}_2)}{R} + \frac{\mu}{4\pi} \oint_{L_1} \oint_{L_2} \frac{(\mathbf{b}_1 \cdot \mathbf{dl}_1)(\mathbf{b}_2 \cdot \mathbf{dl}_2)}{R} \\ & + \frac{\mu}{4\pi(1-\nu)} \oint_{L_1} \oint_{L_2} (\mathbf{b}_1 \times \mathbf{dl}_1) \cdot \mathbf{T} \cdot (\mathbf{b}_2 \times \mathbf{dl}_2), \end{aligned} \quad (2.75)$$

where

$$T_{ij} = \frac{\partial^2 R}{\partial x_{1i} \partial x_{1j}} = \frac{\partial^2 R}{\partial x_{2i} \partial x_{2j}}$$

as the order of differentiation does not matter in this case.

The strain energy of a single dislocation loop  $L$  can now be obtained as the limiting case of the above result by setting  $L_1 = L_2$  and dividing the result by 2 [26, 44]. We get

$$W_s = \frac{\mu}{8\pi} \oint_{L_1=L} \oint_{L_2=L} \frac{(\mathbf{b} \cdot d\mathbf{l}_1)(\mathbf{b} \cdot d\mathbf{l}_2)}{R} + \frac{\mu}{8\pi(1-\nu)} \oint_{L_1=L} \oint_{L_2=L} (\mathbf{b} \times d\mathbf{l}_1) \cdot \mathbf{T} \cdot (\mathbf{b} \times d\mathbf{l}_2), \quad (2.76)$$

where  $R$  is the distance between two points on the dislocation—see Figure 2.13.

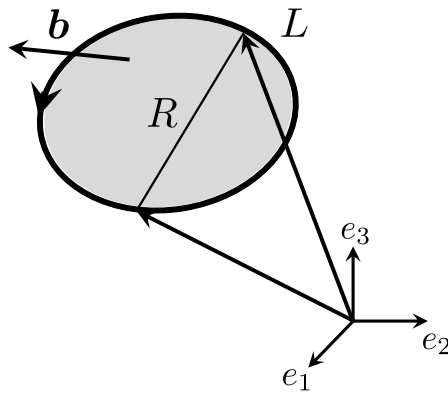


Figure 2.13: Schematic of a dislocation loop within an infinite elastic continuum.

As written, the dislocation self-energy  $W_s$  diverges. This is the same problem that led to the use of a hollow cylinder when computing the strain energy of straight dislocations. However, the use of a hollow core for general curved dislocations increases the complexity of the problem as it would require a knowledge of the Green's function for the region outside the dislocation core [44]. We will return to this discussion in Section 2.5.

## 2.5 Forces on a Dislocation

The notion of force on a dislocation is one of configurational forces, i.e. one defined as the variation (in the derivative sense) of the energy (or work) of a solid with respect to the position of the configuration. This force should not be confused with the notion of force on a mass as the former is, in a sense, fictitious and introduced to give a description of energy changes in a solid [20, 26, 54, 66, 67]. As such, the force on a dislocation is the variation of the energy of the host medium with respect to the position of the dislocation. In what follows, it will be important to

distinguish between forces due to external stresses, those due to internal stresses, and those due to the self-stress of the dislocation.

### Forces due to external stresses

Consider a dislocation loop in an elastic medium and let  $\sigma$  be the stress field due to applied tractions at the boundary of the solid. As the dislocation is created, the work done by the applied tractions  $\sigma$  is [26, 42] is

$$W = \int_{S_0} -b_i \sigma_{ij} dS_j, \quad (2.77)$$

where, as before,  $S_0$  is the area enclosed by the dislocation line.

Next, suppose that an element of line  $d\mathbf{l}$  of the dislocation moves by an amount  $d\mathbf{x}$ —see Figure 2.14. Then the area  $S_0$  increases by  $\delta S_0 = d\mathbf{x} \times d\mathbf{l}$  and as a result, the applied tractions do additional work:

$$\begin{aligned} \delta W &= -b_i \sigma_{ij} \delta S_{0j} \\ &= -b_i \sigma_{ij} \epsilon_{jmn} dx_m dl_n \\ &= (-\sigma_{ji} b_i \epsilon_{jmn} dl_n) dx_m \\ &= (\epsilon_{mjn} \sigma_{ji} b_i dl_n) dx_m. \end{aligned} \quad (2.78)$$

However, denoting by  $d\mathbf{F}$  the configurational force on the element  $d\mathbf{l}$  of the dislocation, we must also have that

$$\delta W = dF_m dx_m. \quad (2.79)$$

Since the element  $d\mathbf{l}$  and the virtual displacement  $d\mathbf{x}$  were chosen randomly,

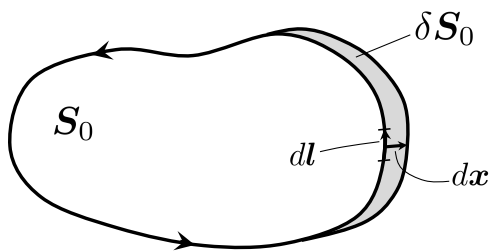


Figure 2.14: An element  $d\mathbf{l}$  of dislocation line moves a distance  $d\mathbf{x}$ , thus increasing the area swept by the dislocation by the amount  $\delta S_0 = d\mathbf{x} \times d\mathbf{l}$ .

comparing Equations (2.78) and (2.79) implies that the force on the element  $d\mathbf{l}$  is given by

$$dF_m = \epsilon_{mjn} \sigma_{ji} b_i dl_n. \quad (2.80)$$

In vector notation, Equation (2.80) becomes

$$d\mathbf{F} = (\boldsymbol{\sigma}\mathbf{b}) \times d\mathbf{l}. \quad (2.81)$$

Equation (2.81) (or, equivalently, Equation (2.80)) is known as the Peach-Koehler formula for the force on a dislocation, owing to Peach and Koehler [65] who first derived it in 1950. In Equation (2.80), the stress field  $\boldsymbol{\sigma}$  is to be evaluated at the element of dislocation line  $d\mathbf{l}$ .

### Forces due to internal stresses

Internal stresses in a solid with a dislocation can be understood as those stresses due to other imperfections inside the solid resulting in traction-free state at the external surfaces [20]. These could be due to other dislocations or point defects.

Following a derivation similar to the above, it can be shown [54] that the force on the dislocation due to other sources of internal stress also assumes the form given in Equation (2.81). More specifically, a dislocation in a solid with other sources of internal stress experiences a force

$$d\mathbf{F} = (\boldsymbol{\sigma}^O\mathbf{b}) \times d\mathbf{l}, \quad (2.82)$$

where now  $\boldsymbol{\sigma}^O$  is the stress field due to the internal sources.

For our purposes, the image stresses due to the dislocation are also considered to be of the internal type. These are stresses induced by the fact that the dislocation may be in a bounded—rather than infinite—medium [68] and are illustrated with the help of Figure 2.15. When it comes to their effect on a dislocation, Gavazza [69, 70] was the first to rigourously prove that the force they create can also be written using the Peach-Koehler formula, viz.

$$d\mathbf{F} = (\boldsymbol{\sigma}^I\mathbf{b}) \times d\mathbf{l}, \quad (2.83)$$

where  $\boldsymbol{\sigma}^I$  is the image stress field of the dislocation.

### Self-force of a dislocation

In the following, we use the notion of *self-force* to mean the force on a dislocation due to its own elastic field in an infinite medium. The resulting stress, also known as the self-stress of the dislocation, is given by Equation (2.69), which is repeated below for convenience:

$$\sigma_{mn}(\mathbf{x}) = C_{mnpq}u_{p,q}(\mathbf{x}) = -b_i C_{mnpq} C_{ijkl} \epsilon_{rjq} \oint_L G_{kp,l}(\mathbf{x} - \mathbf{x}') dx'_r.$$

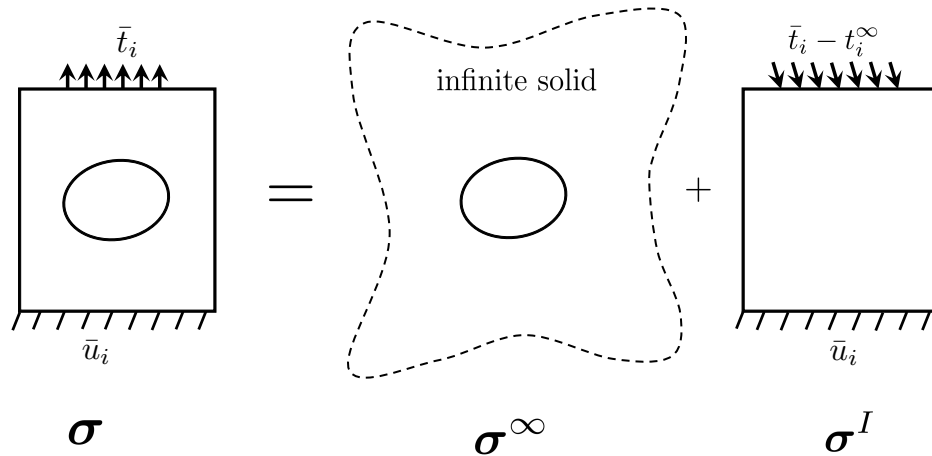


Figure 2.15: Principle of superposition used to define the image stress in a bounded solid with a dislocation [71, 72].  $\sigma$  corresponds to the stress in the finite dislocated solid as shown on the left.  $\sigma^\infty$  corresponds to the stress in the infinite dislocated solid. This creates tractions  $t_i^\infty$  at the boundary that would delimit the real finite solid. Finally,  $\sigma^I$  is the image stress in the finite solid free of dislocations. Note the traction boundary conditions used in this case.

Inevitably, the self-stress diverges along the dislocation line. Therefore, it cannot be used in the Peach-Koehler formula to compute the self-force on the dislocation. Still, in an attempt to quantify the self-force on a dislocation, researchers haven't taken various approaches to *regularize* the self-stress along the dislocation line. Beyond suggesting yet another such approach, the work of Cai *et al.* [73] gives an excellent review of previous attempts to remove this singularity in the continuum theory of dislocations. A few of them are summarized below.

In reference [74], Brown describes an approach where the self-stress at a point  $x$  along the dislocation is evaluated as the average of those at points  $x \pm \epsilon \mathbf{m}$ , where  $\epsilon$  can be taken to be the core parameter and  $\mathbf{m}$  is the in-plane normal to the dislocation at  $x$ —see Figure 2.16.

In the approach of Gavazza and Barnett [68], a tubular region around the dislocation similar to Figure 2.11 is removed and the elastic energy is computed using the volume outside this region. The resulting self-force is then approximated as the variation of the energy. However, this method is restrictive in that it applies only to planar dislocations.

Hirth and Lothe [26] on the other hand suggest a regularization where the self-stress at a point  $x$  along the dislocation is computed using Equation (2.69), but with the

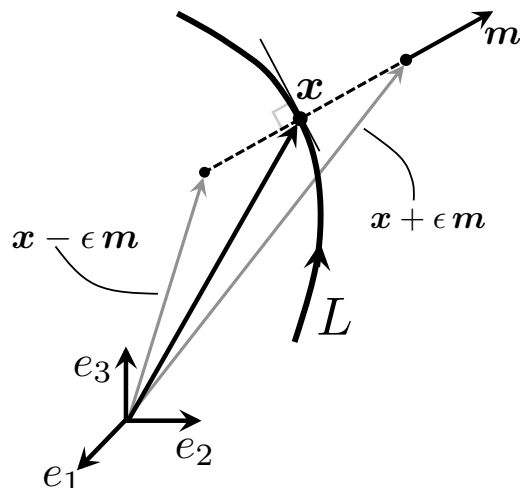


Figure 2.16: Illustration of the core regularization proposed by Brown [74] in 1964. The self-stress at  $\boldsymbol{x}$  is computed as the average of those at  $\boldsymbol{x} \pm \epsilon \boldsymbol{m}$ , where  $\boldsymbol{m}$  is the in-plane normal to the dislocation at  $\boldsymbol{x}$ .

added constraint that the integral be set to zero for points  $\boldsymbol{x}'$  lying within a radius  $\epsilon$  of  $\boldsymbol{x}$ . For the illustration of Figure 2.17, this means that the self-stress at  $\boldsymbol{x}$  is approximated as

$$\sigma_{mn}(\boldsymbol{x}) = C_{mnpq}u_{p,q}(\boldsymbol{x}) \approx -b_i C_{mnpq} C_{ijkl} \epsilon_{rjq} \int_{A \rightarrow B} G_{kp,l}(\boldsymbol{x} - \boldsymbol{x}') dx'_r, \quad (2.84)$$

where the integral is taken along the open contour  $A \rightarrow B$  along  $L$ .

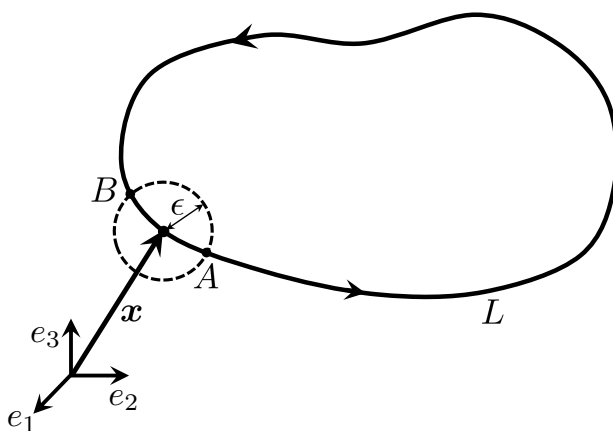


Figure 2.17: Illustration of the core regularization proposed by Hirth and Lothe [26]. The self-stress at  $\boldsymbol{x}$  is computed using Equation (2.69) but excluding those points  $\boldsymbol{x}'$  that are a distance less than  $\epsilon$  away from  $\boldsymbol{x}$ .

Finally, in the approach of Cai *et al.* [73], the Burgers vector is spread isotropically within the core—as opposed to being concentrated on the dislocation line—using a

spreading function characterized by a single parameter which they call the spreading radius. This parameter essentially plays the same role as the dislocation core radius.

The current work uses yet another regularization of the dislocation core. The details are given in Chapter 3 as part of the method of monopoles for dislocation dynamics.

## Chapter 3

### A METHOD OF MONOPOLES FOR DISLOCATION DYNAMICS

Note: Significant content of this chapter is taken from the work of Deffo, Ariza, and Ortiz [75].

#### 3.1 Introduction

The plastic deformation of crystals is the macroscopic effect of the cooperative motion of large ensembles of lattice dislocations. From a geometric point of view, dislocations are line-like lattice defects that demarcate the boundary of areas of constant crystallographic slip on slip planes. By the discrete nature of crystal lattices, crystallographic slip is in turn constrained to occur in quanta of Burgers vector and, therefore, the dislocation lines carry a quantized Burgers vector 'charge'. Since dislocations are boundaries, they must themselves have no boundary, i.e., they must form closed loops, branch according to Frank's rule or terminate at the boundary of the solid. The motion of dislocation is driven by the Peach-Koehler force induced by the applied stresses and by the elastic interaction between dislocations and is controlled by dislocation mobility. As they move, dislocations may undergo line stretching, pair annihilation, dislocation reactions, pinning-depinning interactions, and other complex geometrical and topological transitions.

Given their fundamental role as agents of plastic deformation, dislocations have been extensively studied both experimentally, analytically and computationally. This chapter contributes to this study by proposing an innovative approach to dislocation dynamics simulations. However, before giving the details of this new theory, previous attempts at the long lasting problem of dislocation dynamics simulation stand a brief review.

#### 3.2 Previous Approaches to Dislocation Dynamics

Though new methods for dislocation dynamics have recently been proposed (cf., e.g., the level-set method of [76]), previous attempts can be categorized into two classes: the line dislocation dynamics method and the phase field approach.

The line approach to dislocation dynamics simulations can usually be summarized as follows [40, 77]:

1. Discretize the dislocation lines using an adequate scheme—typically connected line segments;
2. Compute the Peach-Koehler forces along the dislocation elements using continuum linear elasticity—for the forces due to applied external stresses and other sources of internal stresses as described in Section 2.5—and an appropriate core regularization scheme—for the forces due to the self-stress of the dislocation element, also described in Section 2.5;
3. Evolve the dislocation elements using an appropriate mobility law;
4. Compute the resulting plastic deformation;
5. Apply complex rules to account for short-range segment-segment interactions, dislocation reactions, and topological transitions;
6. Go back to step 2 above and repeat until the total simulation time is reached.

Within this description, the overall dislocation structure is characterized by a set of nodes (or segments) and a data structure defining the connectivity between them [78]. This is known as the *line dislocation dynamics method*. Across the major dislocation dynamics codes, the discretization can be performed in two different manners which lead to two families of dislocation dynamics simulations [78, 79].

### Lattice-based simulations

In the initial version of lattice-based codes, all dislocations are discretized into a collection of edge and screw segments. In recent developments, however, curved dislocations are discretized into a succession of straight segments—not necessarily of edge or screw type—which are positioned on preset directions of an underlying cubic lattice such that the length of each segment is a multiple of the lattice parameter [79, 80]. Because the segment extremities coincide with lattice points, a finite set of dislocation orientations is selected and only these orientations are considered. Dislocation motion is considered only in the direction orthogonal to each of these segments [78, 80]. This is illustrated in Figure 3.1 where the dislocation line and the corresponding lattice-based discretization are shown in black and red respectively. During simulations, the integration points at which the Peach-Koehler force is calculated are usually taken to be the middle of segments. However, sometimes the integration points have to be moved to other locations for ease of computing of the Peach-Koehler force [80]. Examples of dislocation

dynamics codes using this discretization scheme include *Tridis* and *microMegas* [79]. For further reading on lattice-based simulations, the reader is referred to [80, 81] and the references therein.

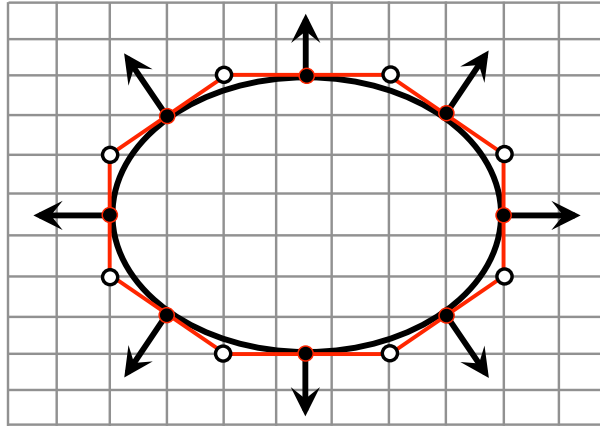


Figure 3.1: Discretization of a curved dislocation into line segments (in red) in lattice-based simulations. The integration points are taken as the middles of the segments. The outward arrows indicate the only possible directions of motion of the segments.

### Nodal simulations

In node-based simulations, the dislocations are represented by a set of nodes positioned on the dislocation lines, and shape functions are used to connect consecutive nodes. Though the simplest and most commonly used shape functions are the linear type, resulting in straight line segments [78] (see Figure 3.2), cubic splines have also been used—for example in the *PDD* code of Ghoniem *et al.* which is detailed in [82]. There is no need to restrict the discretization to a collection of edge and screw segments as any dislocation orientation is allowed. The segments are only submitted to the condition of conservation of Burgers vector at the nodes—see Figure 1.13 and Equation 1.4. Furthermore, the motion of the nodes is not restricted to specified directions. Rather, dislocation segments can move in any direction consistent with their mobility law [78]. However, because the nodes are located on the dislocation lines, computing the Peach-Koehler force requires regularization of the elastic energy and stress expressions. In the nodal code *ParaDiS* [83], the core regularization of Cai *et al.* [73] is used to that effect. Reference [72] and Chapter 10 of [40] give a more detailed description of line dislocation dynamics using nodal representation.

In dislocation dynamics simulations, each of the above discretizations has its

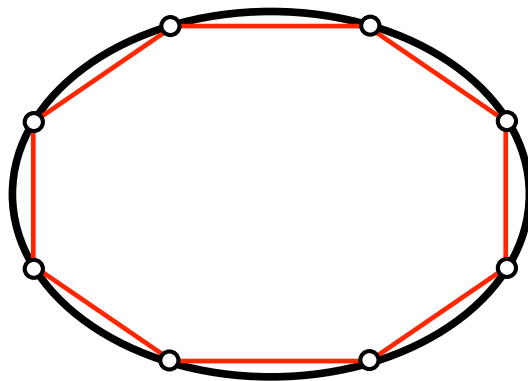


Figure 3.2: Discretization of a curved dislocation into line segments (in red) in nodal simulations.

advantages in terms of accuracy, computing efficiency, simplicity, and flexibility. In lattice-based simulations, since the segments extremities coincide with lattice points, force calculations are simplified as the finite number of segment directions allows tabulating parts of the stress field computations [80]. On the other hand, with node-based simulations, the discretization generally gives smoother representations of the dislocation line. This is because the dislocation segments can take any shape, thus resulting in a more accurate representation of the dislocation. However, despite these advantages, line dislocation dynamics simulations still suffer from challenges associated with large scale 3D simulations, the first of which is the computational cost [77]. It is well known that for a simulation volume containing  $N$  segments, the cost for the nodal force computations scales as  $\mathcal{O}(N^2)$  [79, 80]. As a result, researchers have taken various approaches to reducing this computational overhead.

One such venue is the use of the *Fast Multipole Method (FMM)* [84, 85] and the derivative works thereof [86, 87]. Application of this method in dislocation dynamics is detailed in references [88, 89]. Despite the improvements provided by the FMM in dislocation dynamics, the cost of nodal force computations is further compounded by the fact that one needs to keep track of the connectivity of the segments (or nodes) at all time. This is especially true during strain hardening where dislocation entanglements lead to complex interactions and connectivities between nodes [90–92].

Furthermore, the simulation time step strongly correlates with the stability, and thus accuracy, of the computations. Indeed, because most line discretization schemes use

explicit methods for time integration of the nodes (cf., e.g., the Euler method and the Euler-trapezoid method used in *microMegas* [80] and *ParaDis* [40] respectively), stability of the algorithm limits the simulation time step to small values. As a result, the number of time steps required to achieve a given total simulation time is larger than in an implicit simulation where the algorithm is unconditionally stable, and thus the time step can be taken to be significantly larger.

The phase field method to dislocation dynamics was born in an attempt to address some of the issues just mentioned. The approach relies on a continuous field of eigenstrains to reveal the locations of dislocations in regions of high strain gradients. Indeed, given that a dislocation is the boundary line between slipped and unslipped areas on a crystal plane, the amount of slip across the plane becomes a natural candidate for the phase field associated with the dislocation [40]—see Chapter 11 of [40] and the references therein as well as the paper by Koslowski *et al.* [93] for an overview of the method. A significant advantage of this method stems from the fact that no specialized treatment of topological changes is required [40, 77] as the method seamlessly accounts for these phenomena. As a result, the implementation is more straightforward when compared to line dislocation dynamics. Nevertheless, because the equations are solved on a grid, features smaller than the grid spacing cannot be resolved. As a result, short range dislocation interactions cannot be modeled accurately on a grid without a very fine grid spacing [77]. However, this would make large-scale 3D simulations computationally unfeasible, thus offsetting the method's ability to seamlessly deal with topological transitions.

The complexities and limitations of the two approaches just described derive largely from i) the need for dislocation segments to remain linearly connected in order for dislocation lines to remain boundaries, or 'divergence-free', and ii) the inability of the phase field method to give reliable results for large-scale 3D simulations. In line dislocation simulations especially, the resulting dynamics inevitably leads to complex line entanglements that are difficult to track and negotiate effectively. In light of these complexities and limitations, we develop a 'line-free' paradigm differing fundamentally from traditional line-based schemes in that the dislocation density is concentrated at points, or *monopoles*, and an explicit linear connectivity, or 'sequence', between the monopoles is not defined or enforced. Instead, the monopoles move as an unstructured point set subject to a weak divergence constraint. In this sense, the new paradigm sidesteps the need to track dislocation lines, an attribute that offers significant computational advantages

in terms of simplicity and efficiency. In particular, it affords an extension to three dimensions of the wealth of point-dislocation methods that have been developed and extensively applied in two dimensions (cf. the seminal paper [94] and derivative works thereof, too numerous to list or even summarize here).

### 3.3 Introduction to the Method of Monopoles

The basis for the new paradigm is a reformulation of dislocation dynamics as a problem of *transport of measures*<sup>1</sup> (cf., e.g., [97] for background on optimal transport theory). Whereas the transport nature of dislocation dynamics has long been appreciated (cf., e.g., [62]), the literature to date is largely restricted to ‘continuously distributed dislocations’, or dislocation densities described by regular functions. However, as already noted, dislocations are line defects and, as such, measures and not functions. This distinction is not insignificant but fundamental. Indeed, the reformulation of dislocation transport theory from functions to measures affords a number of essential extensions and provides the basis for the present work: i) it enables the direct treatment of dislocation as line objects, as opposed to ‘diffuse’ or ‘distributed’ functions; ii) it leads to notions of *weak solution* and of weak satisfaction of the divergence constraint that, in particular, open the way for spatial approximation schemes other than segments; iii) it introduces concepts from transport theory such as transport maps and push-forward operations enabling exact geometrical updates; iv) it supports time discretizations resulting in incremental minimum problems for energy-dissipation functionals; and v) it enables discretizations of the dislocation density within spaces of measures, e.g., by means of Dirac masses or ‘monopoles’, which would otherwise be undefined in functional spaces.

Within this measure-theoretical framework, monopoles suggest themselves as a canonical approximation owing to the density properties of Dirac masses in spaces of measures. Specifically, every monopole carries a Burgers vector and an element of line. The monopoles then move according to mobility kinetics driven by elastic and applied forces. The divergence constraint, expressing the requirement that the monopoles approximate a boundary, is enforced weakly. Most importantly, at no point in the approximation or in the calculations an explicit linear connectivity, or

---

<sup>1</sup>Here and throughout this work, the term *measure*, which is standard in mathematics (cf., e.g., [95]), is used simply to emphasize that certain fields, such as the plastic deformation of the dislocation density, are not regular functions but are instead concentrated on surfaces or lines and are characterized by their action on appropriate test functions; cf. also [96] for a rigorous treatment of plastic deformations and dislocation densities as currents.

'sequence', between the monopoles is defined or enforced. The monopoles instead move as an unstructured point set subject to the weak divergence constraint. In this sense, the new paradigm is 'line-free', i.e., it sidesteps the need to track dislocation lines, an attribute that offers significant computational advantages in terms of simplicity and efficiency.

The time discretization developed in the present work parallels the pioneering work of Jordan, Kinderlehrer, and Otto [98] on transport of scalar measures, and reduces the problem to the successive minimization of an incremental energy-dissipation functional. The solutions of these minimum problems define a time-wise sequence of incremental transport maps. Pushforward by the incremental transport maps then supplies a geometrically exact update for the dislocation measure that, in particular, preserves the divergence-free constraint. The spatial discretization of the transport maps in turn mirrors similar mesh-free discretization schemes proposed in the context of solid and fluid flows [99] and diffusion [100]. Because gradients are required by the geometrical updates, the discretization of the transport map must be conforming. We specifically use a max-ent interpolation scheme [101] that, in keeping with the 'line-free' character of the monopole approximation, does not require sequencing of the monopoles.

The rest of the chapter is organized as follows. In Section 3.4, we begin with a succinct review of dislocation dynamics as a problem of transport of measures. The representation of dislocations as line currents<sup>2</sup> [96, 104, 105] is summarized in Section 3.4. Of particular concern is the formulation of transport equations in a weak form that is applicable to dislocation densities that are concentrated on lines or points and that are not differentiable in the sense of ordinary functions, cf. Section 3.4. An additional focus concerns the reformulation of the transport problem in terms of transport maps and geometrically-exact push-forward operations that pave the way for time discretization, cf. Section 3.4. In order to close the transport problem, a mobility law delivering the instantaneous dislocation velocity needs to be specified. Section 3.5 develops the conventional energetic viewpoint that the dislocation motion is a *gradient flow* driven by energetic driving forces and governed by kinetics. We specifically focus on variational formulations of mobility, Section 3.5, and energy, Sections 3.5 and 3.5, that provide the basis for the incremental minimum problems developed subsequently. Section 3.5 focuses

---

<sup>2</sup>Currents arise in geometrical measure theory (cf., e.g., [102, 103]) as special measures, indeed distributions, which generalize the Dirac delta distribution to lines and surfaces and carry vector or tensor-valued charge capable of acting on general forms.

on the representation of the energy as a function of the dislocation density. In particular, we present a derivation based on the Helmholtz decomposition that generalizes an earlier derivation of Mura [106] to arbitrary domains and nonlinear behavior. In Section 3.5 we deal with the logarithmic divergence of the energy by means of an explicit core regularization based on gradient elasticity. In Section 3.6, we address issues of approximation, including time discretization, discretization of the dislocation measure and discretization of the transport map. Following [98–100], time discretization is effected by defining an incremental energy-dissipation functional for the transport map, with the update of the dislocation measure following as a byproduct, cf. Section 3.6. Exploiting the property that the incremental energy-dissipation functional is well-defined for general dislocation measures, we proceed to discretize the dislocation measure by means of Dirac masses, or monopoles, cf. Section 3.6. We additionally discretize the transport map by means of mesh-free max-ent interpolation [101], cf. Section 3.6, in keeping with the line-free character of the approach. The incremental equations of equilibrium finally follow by rendering the incremental energy-dissipation functional stationary with respect to the monopole positions, cf. Section 3.6. The general structure of the resulting dislocation dynamics solver and selected issues of implementation are discussed in Section 3.6. The developments to this point are based on the assumption that the incremental transport map is continuous and, therefore, the dislocation measure undergoes no topological transitions. Section 3.7 addresses two common topological transitions in the context of the monopole approximation, namely dislocation reactions and dislocation nucleation.

### 3.4 Dislocation Dynamics as a Transport Problem

The formulation of dislocation dynamics as a transport problem is well known [62], but may stand a brief review as it provides the basis for all subsequent developments. We specifically call attention to the representation of dislocations as measures, or, more specifically, as line currents [96, 104, 105], that opens the way for particle-like approximation schemes such as the method of monopoles developed in this work.

#### Dislocation geometry

We consider throughout a crystal occupying a region  $\Omega \subset \mathbb{R}^3$ . A continuum *plastic deformation* generated by crystallographic slip is a tensor-valued measure  $\beta^p$  supported on a *slip surface*  $\Sigma$ , contained within crystallographic planes, characterized

by the property that

$$\int_{\Omega} \eta_{ij} d\beta_{ij}^p = \int_{\Sigma} \eta_{ij} \delta_i \nu_j dS \quad (3.1)$$

for all test functions  $\eta$ , where  $\nu(\mathbf{x})$  and  $dS(\mathbf{x})$  are the unit normal and element of area at  $\mathbf{x} \in \Sigma$ , respectively. In addition, the slip surface  $\Sigma$  is a surface of discontinuity of the displacement field of the crystal and  $\delta(\mathbf{x})$  is the displacement jump across  $\mathbf{x} \in \Sigma$ . Within the Volterra theory of dislocations, the value of the displacement jump is constrained to be an integer combination of Burgers vectors characteristic of the crystal class. In particular, the displacement jump is piecewise constant over the slip surface.

The Nye [107] dislocation measure  $\alpha$  is given by Kröner's formula [108] as

$$\alpha_{ij} = -\beta_{ik,l}^p e_{lkj}, \quad (3.2)$$

where  $e_{ijk}$  denotes the permutation tensor and the curl is to be interpreted in a distributional sense, i.e.,

$$\int_{\Omega} \eta_{ij} d\alpha_{ij} = \int_{\Sigma} \eta_{ij,l} e_{jlk} d\beta_{ik}^p \quad (3.3)$$

for all test functions  $\eta$ . For Volterra dislocations, the dislocation measure has the representation

$$\int_{\Omega} \eta_{ij} d\alpha_{ij} = \int_{\Gamma} \eta_{ij} b_i t_j ds \quad (3.4)$$

for all test functions  $\eta$ , where *dislocation line*, within  $\Sigma$ ,  $\mathbf{t}(\mathbf{x})$  and  $ds(\mathbf{x})$  are the unit tangent vector and the element of length at  $\mathbf{x} \in \Gamma$ , respectively, and, for every  $\mathbf{x} \in \Gamma$ ,  $\mathbf{b}(\mathbf{x})$  is a Burgers vector of the crystal. In particular, the dislocation line separates regions of constant displacement jump within the slip surface.

It follows from Kröner's formula (3.2) that

$$\alpha_{ij,j} = 0, \quad (3.5)$$

i.e., the dislocation density is closed, or *divergence-free*. Here, again, the divergence is to be interpreted in a distributional sense, i.e.,

$$-\int_{\Gamma} \xi_{i,j} d\alpha_{ij} = 0, \quad (3.6)$$

for all test functions  $\xi$ . The null-divergence property—Equation (3.5)—of the dislocation density implies that dislocations cannot terminate in the bulk but must

form closed loops or networks or exit through the boundary. It also implies Frank's rule for dislocation branching (cf., e.g., [26]).

Representations (3.1) and (3.4) give measure-theoretical expression to distributions of crystallographic slip and Volterra dislocations. We note that the plastic-deformation and dislocation measures are also (rectifiable integer-valued) *currents* [96, 105] of well-defined dimension, namely, the plastic deformation measure is a two-dimensional current and the dislocation measure is a one-dimensional current. As currents, the plastic deformation and dislocation measures additionally have well-defined *boundaries*. In the sense of currents, Kröner's formula (3.2) simply defines the dislocation current as the boundary of the plastic-deformation current. In addition, the divergence-free condition (3.5) simply records the fact that a boundary has itself null boundary.

### Dislocation transport

Next, we consider moving dislocations characterized by a time-dependent dislocation measure  $\alpha(\mathbf{x}, t)$ . Let  $S$  be a fixed, arbitrary oriented surface with boundary  $\partial S$ . The total Burgers vector crossing  $S$  is then given by<sup>3</sup>

$$b_i(S, t) = \int_S \nu_j d\alpha_{ij}. \quad (3.7)$$

Taking rates, we obtain

$$\dot{b}_i(S, t) = \int_S \nu_j d\dot{\alpha}_{ij}, \quad (3.8)$$

with all derivatives understood in the distributional sense. But  $\dot{b}(S, t)$  must also equal the flux of Burgers vector across the boundary  $\partial S$ , i.e.,

$$\dot{b}_i(S, t) = \int_{\partial S} e_{mnk} v_m t_k d\alpha_{in}, \quad (3.9)$$

where  $\mathbf{v}(\mathbf{x}, t)$  is the dislocation velocity. Note that  $\mathbf{v}(\mathbf{x}, t)$  has no contribution to  $\dot{b}(S, t)$  if it is parallel to the dislocation line or the contour  $\partial S$  at  $\mathbf{x}$ , as required.

An application of Stoke's theorem then gives

$$\int_S \nu_j d\dot{\alpha}_{ij} = \int_S e_{jlk} e_{mnk} \nu_j (v_m d\alpha_{in})_{,l}, \quad (3.10)$$

and, since  $S$  is arbitrary,

$$\dot{\alpha}_{ij} - e_{jlk} e_{mnk} (v_m \alpha_{in})_{,l} = 0, \quad (3.11)$$

---

<sup>3</sup>More precisely,  $b(S, t)$  is the link of  $\alpha$ , regarded as a current, and  $S$ , cf., e.g., [109].

which defines a transport equation for the dislocation measure. Using the identity

$$e_{ijk}e_{imn} = \delta_{jm}\delta_{kn} - \delta_{jn}\delta_{km}, \quad (3.12)$$

the transport equation (3.11) can be recast in the equivalent form

$$\dot{\alpha}_{ij} - (\alpha_{il}v_j - \alpha_{ij}v_l)_{,l} = 0, \quad (3.13)$$

or, using Equation (3.5),

$$\dot{\alpha}_{ij} + \alpha_{ij,l}v_l - \alpha_{il}v_{j,l} + \alpha_{ij}v_{l,l} = 0. \quad (3.14)$$

Taking the distributional divergence of this equation we additionally find that

$$\dot{\alpha}_{ij,j} = 0, \quad (3.15)$$

which shows that the transport equation (3.11) is indeed consistent with the divergence constraint. More precisely, testing (3.11) with  $\eta_{ij}$  we obtain

$$\int_{\Omega} \eta_{ij} d\dot{\alpha}_{ij} + \int_{\Omega} e_{jlk}e_{mnk}v_m\eta_{ij,l}d\alpha_{in} = 0. \quad (3.16)$$

Setting  $\eta_{ij} = \xi_{i,j}$ , this identity further reduces to

$$\int_{\Omega} \xi_{i,j} d\dot{\alpha}_{ij} = 0, \quad (3.17)$$

which indeed implies (3.6).

The transport equation (3.11) has the effect of restricting the possible rates and variations of the dislocation measure  $\alpha$ . Specifically, for a rate  $\dot{\alpha}$  to be admissible, there must exist a vector field  $\mathbf{v}(\mathbf{x}, t)$  such that the curl of  $\alpha \times \mathbf{v}$  equals  $-\dot{\alpha}$ .

### Transport maps

An equivalent Lagrangian formulation of the transport problem that plays a central role in time discretization can be formulated in terms of a transport map  $\varphi : \Omega \times [0, T] \rightarrow \Omega$  [97]. In this representation, the dislocation measure  $\alpha(\cdot, t)$  at time  $t$  is the *push-forward* of the initial dislocation measure  $\alpha_0(\mathbf{x}) = \alpha(\cdot, 0)$  by  $\varphi(\cdot, t)$ . Formally,

$$\alpha_t = \varphi_{t\#} \alpha_0, \quad (3.18)$$

where we write  $d\alpha_t(\mathbf{x}) = d\alpha(\mathbf{x}, t)$  and  $\varphi_t(\mathbf{x}) = \varphi(\mathbf{x}, t)$ , and  $\varphi_{t\#}$  denotes the push-forward by  $\varphi_{t\#}$ .

The appropriate notion of push-forward for dislocation measures, regarded as line currents, is that  $\nu$  is the push-forward of  $\mu$  by  $\varphi$  if

$$\int_{\Omega} \eta_{ij}(\mathbf{y}) d\nu_{ij}(\mathbf{y}) = \int_{\Omega} \eta_{ij}(\varphi(\mathbf{x})) \nabla \varphi_{jp}(\mathbf{x}) d\mu_{ip}(\mathbf{x}), \quad (3.19)$$

for all test functions  $\eta$ . We note that

$$\begin{aligned} \int_{\Omega} \xi_{i,j}(\mathbf{y}) d\nu_{ij}(\mathbf{y}) &= \int_{\Omega} \xi_{i,j}(\varphi(\mathbf{x})) \nabla \varphi_{jp}(\mathbf{x}) d\mu_{ip}(\mathbf{x}) \\ &= \int_{\Omega} (\xi_i(\varphi(\mathbf{x})))_{,p} d\mu_{ip}(\mathbf{x}), \end{aligned} \quad (3.20)$$

whence it follows that the push-forward operation preserves the divergence-free condition, i.e., if  $\mu$  is divergence-free then so is  $\nu$ . The local form of the push-forward is obtained by considering absolutely continuous dislocation measures, or *continuously distributed dislocations*,  $d\mu_{ij} = f_{ij} dx$  and  $d\nu_{ij} = g_{ij} dy$ , where  $\mathbf{f}$  and  $\mathbf{g}$  are regular *dislocation densities*. In this case,

$$\begin{aligned} \int_{\Omega} \eta_{ij}(\mathbf{y}) g_{ij}(\mathbf{y}) dy &= \int_{\Omega} \eta_{ij}(\varphi(\mathbf{x})) g_{ij}(\varphi(\mathbf{x})) \det(\nabla \varphi(\mathbf{x})) dx \\ &= \int_{\Omega} \eta_{ij}(\varphi(\mathbf{x})) \nabla \varphi_{jp}(\mathbf{x}) f_{ip}(\mathbf{x}) dx, \end{aligned} \quad (3.21)$$

which requires that

$$g_{ij}(\varphi(\mathbf{x})) = \frac{\nabla \varphi_{jp}(\mathbf{x}) f_{ip}(\mathbf{x})}{\det(\nabla \varphi(\mathbf{x}))}. \quad (3.22)$$

We observe that the push-forward operation entails reorientation and stretching of the dislocation line.

For completeness, we verify that Equation (3.18) is equivalent to the transport equation (3.11). Using the definition (3.19) of push-forward, we have

$$\int_{\Omega} \eta_{ij}(\mathbf{y}) d\alpha_{ij}(\mathbf{y}, t) = \int_{\Omega} \eta_{ij}(\varphi(\mathbf{x}, t)) \nabla \varphi_{jp}(\mathbf{x}, t) d\alpha_{ip}(\mathbf{x}, 0). \quad (3.23)$$

For simplicity, we consider the case of absolutely continuous dislocation measures  $d\alpha_{ij}(\mathbf{x}, t) = \rho_{ij}(\mathbf{x}, t) dx$ . In this case, the push-forward (3.23) reduces to

$$\rho_{ij}(\varphi(\mathbf{x}, t), t) = \frac{\nabla \varphi_{jp}(\mathbf{x}, t) \rho_{ip}(\mathbf{x}, 0)}{\det(\nabla \varphi(\mathbf{x}, t))}. \quad (3.24)$$

Taking time derivatives, we obtain

$$\begin{aligned} \dot{\rho}_{ij}(\varphi(\mathbf{x}, t), t) + \rho_{ij,k}(\varphi(\mathbf{x}, t), t) \dot{\varphi}_k(\mathbf{x}, t) &= \\ \frac{\nabla \dot{\varphi}_{jp}(\mathbf{x}, t) \rho_{ip}(\mathbf{x}, 0)}{\det(\nabla \varphi(\mathbf{x}, t))} - \frac{\nabla \varphi_{jp}(\mathbf{x}, t) \rho_{ip}(\mathbf{x}, 0)}{\det(\nabla \varphi(\mathbf{x}, t))} \nabla \dot{\varphi}_{lq}(\mathbf{x}, t) \nabla \varphi_{ql}^{-1}(\mathbf{x}, t) &= \\ \nabla \dot{\varphi}_{jp}(\mathbf{x}, t) \nabla \varphi_{pk}^{-1}(\mathbf{x}, t) \rho_{ik}(\varphi(\mathbf{x}, t), t) - \\ \nabla \dot{\varphi}_{lq}(\mathbf{x}, t) \nabla \varphi_{ql}^{-1}(\mathbf{x}, t) \rho_{ij}(\varphi(\mathbf{x}, t), t), \end{aligned} \quad (3.25)$$

or, by a suitable change of variables,

$$\dot{\rho}_{ij}(\mathbf{y}, t) + \rho_{ij,k}(\mathbf{y}, t)v_k(\mathbf{y}, t) = v_{j,k}(\mathbf{y}, t)\rho_{ik}(\mathbf{y}, t) - v_{k,k}(\mathbf{y}, t)\rho_{ij}(\mathbf{y}, t), \quad (3.26)$$

which is identical to (3.14) with velocity

$$v_i(\mathbf{y}, t) = \dot{\varphi}_i(\varphi^{-1}(\mathbf{y}, t), t), \quad (3.27)$$

as required.

### 3.5 Mobility and Energetics

In order to close the transport problem (3.11), we need to specify a mobility law that supplies the instantaneous dislocation velocity. Whereas the transport problem (3.11) concerns the geometry of the dislocations and its evolution in time, the mobility law encodes the *kinetics* of dislocation motion. In this section, we develop the conventional energetic viewpoint that the dislocation motion is a *gradient flow* driven by energetic driving forces and governed by kinetics. We specifically focus on variational formulations that provide the basis for the incremental minimum problems developed subsequently.

#### Dislocation mobility

In order to identify the appropriate driving force for dislocation motion, we consider the rate of elastic energy  $\dot{E}$  attendant to a plastic deformation rate  $\dot{\beta}^p$ . Alternatively, we may regard  $\dot{\beta}^p$  as a *variation* of the plastic deformation  $\beta^p$  and  $\dot{E}$  the attendant variation of the energy  $E$ , as the operations of taking rates and variations are mathematically identical. We have

$$\begin{aligned} \dot{E} &= \int_{\Omega \setminus \Sigma} \sigma_{ij} \dot{\beta}_{ij}^e dx = \int_{\Omega} \sigma_{ij} (\dot{u}_{i,j} - \dot{\beta}_{ij}^p) dx \\ &= \int_{\Omega} \sigma_{ij} (\dot{u}_{i,j} - \dot{\beta}_{ij}^p) dx = - \int_{\Omega} \sigma_{ij} d\dot{\beta}_{ij}^p, \end{aligned} \quad (3.28)$$

i.e., at equilibrium and in the absence of body forces and applied tractions, the rate of elastic energy equals the negative of the plastic work rate. We recall that equilibrium stress fields admit the representation

$$\sigma_{ij} = -\chi_{ik,l} e_{lkj} = \sigma_{ji}, \quad (3.29a)$$

$$\chi_{ij,j} = 0, \quad (3.29b)$$

in terms of an Airy stress potential  $\chi$ . Inserting this representation into Equation (3.28), we obtain

$$\dot{E} = \int_{\Omega} \chi_{ik,l} e_{lkj} d\dot{\beta}_{ij}^p = \int_{\Omega} \chi_{ij} d\dot{\alpha}_{ij}, \quad (3.30)$$

which shows that the Airy stress potential and the dislocation measure are *work conjugate*.

In order to proceed further, we need to characterize the admissible rates, or variations,  $\dot{\alpha}$ . This characterization is non-trivial since the dislocation densities  $\alpha$  define a non-linear space.<sup>4</sup> Formally, the appropriate notion of variation of  $\alpha$  follows from the transport equation (3.11), namely,  $\dot{\alpha}$  is an admissible rate, or variation, if there exists a velocity field  $\mathbf{v}$  such that (3.11) is satisfied. Using this differential structure, we have

$$\begin{aligned} \dot{E} &= \int_{\Omega} \chi_{ij} d\dot{\alpha}_{ij} = \int_{\Omega} \chi_{ij,l} e_{jlk} e_{mnk} v_m d\alpha_{in} \\ &= \int_{\Omega} \sigma_{ik} e_{nmk} v_m d\alpha_{in} = \int_{\Gamma} \sigma_{ik} e_{nmk} v_m b_i t_n ds = \int_{\Gamma} f_m v_m ds, \end{aligned} \quad (3.31)$$

where

$$f_m = \sigma_{ik} e_{nmk} b_i t_n \quad (3.32)$$

is the Peach-Koehler force per unit dislocation length.

In view of (3.32), standard thermodynamic arguments suggest that the dislocation motion is governed by a mobility law of the type

$$v_i = D_i \psi^*(\mathbf{f}), \quad (3.33)$$

where  $\psi(\mathbf{f})$  is a dual kinetic potential and  $D_i$  denotes partial differentiation. Alternatively, we may express the mobility law in inverse form as

$$f_i = D_i \psi(\mathbf{v}), \quad (3.34)$$

where the kinetic potential  $\psi(\mathbf{v})$  is the Legendre transform of  $\psi^*(\mathbf{f})$ , provided that it exists.<sup>5</sup>

The precise form of the mobility law, and the potential  $\psi(\mathbf{v})$  depends on the physical processes that limit dislocation mobility (cf., e.g., [26]). For instance, if lattice friction is the rate-limiting mechanism, then

$$\psi(\mathbf{v}) = \tau_c |\mathbf{v}|, \quad (3.35)$$

<sup>4</sup>cf., e.g., [97, 110] for background on the closely related spaces of probability measures that arise in scalar transport problems. The geometry of optimal transport of vector-value measures appears to be considerably less developed.

<sup>5</sup>We recall that the Legendre transform is well-defined on proper, convex, lower-semicontinuous functions, cf., e.g., [111].

where  $\tau_c$  is the critical resolved shear stress. In particular,  $\psi(\mathbf{v})$  is homogeneous of degree one in the dislocation velocity. If, instead, dislocation motion is controlled by phonon drag, then

$$\psi(\mathbf{v}) = \frac{B}{2}|\mathbf{v}|^2, \quad (3.36)$$

where  $B$  is a phonon-drag coefficient. In this case,  $\psi(\mathbf{v})$  is quadratic in the dislocation velocity.

### Dislocation energy

As we have seen, within an energetic framework the motion of the dislocations, and the attendant evolution of the dislocation measure, is driven by energetic or Peach-Koehler forces. For present purposes, we shall require a representation of the energy that is well-defined for general dislocation measures, including Volterra dislocations and, subsequently, dislocation monopoles. We derive one such representation in two steps. Firstly, we present a general argument based on the Helmholtz decomposition [104] that shows that, in the absence of Dirichlet boundary conditions, the—possibly nonlinear—elastic energy of the solid depends solely on the dislocation density. This representation generalizes a similar result obtained by Mura [106] for the special case of linear elasticity. Unfortunately, conventional linear elasticity is not well-suited to Volterra dislocations due to the well-known logarithmic divergence of the energy (cf., e.g., [26]). In order to sidestep this difficulty, we develop a regularization based on strain-gradient elasticity that renders the energy well-defined for general dislocation measures, including dislocation monopoles.

Suppose that the crystal deforms under the action of body forces  $\mathbf{f}$ , prescribed displacements  $\mathbf{g}$  over the displacement or Dirichlet boundary  $\Gamma_D$  and applied tractions  $\mathbf{h}$  over the traction or Neumann boundary  $\Gamma_N$ . We recall that the Helmholtz decomposition of  $\beta^p$  is [112]

$$\beta_{ij}^p = v_{i,j} + w_{ik,l}e_{lkj}, \quad (3.37)$$

where  $\mathbf{v}$  and  $\mathbf{w}$  are potentials. To this representation, we additionally append the Lorenz gauge condition

$$w_{ij,j} = 0, \quad (3.38)$$

and the boundary conditions

$$v_i = 0, \quad \text{on } \Gamma_D, \quad (3.39a)$$

$$w_{ik,l}e_{lkj}n_j = 0, \quad \text{on } \Gamma_N. \quad (3.39b)$$

Taking the divergence and the curl of (3.37), we obtain

$$\beta_{ij,j}^p = v_{i,jj}, \quad (3.40a)$$

$$\beta_{im,n}^p e_{nmj} = -\alpha_{ij} = w_{ik,ln} e_{lkm} e_{nmj} = -w_{ij,kk}, \quad (3.40b)$$

where we have used the gauge condition (3.38) and Kröner's formula (3.2). Equations (3.40), together with the boundary conditions (3.39), uniquely determine the potentials. In particular, we note that the vector potential  $\mathbf{w}$  is fully determined by the dislocation measure  $\boldsymbol{\alpha}$ .

Let  $\bar{\boldsymbol{\sigma}}$  be a stress field in equilibrium with the body forces and the applied tractions, i.e.,

$$\bar{\sigma}_{ij,j} + f_i = 0, \quad \text{in } \Omega, \quad (3.41a)$$

$$\bar{\sigma}_{ij} n_j = h_i, \quad \text{on } \Gamma_N. \quad (3.41b)$$

Then, the potential energy of the crystal takes the form

$$\Phi(\mathbf{u}, \boldsymbol{\beta}^p) = \int_{\Omega} (W(D\mathbf{u} - \boldsymbol{\beta}^p) - \bar{\sigma}_{ij}(u_{i,j} - \beta_{ij}^p)) dx, \quad (3.42)$$

where  $W(\boldsymbol{\beta}^e)$  is the elastic strain energy density and  $D\mathbf{u}$  is the distributional derivative of the displacement field. For a linear elastic crystal,

$$W(\boldsymbol{\beta}^e) = \frac{1}{2} c_{ijkl} \epsilon_{ij}^e \epsilon_{kl}^e, \quad (3.43)$$

where  $c_{ijkl}$  are the elastic moduli and  $\epsilon_{ij}^e = (\beta_{ij}^e + \beta_{ji}^e)/2$  are the elastic strains. However, we emphasize that the present derivation does not require linearity and holds for general strain energy densities. The elastic energy at equilibrium follows as

$$E(\boldsymbol{\beta}^p) = \inf\{\Phi(\mathbf{u}, \boldsymbol{\beta}^p), \mathbf{u} = \mathbf{g} \text{ on } \Gamma_D\}. \quad (3.44)$$

But, inserting the Helmholtz decomposition (3.37) into (3.42) gives

$$\Phi(\mathbf{u}, \boldsymbol{\beta}^p) = \int_{\Omega} (W(D\mathbf{u} - D\mathbf{v} - \nabla \times \mathbf{w}) - \bar{\sigma}_{ij}(v_{i,j} + w_{ik,l} e_{lkj})) dx. \quad (3.45)$$

Absorbing  $\mathbf{v}$  into  $\mathbf{u}$ , which by (3.39a) leaves  $\mathbf{u}$  unchanged over  $\Gamma_D$ , we obtain

$$E(\boldsymbol{\beta}^p) = \inf\{\Phi(\mathbf{u}, \nabla \times \mathbf{w}), \mathbf{u} = \mathbf{g} \text{ on } \Gamma_D\} = E(\boldsymbol{\alpha}), \quad (3.46)$$

since the potential  $\mathbf{w}$  is fully determined by the dislocation density  $\boldsymbol{\alpha}$ . Let  $\mathbf{u}^*$  be the displacement field at equilibrium, also fully determined by  $\boldsymbol{\alpha}$ . Then,

$$\int_{\Omega} (DW_{ij}(D\mathbf{u}^* - \nabla \times \mathbf{w}) - \bar{\sigma}_{ij}) \eta_{i,j} dx = 0, \quad (3.47)$$

for all test functions  $\boldsymbol{\eta}$ , and the stress field at equilibrium follows as

$$\sigma_{ij}^* = DW_{ij}(D\mathbf{u}^* - \nabla \times \mathbf{w}), \quad (3.48)$$

which is also fully determined by the dislocation density  $\boldsymbol{\alpha}$ .

In cases where the body is subject to traction boundary conditions only, such as an infinite body or a periodic unit cell, a more direct expression for the energy can be obtained as follows. Begin by writing the potential energy (3.42) as

$$\Phi(\boldsymbol{\beta}^e) = \int_{\Omega} (W(\boldsymbol{\beta}^e) - \bar{\sigma}_{ij}\beta_{ij}^e) dx, \quad (3.49)$$

where

$$\beta_{ij}^e = u_{i,j} - \beta_{ij}^p \quad (3.50)$$

is the elastic deformation. From Kröner's formula (3.2) we have

$$\alpha_{ij} = \beta_{ik,l}^e e_{lkj}. \quad (3.51)$$

Thus, in the absence of displacement boundary conditions, the equilibrium elastic deformation  $\boldsymbol{\beta}^{e*}$  follows directly from the minimum problem

$$\boldsymbol{\beta}^{e*} \in \operatorname{argmin} \{ \Phi(\boldsymbol{\beta}^e), \nabla \times \boldsymbol{\beta}^e = \boldsymbol{\alpha} \}. \quad (3.52)$$

Thus,  $\boldsymbol{\beta}^{e*}$  minimizes the potential energy of the solid subject to the constraint that it be compatible everywhere except on the support of the dislocation measure, where it must satisfy a curl constraint, e.g., in the sense of Burgers circuits. Enforcing the curl constraint by means of a Lagrange multiplier  $\boldsymbol{\chi}$ , or Airy stress potential, results in the Lagrangian

$$L(\boldsymbol{\beta}^e, \boldsymbol{\chi}) = \int_{\Omega} (W(\boldsymbol{\beta}^e) - \bar{\sigma}_{ij}\beta_{ij}^e - \chi_{ij}(\alpha_{ij} - \beta_{ik,l}^e e_{lkj})) dx, \quad (3.53)$$

or, integrating by parts,

$$L(\boldsymbol{\beta}^e, \boldsymbol{\chi}) = \int_{\Omega} (W(\boldsymbol{\beta}^e) - (\bar{\sigma}_{ij} + \chi_{ik,l} e_{lkj})\beta_{ij}^e - \chi_{ij}\alpha_{ij}) dx, \quad (3.54)$$

which must be stationary at equilibrium. We note that  $\boldsymbol{\beta}^e$  enters the Lagrangian undifferentiated and can, therefore, be minimized pointwise, which results in the complementary energy

$$\Phi^*(\boldsymbol{\chi}, \boldsymbol{\alpha}) = \int_{\Omega} (W^*(\nabla \times \boldsymbol{\chi} + \bar{\boldsymbol{\sigma}}) + \chi_{ij}\alpha_{ij}) dx, \quad (3.55)$$

where

$$W^*(\boldsymbol{\sigma}) = \sup\{\sigma_{ij}\beta_{ij}^e - W(\boldsymbol{\beta}^e)\} \quad (3.56)$$

is the complementary energy density. For linear elastic solids, eq. (3.43), we explicitly have

$$W^*(\boldsymbol{\sigma}) = \frac{1}{2} c_{ijkl}^{-1} \sigma_{ij} \sigma_{kl}. \quad (3.57)$$

The elastic energy follows again by minimization with respect to the elastic deformations, i.e.,

$$E(\boldsymbol{\alpha}) = \inf \Phi^*(\cdot, \boldsymbol{\alpha}). \quad (3.58)$$

From Equation (3.58) we conclude that, in the absence of Dirichlet boundary conditions, the elastic energy at equilibrium is a function solely of the dislocation measure, as advertised.

### Core regularization

One key advantage of the representation (3.58) of the energy is that  $\boldsymbol{\alpha}$  enters in  $\Phi^*(\boldsymbol{\chi}, \boldsymbol{\alpha})$  linearly and can therefore be treated as a general measure, as required by the monopole approximations pursued subsequently. However, as already noted, a direct application of (3.58) to Volterra dislocations is not possible due to the well-known logarithmic divergence of the energy. This type of energy divergence is well-known in connection with elliptic problems with measure data, e.g., the Laplace equation with a point source [113]. In these problems, equilibrium solutions exist but have infinite energy, which precludes an energetic characterization of the solutions and attendant configurational forces.

A number of regularizations of linear elasticity have proposed in order to eliminate the logarithmic divergence of the energy of Volterra dislocations (cf., e.g., [40]), including discrete elasticity [104, 114], core cut-offs [26] and nonlinear elasticity [115, 116]. Yet another regularization that is particularly well-suited to general dislocation measures consists of endowing dislocation lines with a *core profile*, e.g., by mollifying the dislocation measure on the scale of the lattice parameter  $\epsilon$  [105]. In this approach, the dislocation density is given the representation

$$\boldsymbol{\alpha}^\epsilon = \phi^\epsilon * \boldsymbol{\alpha}, \quad (3.59)$$

where  $\boldsymbol{\alpha}$  is a collection of Volterra dislocation lines,  $\phi^\epsilon$  is a mollifier and  $*$  denotes

convolution<sup>6</sup>. The regularized energy is then

$$E^\epsilon(\boldsymbol{\alpha}) = E(\boldsymbol{\alpha}^\epsilon), \quad (3.60)$$

with  $E(\cdot)$  given by (3.58).

A connection between mollification of the dislocation density and strain-gradient elasticity can be established as follows. Begin by regularizing the complementary energy (3.55) as

$$\Phi^{*\epsilon}(\boldsymbol{\chi}, \boldsymbol{\alpha}) = \int_{\Omega} (W^*(\nabla \times (1 - \epsilon^2 \Delta)\boldsymbol{\chi} + \bar{\boldsymbol{\sigma}}) + \chi_{ij} \alpha_{ij}) dx, \quad (3.61)$$

where  $\Delta$  denotes the Laplacian operator. Changing variables to

$$\boldsymbol{\chi}^\epsilon = (1 - \epsilon^2 \Delta)\boldsymbol{\chi}, \quad (3.62)$$

the regularized complementary energy (3.61) becomes

$$\Phi^{*\epsilon}(\boldsymbol{\chi}, \boldsymbol{\alpha}) = \int_{\Omega} (W^*(\nabla \times \boldsymbol{\chi}^\epsilon + \bar{\boldsymbol{\sigma}}) + \chi_{ij}^\epsilon \alpha_{ij}^\epsilon) dx = \Phi^*(\boldsymbol{\chi}^\epsilon, \boldsymbol{\alpha}^\epsilon), \quad (3.63)$$

with

$$\boldsymbol{\alpha}^\epsilon = (1 - \epsilon^2 \Delta)^{-1} \boldsymbol{\alpha} = \phi^\epsilon * \boldsymbol{\alpha}, \quad (3.64)$$

and

$$\phi^\epsilon(\mathbf{x}) = \frac{1}{4\pi\epsilon^2|\mathbf{x}|} e^{-|\mathbf{x}|/\epsilon}, \quad (3.65)$$

which identifies the mollifier and the core structure of the dislocations.

For an infinite linear isotropic solid, the elastic energy (3.58) of a sufficiently regular dislocation measure follows as (cf. [26], eq. (4-44))

$$\begin{aligned} E(\boldsymbol{\alpha}) = & -\frac{\mu}{4\pi} \int \int \frac{1}{R(\mathbf{x}, \mathbf{x}')} e_{ikm} e_{jln} d\alpha_{ij}(\mathbf{x}) d\alpha_{kl}(\mathbf{x}') \\ & + \frac{\mu}{8\pi} \int \int \frac{1}{R(\mathbf{x}, \mathbf{x}')} d\alpha_{ii}(\mathbf{x}) d\alpha_{jj}(\mathbf{x}') \\ & + \frac{\mu}{8\pi(1-\nu)} \int \int T_{mn}(\mathbf{x}, \mathbf{x}') e_{ijm} e_{kln} d\alpha_{ij}(\mathbf{x}) d\alpha_{kl}(\mathbf{x}'), \end{aligned} \quad (3.66)$$

where

$$R(\mathbf{x}, \mathbf{x}') = |\mathbf{x} - \mathbf{x}'|, \quad T_{ij}(\mathbf{x}, \mathbf{x}') = \frac{\partial^2 R}{\partial x_i \partial x_j}(\mathbf{x} - \mathbf{x}'), \quad (3.67)$$

---

<sup>6</sup>By a *mollifier* here we understand a sequence  $\phi^\epsilon$  of smooth positive functions of total mass 1 defining a Dirac-sequence. We also recall that the convolution of two functions is defined as  $f * g = \int f(\mathbf{x} - \mathbf{x}')g(\mathbf{x}') dx'$  (cf., e.g., [117]).

$\mu$  is the shear modulus and  $\nu$  Poisson's ratio. Inserting (3.59) into (3.66), we obtain

$$\begin{aligned} E^\epsilon(\boldsymbol{\alpha}) = & -\frac{\mu}{4\pi} \int \int S^\epsilon(\mathbf{x}, \mathbf{x}') e_{ikm} e_{jln} d\alpha_{ij}(\mathbf{x}) d\alpha_{kl}(\mathbf{x}') \\ & + \frac{\mu}{8\pi} \int \int S^\epsilon(\mathbf{x}, \mathbf{x}') d\alpha_{ii}(\mathbf{x}) d\alpha_{jj}(\mathbf{x}') \\ & + \frac{\mu}{8\pi(1-\nu)} \int \int T_{mn}^\epsilon(\mathbf{x}, \mathbf{x}') e_{ijm} e_{kln} d\alpha_{ij}(\mathbf{x}) d\alpha_{kl}(\mathbf{x}'), \end{aligned} \quad (3.68)$$

where we write

$$S = 1/R, \quad S^\epsilon = \phi^\epsilon * \phi^\epsilon * S, \quad (3.69)$$

and

$$R^\epsilon = \phi^\epsilon * \phi^\epsilon * R, \quad T_{ij}^\epsilon = \phi^\epsilon * \phi^\epsilon * T_{ij} = \frac{\partial^2 R^\epsilon}{\partial x_i \partial x_j}. \quad (3.70)$$

By virtue of the regularization of the kernels, the energy (3.68) is now finite for general dislocation measures. In particular, for Volterra dislocations (3.68) specializes to

$$\begin{aligned} E^\epsilon(\boldsymbol{\alpha}) = & -\frac{\mu}{4\pi} \int_\Gamma \int_\Gamma S^\epsilon(\mathbf{x}(s), \mathbf{x}(s')) (\mathbf{b}(s) \times \mathbf{b}(s')) \cdot (\mathbf{t}(s) \times \mathbf{t}(s')) ds ds' \\ & + \frac{\mu}{8\pi} \int_\Gamma \int_\Gamma S^\epsilon(\mathbf{x}(s), \mathbf{x}(s')) (\mathbf{b}(s) \cdot \mathbf{t}(s)) (\mathbf{b}(s') \cdot \mathbf{t}(s')) ds ds' + \\ & \frac{\mu}{8\pi(1-\nu)} \int_\Gamma \int_\Gamma (\mathbf{b}(s) \times \mathbf{t}(s)) \cdot \mathbf{T}^\epsilon(\mathbf{x}(s), \mathbf{x}(s')) \cdot (\mathbf{b}(s') \times \mathbf{t}(s')) ds ds'. \end{aligned} \quad (3.71)$$

For the specific mollifier (3.65), straightforward calculations using the Fourier transform give, explicitly,

$$S^\epsilon(r) = \frac{2\epsilon - (r + 2\epsilon)e^{-r/\epsilon}}{2\epsilon r}, \quad R^\epsilon(r) = \frac{r^2 + 4\epsilon^2 - \epsilon(r + 4\epsilon)e^{-r/\epsilon}}{r}, \quad (3.72)$$

with  $r = |\mathbf{x} - \mathbf{x}'|$ .

**Example 3.5.1 (Circular prismatic loop)** *We illustrate the logarithmic divergence of linearly elastic Volterra dislocations and the effect of regularization by means of the simple example of a circular prismatic loop. Assume that the loop is in the  $(x_1, x_2)$ -plane, has radius  $\rho$  and its Burgers vector is  $\mathbf{b} = b \mathbf{e}_3$ ,  $b > 0$ . Under these conditions, (3.71) reduces to*

$$E^\epsilon(\rho) = \frac{\mu b^2 \rho^2}{8\pi(1-\nu)} \int_0^{2\pi} \int_0^{2\pi} \mathbf{e}_r(\theta) \cdot \mathbf{T}^\epsilon(\rho \mathbf{e}_r(\theta) - \rho \mathbf{e}_r(\theta')) \cdot \mathbf{e}_r(\theta') d\theta d\theta', \quad (3.73)$$

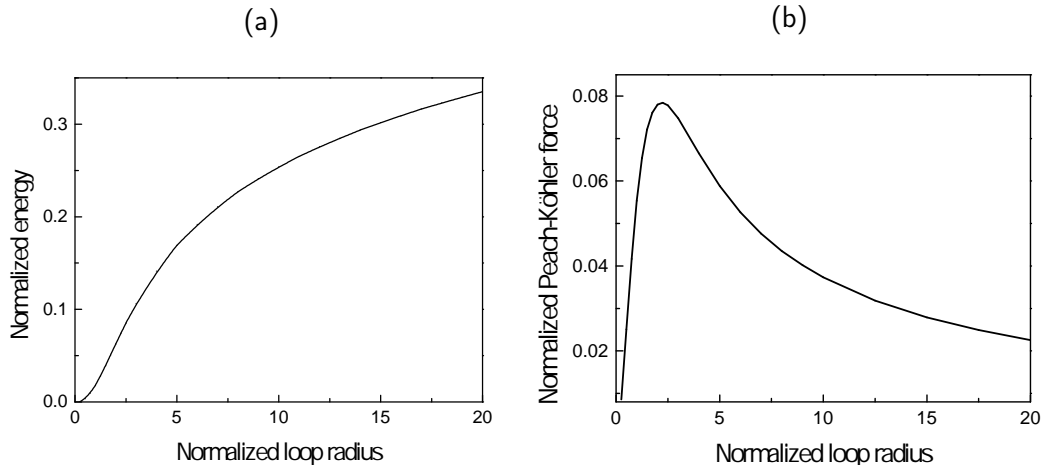


Figure 3.3: Circular prismatic loop. a) Regularized energy normalized by  $\frac{\mu b^2 \rho^2}{8\pi(1-\nu)\epsilon}$ . b) Regularized Peach-Koehler force per unit length normalized by  $\frac{\mu b^2}{8\pi(1-\nu)\epsilon}$ . Loop radius normalized by  $\epsilon$ .

where  $\theta$  is the polar angle and  $e_r(\theta)$  is the radial unit vector on the plane  $x_3 = 0$ . The corresponding Peach-Koehler force acting on the loop is

$$f^\epsilon(\rho) = \frac{1}{2\pi\rho} \frac{\partial E^\epsilon}{\partial \rho}(\rho). \quad (3.74)$$

The dependence of  $E^\epsilon(\rho)$  and  $f^\epsilon(\rho)$  on the loop radius  $\rho$  is shown in Figure 3.3. As may be seen from the figure, both the energy and the Peach-Koehler force are finite for all  $0 \leq \rho < +\infty$ . Thus, the regularization eliminates the divergence of energy and the Peach-Koehler force as  $\rho \rightarrow 0$ . Specifically, we observe that both the energy and the Peach-Koehler force decrease to zero as  $\rho \rightarrow 0$ , at which point the loop annihilates. For large  $\rho$ , the energy grows as  $\rho \log(\rho/\epsilon)$  and the Peach-Koehler force decays as  $\log(\rho/\epsilon)/\rho$ , in agreement with linear elasticity (cf. [26], eqs. (5-28) and (6-52)).  $\square$

### 3.6 Variational Formulation and Approximation

We note from (3.48) that the Peach-Koehler driving force (3.32) is a function of the dislocation measure  $\alpha$ . Therefore, the transport equation (3.11) and the mobility law (3.33) define a closed transport problem governing the evolution of  $\alpha$  in time. The study of transport problems for measures was pioneered by Jordan, Kinderlehrer, and Otto (JKO) [98, 118, 119] in the context of scalar measures. They recognized that such problems can be given a natural variational structure by recourse to time discretization. This incremental approach characterizes the time

evolution as a competition between dissipation, which penalizes departures from the current configuration, and energy, which favors low-energy configurations. Quite crucially, JKO quantify the incremental dissipation by means of a Wasserstein-like distance between two consecutive measures. As we shall see, the overwhelming advantage of such measure-theoretical and time-discrete variational approaches is that they are *geometrically exact* in the sense of the incremental push-forward operation. In the present setting, the resulting incremental dislocation updates are exact with respect to dislocation advection, stretching of null-divergence constraint. Another crucial advantage of measure-theoretical approaches is that they supply a suitable mathematical framework for the formulation of particle methods such as the method of monopoles proposed here.

### Time discretization

We begin by discretizing the transport problem (3.11) in time. To this end, let  $t_0 = 0 < t_1 < \dots < t_\nu < t_{\nu+1} \dots < t_N = T$  be a discretization of the time interval  $[0, T]$ . We wish to determine corresponding discrete approximations  $\alpha_0, \alpha_1 \dots \alpha_N$  of the dislocation measure of a collection of Volterra dislocations and discrete approximations  $\varphi_0, \varphi_1 \dots \varphi_N$  of the transport maps.

We begin by defining an incremental dissipation as

$$D(\varphi_\nu, \varphi_{\nu+1}) = \quad (3.75)$$

$$\min \left\{ \int_{t_\nu}^{t_{\nu+1}} \int_{\Gamma_0} \psi(\dot{\varphi}(s, t)) |\varphi'(s, t)| ds dt : \varphi(t_\nu) = \varphi_\nu, \varphi(t_{\nu+1}) = \varphi_{\nu+1} \right\},$$

where  $\Gamma_0$  is the initial dislocation line parameterized by its arc-length  $s$  with unit tangent vector  $\mathbf{t}(s)$ , we write

$$\varphi(s, t) = \varphi(\mathbf{x}(s), t), \quad \varphi'(s, t) = \nabla \varphi(\mathbf{x}(s), t) \mathbf{t}(s), \quad (3.76)$$

and the minimum is taken over all transport paths taking values  $\varphi_\nu$  at time  $t_\nu$  and  $\varphi_{\nu+1}$  at time  $t_{\nu+1}$ . In addition, let  $E(t, \alpha)$  denote the elastic energy of the dislocation measure  $\alpha$  at time  $t$ , where the explicit dependence on time derives from the time dependence of the applied loads.

On this basis, we introduce the incremental energy-dissipation functional

$$F(\varphi_\nu, \varphi_{\nu+1}) = D(\varphi_\nu, \varphi_{\nu+1}) + E(t_{\nu+1}, (\varphi_{\nu+1})_\# \alpha_0) - E(t_\nu, (\varphi_\nu)_\# \alpha_0), \quad (3.77)$$

and the incremental minimum problem

$$\varphi_{\nu+1} \in \operatorname{argmin} F(\varphi_{\nu}, \cdot). \quad (3.78)$$

We verify that the solution of this problem indeed approximates the mobility law. Taking variations in (3.77) with respect to  $\varphi_{\nu+1}$  and using the path-optimality of the transport map, we obtain

$$\int_{\Gamma_{\nu+1}} \left( D_i \psi(\mathbf{v}(\mathbf{x}(s), t_{\nu+1})) - f_i(\mathbf{x}(s), t_{\nu+1}) \right) \eta_i(s) ds = 0, \quad (3.79)$$

which is a weak statement of the mobility law (3.34).

In summary, the incremental minimum problem (3.78) determines the updated transport map  $\varphi_{\nu+1}$ , whereupon the updated dislocation measure  $\alpha_{\nu+1}$  follows from the *exact geometric update* (3.23). Specifically, we see from Equation (3.77) that the updated transport map  $\varphi_{\nu+1}$  follows from a competition between the incremental dissipation  $D(\varphi_{\nu}, \varphi_{\nu+1})$ , which penalizes departures from  $\varphi_{\nu}$ , and the energy  $E(t_{\nu+1}, (\varphi_{\nu+1})_{\#} \alpha_0)$ , which drives  $\varphi_{\nu+1}$  towards energy minima.

We note the similarity between the incremental dissipation (3.75) and the Wasserstein distance between scalar measures [97]. It is easy to see that the incremental dissipation  $D(\varphi_{\nu}, \varphi_{\nu+1})$  also defines a distance between dislocation measures. The paths for which the minimum in (3.75) is attained are known as *minimizing paths* and arise in theories of inelasticity including plasticity, where they also supply a nexus between time discretization and incremental variational principles [120]. The minimizing path definition (3.75) of the incremental dissipation has the important property that it results in *a priori* energy bounds that in turn ensure the weak convergence of the time-discretized solutions (cf., e.g., [98, 118, 119]).

Unfortunately, because of the geometrical evolution of the dislocation line, the minimizing paths that deliver the incremental dissipation (3.75) cannot be characterized in closed form and additional approximations are required. A simple scheme consists of restricting the incremental paths to a convenient class, e.g., piecewise linear paths of the form

$$\varphi(s, t) \approx \frac{t_{\nu+1} - t}{t_{\nu+1} - t_{\nu}} \varphi_{\nu}(s) + \frac{t - t_{\nu}}{t_{\nu+1} - t_{\nu}} \varphi_{\nu+1}(s), \quad t \in [t_{\nu}, t_{\nu+1} - t], \quad (3.80)$$

whereupon (3.75) reduces to

$$D(\varphi_{\nu}, \varphi_{\nu+1}) \approx \int_{t_{\nu}}^{t_{\nu+1}} \int_{\Gamma_0} \psi \left( \frac{\varphi_{\nu+1}(s) - \varphi_{\nu}(s)}{t_{\nu+1} - t_{\nu}} \right) |\varphi'(s, t)| ds dt, \quad (3.81)$$

or, exchanging the order of integration,

$$D(\varphi_\nu, \varphi_{\nu+1}) \approx (t_{\nu+1} - t_\nu) \int_{\Gamma_0} \psi \left( \frac{\varphi_{\nu+1}(s) - \varphi_\nu(s)}{t_{\nu+1} - t_\nu} \right) \lambda_{\nu \rightarrow \nu+1}(s) ds, \quad (3.82)$$

where

$$\lambda_{\nu \rightarrow \nu+1}(s) = \frac{1}{t_{\nu+1} - t_\nu} \int_{t_\nu}^{t_{\nu+1}} |\varphi'(s, t)| dt \quad (3.83)$$

is the average stretch ratio of the dislocation line over the interval  $[t_\nu, t_{\nu+1}]$ . A further approximation by recourse to the generalized trapezoidal rule gives, explicitly,

$$\lambda_{\nu \rightarrow \nu+1}(s) \approx (1 - \gamma) |\varphi'_\nu(s)| + \gamma |\varphi'_{\nu+1}(s)|, \quad (3.84)$$

with  $\gamma \in [0, 1]$ .

### Monopole discretization of the dislocation measure

Next, we turn to the question of spatial discretization of the incremental minimum problem (3.78) and the weak form of the transport equation (3.23). The structure of these problems reveals the need for two types of approximations: i) the discretization of the dislocation measure  $\alpha_{\nu+1}$ , and ii) the discretization of the transport map  $\varphi_{\nu+1}$ . We consider these two approximations in turn.

As already noted, the dislocation measure  $\alpha_{\nu+1}$  enters (3.78) and (3.77) linearly and undifferentiated. In addition, the regularized energy (3.60) is finite for general measures, including Dirac atoms. Therefore, a natural and computationally convenient spatial discretization of the dislocation measure is as a linear combination of *dislocation monopoles*, i.e.,

$$\alpha_\nu = \sum_{a=1}^M \mathbf{b}_{a,\nu} \otimes \boldsymbol{\xi}_{a,\nu} \delta_{\mathbf{x}_{a,\nu}}, \quad (3.85)$$

where  $\mathbf{x}_{a,\nu}$  is the position of monopole  $a$  at time  $t_\nu$ ,  $\mathbf{b}_{a,\nu}$  is its Burgers vector,  $\boldsymbol{\xi}_{a,\nu}$  its element of line,  $\delta_{\mathbf{x}_{a,\nu}}$  is the Dirac-delta distribution centered at  $\mathbf{x}_{a,\nu}$ , and  $M$  is the number of dislocation monopoles. It bears emphasis that Equation (3.85) represents a totally *unstructured* monopole ensemble and that no connectivity or sequencing between the monopoles is implied by the representation.

For dislocation measures of the form (3.85), the push-forward (3.23) reduces to

$$\sum_{p=1}^M (\mathbf{b}_{a,\nu+1} \otimes \boldsymbol{\xi}_{a,\nu+1}) \cdot \boldsymbol{\eta}(\mathbf{x}_{a,\nu}) = \sum_{p=1}^M (\mathbf{b}_{a,\nu} \otimes \nabla \varphi_{a,\nu} \boldsymbol{\xi}_{a,\nu}) \cdot \boldsymbol{\eta}(\mathbf{x}_{a,\nu}), \quad (3.86)$$

which must be satisfied for all test functions  $\boldsymbol{\eta}$ . Therefore, we must have

$$\mathbf{b}_{a,\nu+1} = \mathbf{b}_{a,\nu}, \quad (3.87a)$$

$$\boldsymbol{\xi}_{a,\nu+1} = \nabla \varphi_{\nu \rightarrow \nu+1}(\mathbf{x}_{a,\nu}) \boldsymbol{\xi}_{a,\nu}, \quad (3.87b)$$

i.e., the monopoles carry a constant Burgers vector and the element of line of every monopole is advected by the local gradient of the incremental transport map

$$\varphi_{\nu \rightarrow \nu+1} = \varphi_{\nu+1} \circ \varphi_{\nu}^{-1}. \quad (3.88)$$

Thus, in the absence of topological transitions, i.e., if the incremental transport map is continuous, the weak reformulation of the dislocation transport problem results trivially in *Burgers vector conservation*, simply by keeping the Burgers vector of all monopoles constant. In addition, the requisite null-divergence property of the dislocation measure is ensured by the geometrically-exact character of the push-forward operations (3.87).

### Spatial discretization of the incremental transport map

A full spatial discretization additionally requires the interpolation of the incremental transport map  $\varphi_{\nu \rightarrow \nu+1}$ . Since  $\varphi_{\nu \rightarrow \nu+1}$  and its variations enter the governing equations (3.78) and (3.23) differentiated, its interpolation must be conforming. To this end, we consider general linear interpolation schemes of the form

$$\varphi_{\nu \rightarrow \nu+1}(\mathbf{x}) = \mathbf{x} + \sum_{a=1}^M (\mathbf{x}_{a,\nu+1} - \mathbf{x}_{a,\nu}) N_{a,\nu}(\mathbf{x}), \quad (3.89)$$

with gradient

$$\nabla \varphi_{\nu \rightarrow \nu+1}(\mathbf{x}) = \mathbf{I} + \sum_{a=1}^M (\mathbf{x}_{a,\nu+1} - \mathbf{x}_{a,\nu}) \otimes \nabla N_{a,\nu}(\mathbf{x}), \quad (3.90)$$

where  $a$  again indexes the dislocation monopoles,  $\{N_{a,\nu}\}_{a=1}^M$  are consistent shape functions at time  $t_\nu$  and  $\{\mathbf{x}_{a,\nu}\}_{a=1}^M$  and  $\{\mathbf{x}_{a,\nu+1}\}_{a=1}^M$  are the arrays of monopole coordinates at time  $t_\nu$  and  $t_{\nu+1}$ , respectively. Consistency here means, specifically, that the shape functions satisfy the identity

$$\sum_{a=1}^M N_{a,\nu}(\mathbf{x}) = 1, \quad (3.91a)$$

ensuring an exact dislocation update for a uniform translation of all the monopoles. An example of consistent mesh-free interpolation is given in Appendix A.

### Incremental equilibrium equations

Inserting interpolation (3.90) into (3.87b), we obtain the relation

$$\boldsymbol{\xi}_{a,\nu+1} = \boldsymbol{\xi}_{a,\nu} + \left( \sum_{b=1}^M (\mathbf{x}_{b,\nu+1} - \mathbf{x}_{b,\nu}) \nabla N_{b,\nu}(\mathbf{x}_{a,\nu}) \right) \cdot \boldsymbol{\xi}_{a,\nu}, \quad (3.92)$$

which defines a geometrical update for the monopole elements of line. This relation in turn reveals that the updated elements of line  $\{\boldsymbol{\xi}_{a,\nu+1}\}_{a=1}^M$  are fully determined by the updated monopole positions  $\{\mathbf{x}_{a,\nu+1}\}_{a=1}^M$ . Thus, the updated elements of line are not independent variables but are tied to the updated monopole positions. We may therefore render the incremental energy-dissipation function  $F$  a sole function of the updated monopole positions by inserting interpolation (3.85) into (3.77) with all elements of line updated as in (3.92). The corresponding incremental equilibrium equations then follow as

$$\begin{aligned} \mathbf{f}_{a,\nu+1} &= \frac{\partial F}{\partial \mathbf{x}_{a,\nu+1}} = \sum_{b=1}^M \left( \frac{\partial F}{\partial \mathbf{x}_{a,\nu+1}} + \frac{\partial F}{\partial \boldsymbol{\xi}_{b,\nu+1}} \frac{\partial \boldsymbol{\xi}_{b,\nu+1}}{\partial \mathbf{x}_{a,\nu+1}} \right) \\ &= \sum_{b=1}^M \left( \frac{\partial F}{\partial \mathbf{x}_{a,\nu+1}} + \frac{\partial F}{\partial \boldsymbol{\xi}_{b,\nu+1}} \nabla N_{a,\nu}(\mathbf{x}_{b,\nu}) \cdot \boldsymbol{\xi}_{b,\nu} \right) = 0, \end{aligned} \quad (3.93)$$

where we have made use of the update (3.92). We note that the effective forces  $\{\mathbf{f}_{a,\nu+1}\}_{a=1}^M$  on the monopoles comprise a direct term, corresponding to the direct dependence of  $F$  on the updated monopole positions, and a geometrical term resulting from the dependence of  $F$  on the updated monopole elements of line.

### Incremental dissipation

Inserting the monopole approximation (3.85) into the incremental dissipation (3.82), we obtain

$$\begin{aligned} D(\{\mathbf{x}_{a,\nu}\}_{a=1}^M, \{\mathbf{x}_{a,\nu+1}\}_{a=1}^M) &\approx \\ (t_{\nu+1} - t_{\nu}) \sum_{a=1}^M \psi \left( \frac{\mathbf{x}_{a,\nu+1} - \mathbf{x}_{a,\nu}}{t_{\nu+1} - t_{\nu}} \right) &\left( (1 - \gamma) |\boldsymbol{\xi}_{a,\nu}| + \gamma |\boldsymbol{\xi}_{a,\nu+1}| \right) ds, \end{aligned} \quad (3.94)$$

where we have used (3.84) and  $\{\boldsymbol{\xi}_{a,\nu+1}\}_{a=1}^M$  is tied to  $\{\mathbf{x}_{a,\nu+1}\}_{a=1}^M$  through the geometrical update (3.92). It follows from (3.93) that the corresponding monopole forces (3.93) consist of a direct term and a geometrical term. The direct term encodes the dislocation mobility law whereas the geometrical term takes into account the advection and stretching of the dislocation line. We note that the geometrical term vanishes for the particular choice  $\gamma = 0$ .

## Regularized linear elasticity

Inserting the monopole representation (3.85) into the regularized energy (3.71), we obtain

$$E^\epsilon(\{\mathbf{x}_{a,\nu+1}\}_{a=1}^M) = \sum_{a=1}^M E_{a,\nu+1}^\epsilon + \sum_{a=1}^M \sum_{\substack{b=1 \\ b \neq a}}^M E_{ab,\nu+1}^\epsilon, \quad (3.95)$$

where

$$\begin{aligned} E_{ab,\nu+1}^\epsilon &= -\frac{\mu}{4\pi} S^\epsilon(\mathbf{x}_{a,\nu+1}, \mathbf{x}_{b,\nu+1}) (\mathbf{b}_{a,\nu+1} \times \mathbf{b}_{b,\nu+1}) \cdot (\boldsymbol{\xi}_{a,\nu+1} \times \boldsymbol{\xi}_{b,\nu+1}) \\ &+ \frac{\mu}{8\pi} S^\epsilon(\mathbf{x}_{a,\nu+1}, \mathbf{x}_{b,\nu+1}) (\mathbf{b}_{a,\nu+1} \cdot \boldsymbol{\xi}_{a,\nu+1}) (\mathbf{b}_{b,\nu+1} \cdot \boldsymbol{\xi}_{b,\nu+1}) \\ &+ \frac{\mu}{8\pi(1-\nu)} (\mathbf{b}_{a,\nu+1} \times \boldsymbol{\xi}_{a,\nu+1}) \cdot \mathbf{T}^\epsilon(\mathbf{x}_{a,\nu+1}, \mathbf{x}_{b,\nu+1}) \cdot (\mathbf{b}_{b,\nu+1} \times \boldsymbol{\xi}_{b,\nu+1}), \end{aligned} \quad (3.96)$$

is the interaction energy between monopoles  $a$  and  $b$ . In addition, the self-energy of the monopoles is obtained by taking the limit of  $\mathbf{x}_b \rightarrow \mathbf{x}_a$ , with the explicit result

$$E_{a,\nu+1}^\epsilon = \frac{\mu}{8\pi} \frac{1}{2\epsilon} (\mathbf{b}_{a,\nu+1} \cdot \boldsymbol{\xi}_{a,\nu+1})^2 + \frac{\mu}{8\pi(1-\nu)} \frac{1}{3\epsilon} |\mathbf{b}_{a,\nu+1} \times \boldsymbol{\xi}_{a,\nu+1}|^2. \quad (3.97)$$

The essential role of the regularization of the elastic energy is clear in these expressions. In particular, the self-energy of the monopoles is finite but diverges as  $\epsilon \rightarrow 0$ , as expected.

We note that the self-energy (3.97) of the monopoles depends on the angle subtended by the Burgers vector and the element of line. This dependence introduces a *line-tension anisotropy* that favors certain monopole directions over others. For instance, in the usual range of  $\nu > 0$ , screw monopoles,  $\mathbf{b} \times \boldsymbol{\xi} = \mathbf{0}$ , have lower energy than—and therefore are favored over—edge monopoles  $\mathbf{b} \cdot \boldsymbol{\xi} = 0$ . In BCC crystals, this line-tension anisotropy is specially pronounced, resulting in a proliferation of long screw segments.

Applications are often concerned with the motion of dislocations under the action of an applied stress  $\boldsymbol{\sigma}^\infty$ . The effect of the applied stress is to add the term

$$E^{\text{ext}}(\{\mathbf{x}_{a,\nu+1}\}_{a=1}^M) = \sum_{a=1}^M ((\boldsymbol{\sigma}^\infty \mathbf{b}_{a,\nu+1}) \times \boldsymbol{\xi}_{a,\nu+1}) \cdot \mathbf{x}_{a,\nu+1} \quad (3.98)$$

to the total energy. Rearranging terms, we can alternatively write (3.98) in the form

$$E^{\text{ext}}(\{\mathbf{x}_{a,\nu+1}\}_{a=1}^M) = -V \boldsymbol{\sigma}^\infty \cdot \boldsymbol{\epsilon}_{\nu+1}^p, \quad (3.99)$$

cf. eq. (3.28), where

$$\boldsymbol{\epsilon}_{\nu+1}^p = -\frac{1}{V} \sum_{a=1}^M \mathbf{b}_{a,\nu+1} \odot (\boldsymbol{\xi}_{a,\nu+1} \times \mathbf{x}_{a,\nu+1}) \quad (3.100)$$

is the effective or *macroscopic plastic strain*,  $V$  is a macroscopic volume and  $\mathbf{a} \odot \mathbf{b} = (\mathbf{a} \otimes \mathbf{b} + \mathbf{b} \otimes \mathbf{a})/2$  denotes the symmetric dyadic product of vectors  $\mathbf{a}$  and  $\mathbf{b}$ .

In computing all contributions to the energy, we regard the updated monopoles element of line  $\{\boldsymbol{\xi}_{a,\nu+1}\}_{a=1}^M$  as tied to updated monopole positions  $\{\mathbf{x}_{a,\nu+1}\}_{a=1}^M$  through the geometrical update (3.92). The corresponding energetic forces on the monopoles then comprise direct terms, resulting from the dependence of the energy on the updated monopole positions, and geometrical terms, resulting from the dependence of the energy on the updated monopole elements of line.

### Summary of update algorithm

---

**Algorithm 1** Optimal transport of dislocation monopoles.

---

- 1: Compute shape functions  $\{N_{a,\nu}\}_{a=1}^M$  and  $\{\nabla N_{a,\nu}\}_{a=1}^M$  from  $\{\mathbf{x}_{a,\nu}\}_{a=1}^M$ .
  - 2: Solve incremental equilibrium equations:  $\mathbf{f}_{a,\nu+1} = 0$  for  $\{\mathbf{x}_{a,\nu+1}\}_{a=1}^M$ .
  - 3: Update monopole line elements  $\{\boldsymbol{\xi}_{a,\nu}\}_{a=1}^M$ , including splitting.
  - 4: Reset  $\nu \leftarrow \nu + 1$ , go to (1).
- 

The monopole time-stepping algorithm is summarized in Algorithm 1. The forward solution has the usual structure of implicit time-integration and updated-Lagrangian schemes. The updated monopole positions are computed by solving the incremental equilibrium equations (3.93). The update of the monopole line elements is then effected explicitly through the push-forward operations (3.87). In calculations, we solve the equilibrium equations (3.93) using the Polak-Ribière iterative solver [121] or *Scalable Nonlinear Equations Solvers (SNES)* in the PETSc library of the Argonne National Laboratory [122].

The scheme leaves considerable latitude as regards the choice of shape functions for the interpolation of the transport maps. A particularly powerful method for formulating interpolation schemes of any order is provided by maximum-entropy inference [101]. The details of this approach, as it applies in the present context, are summarized in Appendix A. We note that max-ent interpolation introduces a range of interaction  $h_a = 1/\beta_a^2$  for every monopoles, where  $\{\beta_a\}_{a=1}^M$  are parameters of the interpolation. Specifically, the transport map at monopole  $a$ , and derivatives

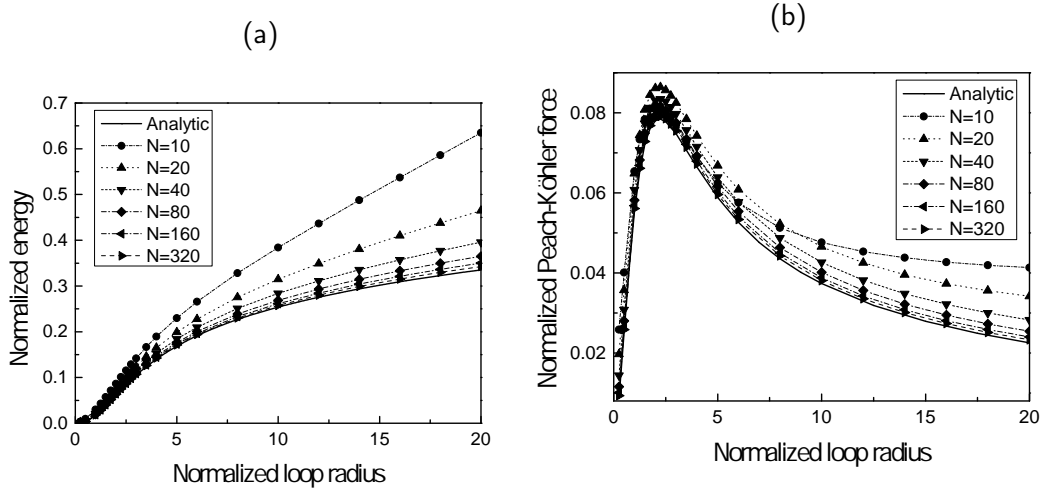


Figure 3.4: Convergence with respect to the number of monopoles for a circular prismatic loop. a) Regularized elastic energy normalized by  $\frac{\mu b^2 \rho^2}{8\pi(1-\nu)\epsilon}$ . b) Regularized Peach-Koehler force normalized by  $\frac{\mu b^2}{8\pi(1-\nu)\epsilon}$ . Loop radius normalized by  $\epsilon$ .

thereof, depends predominantly on the cluster of monopoles in the  $h_a$ -neighborhood. A simple form of *adaptivity* is to tie the parameters  $\{\beta_a\}_{a=1}^M$  to the length of the corresponding line elements through the constraint

$$\beta_a |\xi_a|^2 = \text{constant}. \quad (3.101)$$

In all calculations presented subsequently, we set the constant to  $1/2$ .

While a complete analysis of convergence is beyond the scope of this thesis, we illustrate the convergence properties of the monopole approximation by means of the simple example of a circular prismatic loop. Figure 3.4 illustrates the convergence of the regularized energy and Peach-Koehler force per unit length with respect to the number of monopoles. As may be seen from the figure, coarse discretizations of the loop tend to be overly stiff and overestimate the energy and Peach-Koehler force per unit length. The convergence of the monopole approximation with increasing number of monopoles is also evident in the figure.

### 3.7 Topological Transitions

The preceding developments are predicated on the assumption that the transport maps are continuous. Under such conditions, the topology of the dislocation measure remains invariant. In particular, the Burgers vectors of the monopoles remain constant through the motion—Equation (3.87a). In actual dislocation

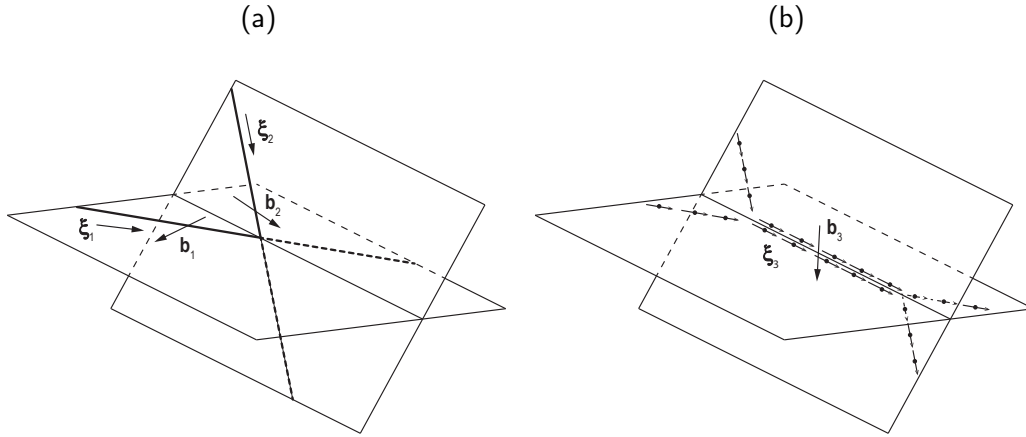


Figure 3.5: Schematic of junction formation. Two intersecting glissile dislocation lines of Burgers vectors  $\mathbf{b}_1$  and  $\mathbf{b}_2$  zip up along a line of direction  $\boldsymbol{\xi}$  on the intersection between their slip planes to form a sessile segment of Burgers vector  $\mathbf{b}_3 = \mathbf{b}_1 + \mathbf{b}_2$ .

dynamics, topological transitions occur due to a number of processes, including dislocation nucleation, dislocation reactions and junction formation, among others (cf., e.g., [40]). Topological transitions require additional logic, or 'rules', to be added to the monopole dynamics. Some basic topological transitions that play a role in subsequent calculations are discussed next.

### Dislocation reactions

Topological transitions may result from *monopole-monopole reactions* of the type

$$\mathbf{b}_1 \otimes \boldsymbol{\xi}_1 \delta_x + \mathbf{b}_2 \otimes \boldsymbol{\xi}_2 \delta_x \rightarrow \mathbf{b}_3 \otimes \boldsymbol{\xi}_3 \delta_x, \quad (3.102)$$

subject to the Burgers-vector conservation constraint

$$\mathbf{b}_1 + \mathbf{b}_2 = \mathbf{b}_3, \quad (3.103)$$

where  $\mathbf{b}_1 \otimes \boldsymbol{\xi}_1 \delta_x$  and  $\mathbf{b}_2 \otimes \boldsymbol{\xi}_2 \delta_x$  are the precursor monopoles and  $\mathbf{b}_3 \otimes \boldsymbol{\xi}_3 \delta_x$  is the product monopole. *Pair-annihilation* represents a special type of dislocation reaction in which the reacting monopoles have equal and opposite Burgers vectors and the reaction product is a null monopole. *Junction formation*, Figure 3.5, entails another special type of dislocation reaction in which two intersecting glissile dislocation lines of Burgers vectors  $\mathbf{b}_1$  and  $\mathbf{b}_2$  zip up along a line of direction  $\boldsymbol{\xi}_3$  on the intersection between their slip planes to form a sessile segment of Burgers vector  $\mathbf{b}_3 = \mathbf{b}_1 + \mathbf{b}_2$ .

The stability of monopole-monopole reactions may be elucidated by comparing the energies before and after the reaction. Thus, before the reaction we have from

(3.95)

$$E^\epsilon = E_{\text{self}}^\epsilon + E_{\text{int}}^\epsilon, \quad (3.104)$$

where

$$\begin{aligned} E_{\text{self}}^\epsilon &= \frac{\mu}{8\pi} \frac{1}{2\epsilon} (\mathbf{b}_1 \cdot \boldsymbol{\xi}_1)^2 + \frac{\mu}{8\pi(1-\nu)} \frac{1}{3\epsilon} |\mathbf{b}_1 \times \boldsymbol{\xi}_1|^2 \\ &+ \frac{\mu}{8\pi} \frac{1}{2\epsilon} (\mathbf{b}_2 \cdot \boldsymbol{\xi}_2)^2 + \frac{\mu}{8\pi(1-\nu)} \frac{1}{3\epsilon} |\mathbf{b}_2 \times \boldsymbol{\xi}_2|^2, \end{aligned} \quad (3.105)$$

is the self-energy of the precursor monopoles, eq. (3.97), and

$$\begin{aligned} E_{\text{int}}^\epsilon &= \frac{\mu}{48\pi(1-\nu)\epsilon} \left( 3(1-\nu)(\mathbf{b}_1 \cdot \boldsymbol{\xi}_1)(\mathbf{b}_2 \cdot \boldsymbol{\xi}_2) \right. \\ &\left. - 6(1-\nu)(\mathbf{b}_1 \times \mathbf{b}_2) \cdot (\boldsymbol{\xi}_1 \times \boldsymbol{\xi}_2) + 2(\mathbf{b}_1 \times \boldsymbol{\xi}_1) \cdot (\mathbf{b}_2 \times \boldsymbol{\xi}_2) \right) \end{aligned} \quad (3.106)$$

is the interaction energy of the precursor monopoles, obtained by taking the limit of  $|\mathbf{x}_1 - \mathbf{x}_2| \rightarrow 0$  in eq. (3.96). After the reaction, the energy of the product monopole is

$$E^\epsilon = \frac{\mu}{8\pi} \frac{1}{2\epsilon} (\mathbf{b}_3 \cdot \boldsymbol{\xi}_3)^2 + \frac{\mu}{8\pi(1-\nu)} \frac{1}{3\epsilon} |\mathbf{b}_3 \times \boldsymbol{\xi}_3|^2. \quad (3.107)$$

The *stability diagram* of the monopole-monopole reaction is

$$\Delta E^\epsilon < 0 \Rightarrow \text{stable}, \quad (3.108a)$$

$$\Delta E^\epsilon = 0 \Rightarrow \text{indifferent}, \quad (3.108b)$$

$$\Delta E^\epsilon > 0 \Rightarrow \text{unstable}, \quad (3.108c)$$

where  $\Delta E^\epsilon$  is the difference between the energies after and before the reaction.

In the particular case  $\boldsymbol{\xi}_1 = \boldsymbol{\xi}_2 = \boldsymbol{\xi}$ , a straightforward calculation using (3.103) gives

$$\Delta E^\epsilon = \frac{\mu}{16\pi\epsilon} (\mathbf{b}_1 \cdot \boldsymbol{\xi})(\mathbf{b}_2 \cdot \boldsymbol{\xi}) + \frac{\mu}{24\pi(1-\nu)\epsilon} (\mathbf{b}_1 \times \boldsymbol{\xi}) \cdot (\mathbf{b}_2 \times \boldsymbol{\xi}). \quad (3.109)$$

In addition, for this particular geometry the sequence of dipoles

$$\boldsymbol{\alpha}_h = \mathbf{b}_1 \otimes \boldsymbol{\xi} \delta_{\mathbf{x} + \epsilon_h \mathbf{e}} + \mathbf{b}_2 \otimes \boldsymbol{\xi} \delta_{\mathbf{x} - \epsilon_h \mathbf{e}}, \quad (3.110)$$

where  $\epsilon_h \downarrow 0$  and  $\mathbf{e}$  is a direction of approach, converges to the reaction product

$$\boldsymbol{\alpha} = \mathbf{b}_3 \otimes \boldsymbol{\xi} \delta_{\mathbf{x}} \quad (3.111)$$

weakly in the sense of measures, i.e.,  $\boldsymbol{\alpha}_h \rightharpoonup \boldsymbol{\alpha}$ . However, we see from (3.109) that  $\Delta E^\epsilon \neq 0$  in general. This shows that, as expected, the energy  $E^\epsilon(\boldsymbol{\alpha})$  is not weakly

continuous with respect to the dislocation measure  $\alpha$ . Eq. (3.109) also shows that  $\Delta E^\epsilon$  can be positive for some reactions, which additionally shows that  $E^\epsilon$  is not weakly lower-semicontinuous. Thus, whereas pair annihilation,  $\mathbf{b} - \mathbf{b} \rightarrow \mathbf{0}$ , and monopole splitting,  $2\mathbf{b} \rightarrow \mathbf{b} + \mathbf{b}$ , lower the energy, monopole pairing,  $\mathbf{b} + \mathbf{b} \rightarrow 2\mathbf{b}$ , increases the energy. This lack of weak lower-semicontinuity has far-reaching consequences for microstructural evolution, as the crystal can lower its energy, or *relax*, through microstructural rearrangements involving annihilation, splitting, network formation and other mechanisms [123].

In calculations, monopole reactions can be accounted for simply by introducing a *capture distance* and replacing the approaching monopoles by their reaction product if the energy is decreased. However, we note from (3.111) that general reaction products can be *rank-two* monopoles, which adds a certain complexity to the implementation.

### Loop nucleation

Dislocations are nucleated during plastic slip through a number of mechanisms including Frank-Read sources, double cross-slip and others [26]. In calculations, we model nucleation simply by introducing small loops of fixed radius  $\rho_0$ , e.g., commensurate with the radius of operation of a Frank-Read source, at prespecified source locations provided that the resolved shear force at the source is greater than the source strength. As such, given a source of strength  $b\tau_c$ , a loop will be nucleated if

$$b\tau \geq b\tau_c, \quad (3.112)$$

where the resolved shear force  $b\tau$  at the source is computed as a configurational force. In other words, we write

$$b\tau = -\frac{\Delta E^\epsilon}{\mathcal{A}}, \quad (3.113)$$

where  $\mathcal{A} = \pi\rho_0^2$  is the area of the putative loop and  $\Delta E^\epsilon = E_{\text{aft}}^\epsilon - E_{\text{bef}}^\epsilon$  is the resulting change in energy.

In light of Equations (3.112) and (3.113), the criterion for loop nucleation becomes

$$\Delta E^\epsilon \leq -b\tau_c\pi\rho_0^2. \quad (3.114)$$

After nucleation, the new loop shields the source and its operation is shut off until the loop becomes sufficiently large. This transient shielding results in the intermittent emission of loops from the sources.

### 3.8 Summary

In this chapter, we presented the theory of the method of monopoles for 3D dislocation dynamics. In doing so, we developed a new core regularization schemes that parallels that of [73], but with the added benefit that the regularization developed here is consistent with the theory of strain gradient elasticity. Next, we prove the validity of the method. First, in Chapter 4, we explore canonical examples and verify that the method of monopoles is consistent with well known results. This sets the stage for Chapter 5 where the method is used to study the evolution of increasingly complex dislocation configurations.

## Chapter 4

### VERIFICATION EXAMPLES

#### 4.1 Introduction

In the preceding chapter, we laid out the theory of the method of monopoles for dislocation dynamics and provided a numerical scheme for its implementation in infinite isotropic media. In this chapter, we apply the aforementioned theory to a series of canonical examples to show the validity of the method. We start with straight dislocations of the screw and edge type for which Chapter 2 provided the analytical elastic fields and we later consider the widely studied case of the circular prismatic loop. This will provide an opportunity to exhibit convergence and accuracy of the method through definitions that will be made explicit later.

#### 4.2 Infinite Straight Screw Dislocation

Consider the segment of screw dislocation line with positive direction along the  $x_3$ -axis as shown in Figure 4.1. The segment has length  $2L$  and is discretized using  $2M+1$  uniformly distributed monopoles so that the element of line length associated with each monopole is  $l = \frac{2L}{2M+1}$ . In light of the method of monopoles, we approximate the nonzero component of the dislocation density tensor for this segment as

$$\alpha_{33}^h = \sum_{a=-M}^{a=M} bl\delta(\mathbf{x} - \mathbf{x}_a) = \sum_{a=-M}^{a=M} \frac{2L}{2M+1} b\delta(x_1)\delta(x_2)\delta(x_3 - x_3^a), \quad (4.1)$$

where  $b$  is the magnitude of the Burgers vector of the dislocation and

$$x_3^a = al = \frac{2aL}{2M+1}, \quad a = -M, \dots, M.$$

#### Self-stresses

Using the definition of the dislocation density tensor (see equation (3.2)), the self stress of a continuous distribution of dislocations in an infinite solid  $\Omega$  can be written as [62]

$$\sigma_{ij} = \int_{\Omega} C_{ijkl} C_{pqmn} e_{lnh} G_{kp,q}(\mathbf{x} - \mathbf{x}') \alpha_{mh}(\mathbf{x}') d\mathbf{x}'. \quad (4.2)$$

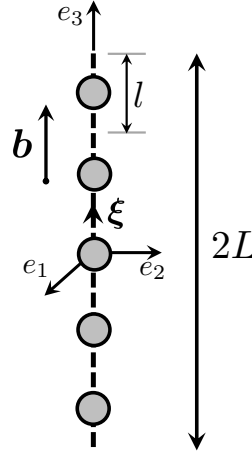


Figure 4.1: Discretization of the screw dislocation segment in the method of monopoles.

Inserting approximation (4.1) into Equation (4.2), the resulting stress field is

$$\begin{aligned}
 \sigma_{ij}^h(\mathbf{x}) &= \int_{\Omega} C_{ijkl} C_{pq3n} \epsilon_{ln3} G_{kp,q}(\mathbf{x} - \mathbf{x}') \sum_{a=-M}^{a=M} \frac{2L}{2M+1} b \delta(x'_1) \delta(x'_2) \delta(x'_3 - x_3^a) d\mathbf{x}' \\
 &= C_{ijkl} C_{pq3n} \epsilon_{ln3} b \sum_{a=-M}^{a=M} \frac{2L}{2M+1} G_{kp,q}(x_1, x_2, x_3 - x_3^a) \\
 &= (C_{ijk1} C_{pq32} - C_{ijk2} C_{pq31}) b \sum_{a=-M}^{a=M} G_{kp,q}(x_1, x_2, x_3 - x_3^a) \frac{2L}{2M+1},
 \end{aligned} \tag{4.3}$$

where we have used the sifting property of the Dirac distribution—see Equation (2.59)—to write the second equality.

For a fixed  $L$ , the last expression in (4.3) is a Riemann sum [124–126] for  $\int_{-L}^L G_{kp,q}(x_1, x_2, x_3 - x'_3) dx'_3$ . Therefore, taking the limit as  $M \rightarrow \infty$ , we get

$$\sigma_{ij}^h(\mathbf{x}) \rightarrow (C_{ijk1} C_{pq32} - C_{ijk2} C_{pq31}) b \int_{-L}^L G_{kp,q}(x_1, x_2, x_3 - x'_3) dx'_3. \tag{4.4}$$

Furthermore, in the limit  $L \rightarrow \infty$ , (4.4) becomes

$$\sigma_{ij}^h(\mathbf{x}) \rightarrow (C_{ijk1} C_{pq32} - C_{ijk2} C_{pq31}) b \int_{-\infty}^{\infty} G_{kp,q}(x_1, x_2, x_3 - x'_3) dx'_3. \tag{4.5}$$

For an isotropic medium with Lamé constant  $\lambda$  and shear modulus  $\mu$ , we have, recalling Equation (2.10),

$$C_{ijkl} = \lambda \delta_{ij} \delta_{kl} + \mu (\delta_{il} \delta_{jk} + \delta_{ik} \delta_{jl}).$$

so that (4.5) simplifies to

$$\sigma_{ij}^h \rightarrow \mu b C_{ijk1} [F_{k32}(\mathbf{x}) + F_{k23}(\mathbf{x})] - \mu b C_{ijk2} [F_{k31}(\mathbf{x}) + F_{k13}(\mathbf{x})], \quad (4.6)$$

where

$$F_{kpq}(\mathbf{x}) = \int_{-\infty}^{\infty} G_{kp,q}(x_1, x_2, x_3 - x'_3) dx'_3.$$

But recall from Equation (2.70) that the Green's tensor for an infinite isotropic medium with shear modulus  $\mu$  and Poisson ratio  $\nu$  is given by

$$G_{ij}(\mathbf{x} - \mathbf{y}) = \frac{1}{8\pi\mu|\mathbf{x} - \mathbf{y}|} \left[ 2\delta_{ij} - \frac{\delta_{ij} - T_i T_j}{2(1 - \nu)} \right]$$

so that

$$G_{ij,k}(\mathbf{x} - \mathbf{y}) = \frac{-1}{8\pi\mu|\mathbf{x} - \mathbf{y}|^2} \left[ 2\delta_{ij} T_k - \frac{\delta_{ij} T_k + \delta_{ik} T_j + \delta_{jk} T_i - 3T_i T_j T_k}{2(1 - \nu)} \right], \quad (4.7)$$

where

$$\mathbf{T} = \frac{\mathbf{x} - \mathbf{y}}{|\mathbf{x} - \mathbf{y}|}.$$

It follows that  $F_{k32}$ ,  $F_{k23}$ ,  $F_{k31}$ , and  $F_{k13}$  evaluate to zero for  $k = 1, 2$ . Likewise,  $F_{323} = F_{313} = 0$ . However,  $F_{332}$  and  $F_{331}$  evaluate respectively to

$$-\frac{1}{2\pi\mu} \frac{x_2}{x_1^2 + x_2^2}$$

and

$$-\frac{1}{2\pi\mu} \frac{x_1}{x_1^2 + x_2^2}.$$

Therefore, we obtain

$$\begin{aligned} \sigma_{ij}^h(\mathbf{x}) &\rightarrow \mu b C_{ij31} F_{332}(\mathbf{x}) - \mu b C_{ij32} F_{331}(\mathbf{x}) \\ &\rightarrow \mu^2 b (\delta_{i3} \delta_{j1} + \delta_{i1} \delta_{j3}) F_{332}(\mathbf{x}) - \mu^2 b (\delta_{i3} \delta_{j2} + \delta_{i2} \delta_{j3}) F_{331}(\mathbf{x}). \end{aligned} \quad (4.8)$$

It is immediate that  $\sigma_{11}^h$ ,  $\sigma_{22}^h$ ,  $\sigma_{12}^h$ , and  $\sigma_{33}^h \rightarrow 0$  everywhere in the solid, whereas

$$\sigma_{13}^h(\mathbf{x}) \rightarrow -\frac{\mu b}{2\pi} \frac{x_2}{x_1^2 + x_2^2},$$

$$\sigma_{23}^h(\mathbf{x}) \rightarrow \frac{\mu b}{2\pi} \frac{x_1}{x_1^2 + x_2^2}.$$

In other words, we recover the stress expressions of Equation (2.28) as  $L, M \rightarrow \infty$ .

## Transport Equation

Recall the dislocation transport equation derived in Chapter 3:

$$\dot{\alpha}_{ij} - e_{jlk}e_{mnk}(v_m\alpha_{in})_{,l} = 0, \quad (4.9)$$

where  $\mathbf{v}$ , the dislocation velocity, is a function of the force on the dislocation.

We assume that the dislocation velocity is zero for driving forces below the Peierls barrier and that the Peierls barrier is small enough to be neglected [127]. This is an especially reasonable assumption in FCC metals where the Peierls stress is very low [128]. In this so-called "viscous drag" regime, the appropriate kinetic potential is given by Equation (3.36) and the dislocation velocity, which becomes a linear function of stress, is usually limited by the viscosity due to dislocation interaction with lattice vibrations (i.e. sound waves) [40]. Thus, in order to determine the dislocation evolution over time, it is necessary to obtain the driving forces along the dislocation. In doing so, we use the Peach-Koehler formula derived in Chapter 2 and repeated below for convenience:

$$\mathbf{f} = (\boldsymbol{\sigma} \cdot \mathbf{b}) \times \mathbf{t}, \quad (4.10)$$

where  $\mathbf{f}$  is the force per unit length,  $\boldsymbol{\sigma}$  is the total stress experienced by the dislocation,  $\mathbf{b}$  is the Burgers vector, and  $\mathbf{t}$  is the tangent to the dislocation line.

For a screw dislocation along the  $x_3$ -axis, we have  $\mathbf{t} = (0, 0, 1)$  and  $\mathbf{b} = (0, 0, b)$  with  $b > 0$  so that

$$f_i = \epsilon_{ij3}\sigma_{j3}b = \epsilon_{i13}\sigma_{13}b + \epsilon_{i23}\sigma_{23}b. \quad (4.11)$$

It has already been established that within the linear elasticity theory of dislocations, the stress field diverges logarithmically along the dislocation line. As a result, a regularization scheme must be employed to evaluate the stresses along the dislocation. Using the core regularization described in Chapter 3, the regularized force along the dislocation is obtained as

$$\begin{aligned} f_i^e &= \phi^e * \phi^e * f_i \\ &= \epsilon_{i13}\sigma_{13}^{ee}b + \epsilon_{i23}\sigma_{23}^{ee}b, \end{aligned} \quad (4.12)$$

where

$$\boldsymbol{\sigma}^{ee} = \phi^e * \phi^e * \boldsymbol{\sigma}, \quad (4.13)$$

with

$$\phi^\epsilon(\mathbf{x}) = \frac{1}{4\pi\epsilon^2|\mathbf{x}|} e^{|\mathbf{x}|/\epsilon}$$

as given in Chapter 3.

In light of this regularization, we make use of Equation (2.72) to write

$$\begin{aligned} \sigma_{\alpha\beta}^{\epsilon\epsilon}(\mathbf{x}) = & -\frac{\mu}{4\pi} \oint_L b_m \epsilon_{im\alpha} \frac{\partial S^{\epsilon\epsilon}}{\partial x'_i} dx'_\beta - \frac{\mu b}{4\pi} \oint_L b_m \epsilon_{im\beta} \frac{\partial S^{\epsilon\epsilon}}{\partial x'_i} dx'_\alpha \\ & - \frac{\mu}{4\pi(1-\nu)} \oint_L b_m \epsilon_{imk} \left( \frac{\partial^3 R^{\epsilon\epsilon}}{\partial x'_i \partial x'_\alpha \partial x'_\beta} - 2\delta_{\alpha\beta} \frac{\partial S^{\epsilon\epsilon}}{\partial x'_i} \right) dx'_k, \end{aligned} \quad (4.14)$$

where

$$R^{\epsilon\epsilon} = \phi^\epsilon * \phi^\epsilon * R = R - \epsilon e^{-R/\epsilon} + \frac{4\epsilon^2}{R} (1 - e^{-R/a}) \quad (4.15)$$

and

$$S^{\epsilon\epsilon} = \phi^\epsilon * \phi^\epsilon * \frac{1}{R} = \frac{1}{R} (1 - e^{-R/a}) - \frac{1}{2\epsilon} e^{-R/\epsilon} \quad (4.16)$$

with

$$\mathbf{R} = \mathbf{x}' - \mathbf{x} \quad \text{and} \quad R = |\mathbf{R}|. \quad (4.17)$$

Therefore, we have

$$\begin{aligned} \sigma_{13}^{\epsilon\epsilon} = & -\frac{\mu}{4\pi} \oint_L b \epsilon_{i31} \frac{\partial S^{\epsilon\epsilon}}{\partial x'_i} dx'_3 - \frac{\mu b}{4\pi} \oint_L b \epsilon_{i33} \frac{\partial S^{\epsilon\epsilon}}{\partial x'_i} dx'_1 \\ & - \frac{\mu}{4\pi(1-\nu)} \oint_L b \epsilon_{i3k} \left( \frac{\partial^3 R^{\epsilon\epsilon}}{\partial x'_i \partial x'_1 x'_3} - 2\delta_{13} \frac{\partial S^{\epsilon\epsilon}}{\partial x'_i} \right) dx'_k. \end{aligned}$$

Upon further simplification, we arrive at

$$\sigma_{13}^{\epsilon\epsilon} = -\frac{\mu b}{4\pi} \int_{-\infty}^{\infty} \frac{R_2}{R} \frac{dS^{\epsilon\epsilon}}{dR} dx'_3. \quad (4.18)$$

Similar calculations lead to

$$\sigma_{23}^{\epsilon\epsilon} = -\frac{\mu b}{4\pi} \int_{-\infty}^{\infty} \frac{R_1}{R} \frac{dS^{\epsilon\epsilon}}{dR} dx'_3. \quad (4.19)$$

Along the dislocation line, i.e. when  $x_1 = x_2 = 0$ , we have  $R_1 = R_2 = 0$ ,  $R_3 = x'_3 - x_3$  so that  $R = |x'_3 - x_3|$ . It follows that,

$$\sigma_{13}^{\epsilon\epsilon} = \sigma_{23}^{\epsilon\epsilon} = 0. \quad (4.20)$$

Therefore, by Equation (4.12), the self-force on the dislocation vanishes and as a result, the velocity is identically zero along the dislocation. Owing to Equation (4.9), this implies that  $\dot{\alpha}_{ij} = 0$ , which means that the dislocation density tensor—and thus the dislocation configuration—is constant in time. This is to be expected since it is well known that an infinite straight dislocation is an equilibrium configuration [68].

### 4.3 Infinite Straight Edge Dislocation

We now consider a segment of edge dislocation line with positive direction along the  $x_3$ -axis and with Burgers vector along the  $x_1$ -axis as shown in Figure 4.2. As in the screw case, the segment has length  $2L$  and is discretized using  $2M + 1$  uniformly distributed monopoles so that the element of line length associated with each monopole is again  $l = \frac{2L}{2M + 1}$ .

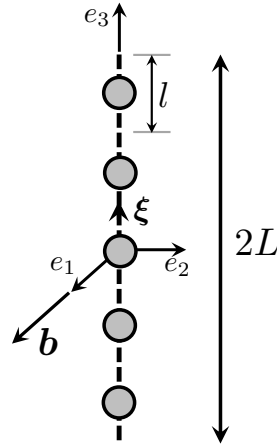


Figure 4.2: Discretization of the screw dislocation segment in the method of monopoles.

Using the method of monopoles, we approximate the nonzero component of the dislocation density tensor for this segment as

$$\alpha_{13}^h = \sum_{a=-M}^{a=M} bl\delta(\mathbf{x} - \mathbf{x}_a) = \sum_{a=-M}^{a=M} \frac{2L}{2M + 1} b\delta(x_1)\delta(x_2)\delta(x_3 - x_3^a), \quad (4.21)$$

where  $b$  is the magnitude of the Burgers vector of the dislocation segment and

$$x_3^a = al = \frac{2aL}{2M + 1}, \quad a = -M, \dots, M.$$

### Self-stresses

We proceed as before and insert the approximation (4.21) into Equation (4.2). The resulting stress field is

$$\begin{aligned}
\sigma_{ij}^h(\mathbf{x}) &= \int_{\Omega} C_{ijkl} C_{pq1n} e_{ln3} G_{kp,q}(\mathbf{x} - \mathbf{x}') \sum_{a=-M}^{a=M} \frac{2L}{2M+1} b \delta(x'_1) \delta(x'_2) \delta(x'_3 - x'_3^a) d\mathbf{x}' \\
&= C_{ijkl} C_{pq1n} e_{ln3} b \sum_{a=-M}^{a=M} \frac{2L}{2M+1} G_{kp,q}(x_1, x_2, x_3 - x_3^a) \\
&= (C_{ijk1} C_{pq12} - C_{ijk2} C_{pq11}) b \sum_{a=-M}^{a=M} G_{kp,q}(x_1, x_2, x_3 - x_3^a) \frac{2L}{2M+1}.
\end{aligned} \tag{4.22}$$

For a fixed  $L$ , the last expression in (4.22) is a Riemann sum for

$\int_{-L}^L G_{kp,q}(x_1, x_2, x_3 - x'_3) dx'_3$  so that as  $M \rightarrow \infty$ , we get

$$\sigma_{ij}^h(\mathbf{x}) \rightarrow (C_{ijk1} C_{pq12} - C_{ijk2} C_{pq11}) b \int_{-L}^L G_{kp,q}(x_1, x_2, x_3 - x'_3) dx'_3. \tag{4.23}$$

In the limit  $L \rightarrow \infty$ , we further have

$$\sigma_{ij}^h(\mathbf{x}) \rightarrow (C_{ijk1} C_{pq12} - C_{ijk2} C_{pq11}) b \int_{-\infty}^{\infty} G_{kp,q}(x_1, x_2, x_3 - x'_3) dx'_3. \tag{4.24}$$

As was done for the case of the screw dislocation segment, we plug expressions for  $C_{ijkl}$  and  $G_{ij,k}$  for the isotropic case into (4.24) and recover the stress expressions (2.41) as  $L, M \rightarrow \infty$ .

### Transport Equation

For an edge dislocation along the  $x_3$ -axis with Burgers vector in the  $x_1$ -axis, we have  $\mathbf{t} = (0, 0, 1)$  and  $\mathbf{b} = (b, 0, 0)$  with  $b > 0$  so that

$$f_i = \epsilon_{ij3} \sigma_{j1} b = \epsilon_{i13} \sigma_{11} b + \epsilon_{i23} \sigma_{21} b. \tag{4.25}$$

The regularized force along the dislocation is then obtained as

$$\begin{aligned}
f_i^\epsilon &= \phi^\epsilon * \phi^\epsilon * f_i \\
&= \epsilon_{i13} \sigma_{11}^{\epsilon\epsilon} b + \epsilon_{i23} \sigma_{21}^{\epsilon\epsilon} b,
\end{aligned} \tag{4.26}$$

where, as before,

$$\sigma^{\epsilon\epsilon} = \phi^\epsilon * \phi^\epsilon * \sigma. \tag{4.27}$$

Following a procedure similar to the screw case of the previous section, we get

$$\sigma_{11}^{\epsilon\epsilon} = \sigma_{21}^{\epsilon\epsilon} = 0. \quad (4.28)$$

Therefore, the self-force on the dislocation again vanishes and the velocity is identically zero along the dislocation. Consequently, the dislocation configuration is constant in time. Again, this is to be expected as an infinite straight dislocation is an equilibrium configuration.

It's important to note that in arriving at the above conclusions for the infinite screw and edge dislocations, no use was made of our approximation for the dislocation density tensor. Therefore, the above follows from the theory of continuous dislocation distributions rather than from the chosen approximation for  $\alpha$ . As a result, showing that our approximation recovers the stresses computed in Chapter 2 is sufficient for the straight screw and edge dislocation configurations.

#### 4.4 Circular Prismatic Dislocation Loop

In the previous examples, the monopole approximation and the theory of continuous distributions of dislocations were used to recover the expected behaviors for infinite screw and edge dislocation lines. In this section, we turn our attention to the circular prismatic dislocation case, i.e. one consisting of a circular dislocation loop whose Burgers vector is normal to the plane of the loop. This configuration has been well studied and expressions for the stress field and energy in an infinite continuum can be found analytically [68, 129, 130]. However, these expressions are often singular along the dislocation line and need to be regularized for use in determining the evolution of the dislocation [73]. In the following, we illustrate the validity of the method of monopoles for the circular prismatic dislocation loop through numerical simulations while using the discretization scheme developed in Chapter 3. In doing so, we consider the dislocation under its own self-stress and under the action of an applied external stress.

##### Climb under self-stress

It is well known that at high temperatures, a circular prismatic dislocation loop—see Figure 4.3—will shrink under the effect of its own self-stress by climb [26, 44, 76]. As seen in Chapter 3, the climb force on the dislocation is radial pointing toward the center of the dislocation. It was shown that the core regularization used in the foregoing is consistent with this result and that the monopole approximation

converges to the analytical solution derived in Chapter 3 as the number of monopoles gets large.

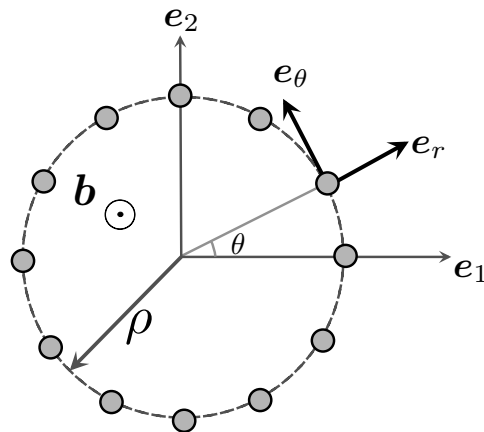


Figure 4.3: Circular prismatic dislocation loop in an elastic continuum.

Given the above convergence, we simulate the evolution of the dislocation loop of Figure 4.3. The loop lies in the  $x_1 - x_2$  plane and has Burgers vector as shown in the figure. We use the following parameters:

- ◇ Initial radius:  $\rho = 5.0$ ,
- ◇ Number of monopoles:  $M = 20$ ,
- ◇ Burgers vector:  $\mathbf{b} = (0, 0, 1)$ ,
- ◇ Climb mobility:  $M_c = 1.0 \times 10^{-2}$ ,
- ◇ Glide mobility:  $M_e = 1.0$ ,
- ◇ Time step:  $\Delta t = 0.1$ ,
- ◇ Number of time steps:  $T = 500$ ,
- ◇ Shear modulus:  $\mu = 1.0$ ,
- ◇ Poisson ratio:  $\nu = 0.3$ ,
- ◇ Regularization parameter:  $\epsilon = 1.0$ .

The monopole approximation of the initial dislocation configuration is shown in Figure 4.4 and Figure 4.5 illustrates the evolution of the dislocation over time. We note that the dislocation shrinks under the effects of its own stress field as expected.

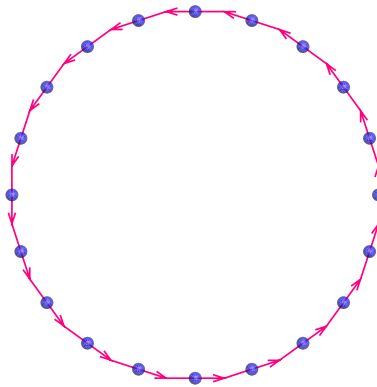


Figure 4.4: Discretization of the circular dislocation loop in the method of monopoles.

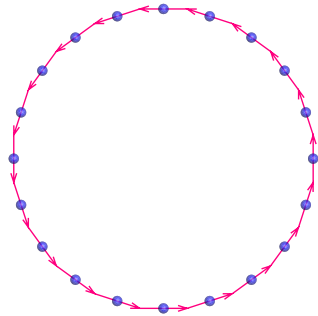
### Climb under applied stress

Next, we consider the evolution of the dislocation under the action of an external stress. As before, only the 33–component of the stress tensor is responsible for dislocation climb. As such, an external stress state  $\sigma^\infty$  is used, with all components set to zero except for the 33–component which is set to 0.05. All other parameters remain as above, with the only exception that the initial radius is now taken to be  $\rho = 1.0$ . The resulting evolution is depicted in Figure 4.6. Once again, we notice that the dislocation expands by climb while still remaining circular.

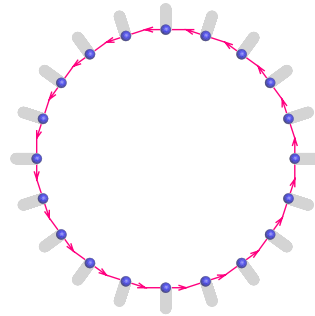
### Convergence study

We already encountered a notion of convergence when computing the regularized Peach-Koehler force on a circular prismatic dislocation loop. It was shown—see Figure 3.4b—that the force obtained from the monopole approximation approaches the analytical value as the number of monopoles gets large.

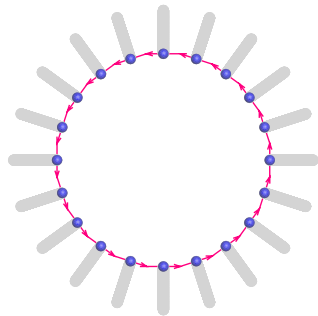
Now, we would like to investigate the accuracy of the approximation over a fixed period of time. However, because our results are qualitative in nature, we do so by investigating the "consistency" of the algorithm. More specifically, for a circular prismatic loop expanding by climb under an applied external stress  $\sigma_{33}^\infty$ , the monopoles positions  $\{\mathbf{x}_{a,\nu+1}\}_{a=1}^M$  at time  $t_{\nu+1}$  suffice to determine the corresponding elements of line  $\{\boldsymbol{\xi}_{a,\nu+1}\}_{a=1}^M$ . This is because the vector  $\boldsymbol{\xi}_{a,\nu+1}$  has the same direction as  $\boldsymbol{\xi}_{a,\nu}$  and, for uniformly distributed monopoles along the



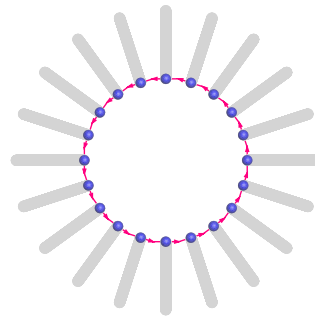
(a) Initial configuration.



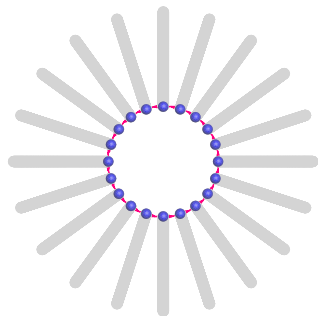
(b) After 100 time steps.



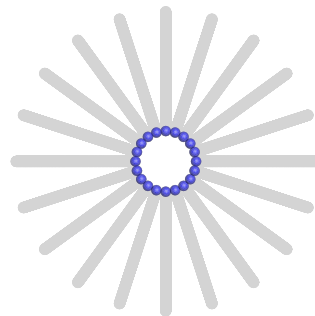
(c) After 200 time steps.



(d) After 300 time steps.



(e) After 400 time steps.

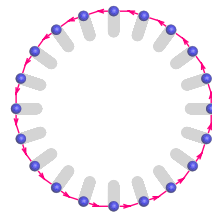


(f) After 500 time steps.

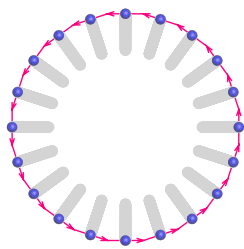
Figure 4.5: Evolution of a circular prismatic dislocation loop under its self-stress in the method of monopoles. As expected, the dislocation shrinks under its self-stress while remaining circular. The grey lines indicate the trajectories of the monopoles.



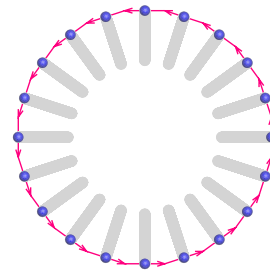
(a) Initial configuration.



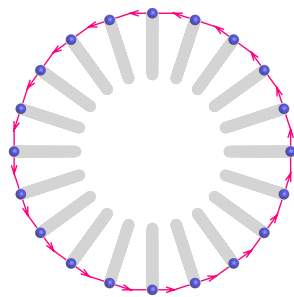
(b) After 100 time steps.



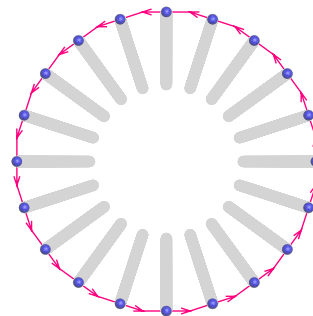
(c) After 200 time steps.



(d) After 300 time steps.



(e) After 400 time steps.



(f) After 500 time steps.

Figure 4.6: Evolution of a circular prismatic dislocation loop under the action of an applied stress  $\sigma_{33}^{\infty} > 0$ . The dislocation expands under the applied stress while remaining circular. The grey lines indicate the trajectories of the monopoles.

circular loop, has magnitude  $|\xi_{a,\nu+1}| = \frac{2\pi}{M}\rho_{\nu+1}$ , where  $\rho_{\nu+1} = |\mathbf{x}_{a,\nu+1}|$  is the same for all monopoles as the dislocation remains circular. We denote this element of line length by  $\xi_r$ .

On the other hand, for any dislocation configuration, the elements of line  $\{\xi_{a,\nu+1}\}_{a=1}^M$  at time  $t_{\nu+1}$  also follow from the new monopoles positions  $\{\mathbf{x}_{a,\nu+1}\}_{a=1}^M$  and the previous positions  $\{\mathbf{x}_{a,\nu}\}_{a=1}^M$  and elements of line  $\{\xi_{a,\nu}\}_{a=1}^M$  through equation (3.92). For the circular prismatic dislocation loop, the resulting elements of line vectors have the same magnitude and we denote the corresponding (constant) element of line length by  $\xi_t$ .

In light of the preceding, we define *consistency* of the algorithm by its ability to give the same elements of line vectors for the canonical example of the circular prismatic loop using the two methods described above. Given that the resulting elements of line computed both ways have the same directions, it suffices to focus on the magnitudes  $\xi_t$  and  $\xi_r$  of the corresponding vectors at each time step. The parameters used in the simulations are identical to those used when examining dislocation climb under self-stress, with the exception that the simulation time step is increased proportionally to the number of monopoles while the simulation time is set to  $s_T = 5.0$ . We display in Figure 4.7 the error between the corresponding element of line lengths. It is computed as  $error = \frac{|\xi_r - \xi_t|}{\rho}$ , where  $\rho$  is the initial radius of the dislocation loop. As can be seen from the figure, the error decreases with the number of monopoles. The convergence rate—or negative slope of the regression line—is computed to be 2.84.

### Monopole Splitting

Though the accuracy of the incremental transport map increases with the number of monopoles, one should notice that the (normalized) error for low numbers of monopoles is quite large, especially for the small simulation time considered. For instance, the error corresponding to  $M = 4$  monopoles is 4.21% for a simulation time of only  $s_T = 5.0$  which in this case corresponds to 6 simulation time steps. Obviously this problem can be remedied by choosing an adequately large number of monopoles *a priori*. However, this number must also depend on the length of the dislocation. Indeed, for expanding geometries, the geometrical update (3.92) results in line stretching and, potentially, in excessively long monopole line elements, with a deleterious effect on accuracy. We prevent this loss of accuracy by splitting the monopoles when they exceed a pre-specified length. In our simulations, this is

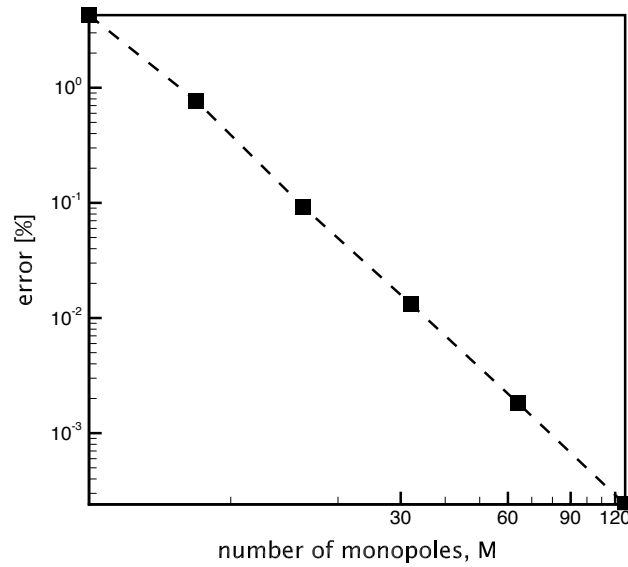


Figure 4.7: Accuracy of the algorithm in predicting the correct elements of line length. Test case of the expanding circular prismatic loop.

done when a monopole's element of line length exceeds twice the Burgers vector magnitude, i.e. when  $|\xi_a| > 2|b_a|$ ,  $a = 1 \dots M$ . We illustrate this process in the schematic of Figure 4.8. Each new monopole is centered on the associated element of line vector—which is half the parent element of line vector—and has the same Burgers vector as the parent monopole. In mathematical terms, we have

$$\xi_{a_1} = \xi_{a_2} = \frac{1}{2} \xi_a \quad (4.29a)$$

$$\mathbf{x}_{a_1} = \mathbf{x}_a - \frac{1}{4} \xi_a, \quad \mathbf{x}_{a_2} = \mathbf{x}_a + \frac{1}{4} \xi_a. \quad (4.29b)$$

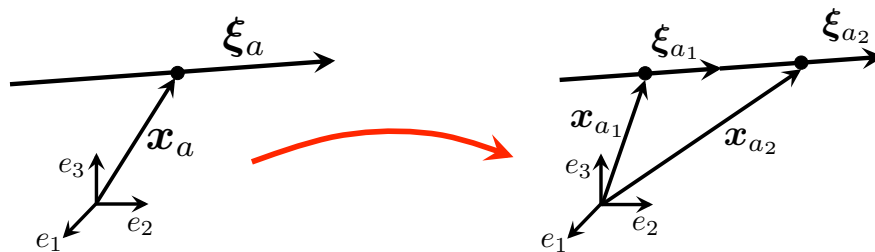


Figure 4.8: Splitting of a monopole into two new ones. The Burgers vector of each new monopole is the same as that of the parent monopole, while the element of line vector is half that of the parent monopole.

Figure 4.9 illustrates this concept for the case of an expanding circular prismatic loop with initial radius  $\rho = 1.0$ . In the illustrations of Figure 4.9, the initial number of monopoles is 8 and the numbers of time steps is 750. All other parameters remain as in Figure 4.6. It is important to emphasize the fact that the splitting procedure does not take into account the order of the monopoles. In other words, the new monopoles need not be given in sequence in the corresponding arrays. In fact, in the current implementation, new monopoles of the type  $a_2$ —see Figure 4.8—are simply recorded at the end of the corresponding arrays. As such, we cannot overstate the simplicity resulting from the line-free character of the method of monopoles.

#### 4.5 Summary

In this chapter, we demonstrated the viability of the method of monopoles for 3D dislocation dynamics. We did so by examining canonical examples in dislocation dynamics for which the expected outcome is well known. These examples included the straight edge and screw dislocations and the circular prismatic dislocation loop. In the case of the straight edge and screw dislocation, it was shown that the monopole approximation indeed recovers the singular stresses corresponding to these configurations. Furthermore, upon regularization of the dislocation cores, the dislocations did not evolve in time, which confirmed the well known fact that straight dislocations are equilibrium configurations.

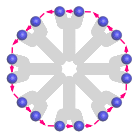
In the case of the circular prismatic loop, we successfully simulated the shrinking of the dislocation by climb under the action of its self-stress. Because of the inherent singularity along dislocation lines, this was done using the core regularization of Chapter 3. For a circular prismatic loop under the influence of applied remote stresses, we also successfully simulated the expected expansion of the dislocation. In doing so, it was necessary to develop a notion of adaptivity or monopole splitting for accuracy of the incremental transport map update. As a result, we implement the monopole splitting algorithm in the numerical examples of Chapter 5.



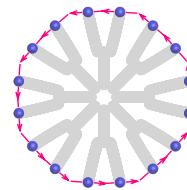
(a) Initial configuration.



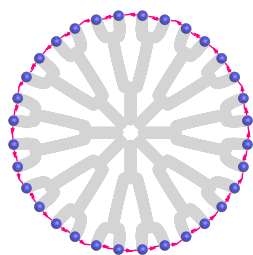
(b) After 150 time steps.



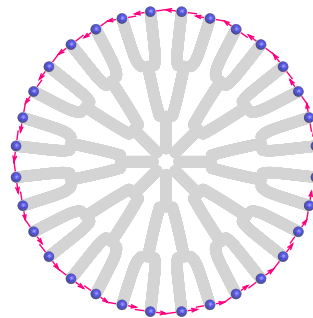
(c) After 300 time steps.



(d) After 450 time steps.



(e) After 600 time steps.



(f) After 750 time steps.

Figure 4.9: Evolution of a circular prismatic dislocation loop under the action of an applied stress  $\sigma_{33}^{\infty} > 0$  where we have implemented the splitting algorithm described in the text. The grey lines indicate the trajectories of the monopoles.

*Chapter 5*

## NUMERICAL EXAMPLES

Note: Significant content of this chapter is taken from the work of Deffo, Ariza, and Ortiz [75].

**5.1 Introduction**

In this chapter, we present selected examples of application that illustrate the range and scope of the method of monopoles presented in the foregoing. We specifically consider the case of a single BCC grain embedded in an elastic matrix. The grain has the shape of a truncated octahedron and the grain boundary is assumed to be impenetrable to dislocations. The impenetrability condition is enforced by means of a potential that penalizes monopole excursions outside the grain. The grain deforms by crystallographic slip on the 12 slip systems in the class  $\{110\}\langle 111\rangle$  under the action of a remotely applied uniaxial stress and the dislocation motion obeys linear kinetics. The calculations are carried out as described in Section 3.6 and with  $\gamma = 0$  in equation (3.84). Several scenarios of increasing complexity are considered. We emphasize that these scenarios are intended to demonstrate numerical capability and not to provide physically accurate quantitative predictions of material behavior.

**5.2 Activation of a Single Slip Plane**

We begin by considering the simplest cases of the activation of a single slip plane. In the first example, we examine the evolution of a single dislocation loop within the slip plane while in the second we consider the repeated activation of a source.

**Single dislocation loop**

In this example, we examine the case of a single loop nucleated at a source on a slip plane of arbitrary locations. A sequence of snapshots of the expanding loop is shown in Figure 5.1. The loop initially expands unimpeded and eventually arrests at the grain boundary. The example serves to illustrate how, despite the line-free character of the calculations, the monopoles nevertheless align themselves in order to attain low-energy configurations. The effectiveness of the geometrical update of the monopole line elements is also evident in the figure. In particular,

the monopoles march 'head-to-toe' in order to maintain a closed-loop, and hence divergence-free, configuration.

### **Single plane dislocation pile-up**

Figure 5.2 shows a sequence of snapshots corresponding to the case in which the source is allowed to operate repeatedly, as described in Section 3.7. As may be seen from the figure, the leading loop is followed at regular intervals by trailing loops. As multiple loops are arrested at the grain boundary, they form a pile up. The example thus demonstrates capability for repeated nucleation, loop-to-loop interaction and dislocation pile-up at grain boundaries, all of which constitute important mechanisms of dislocation multiplication and interaction.

## **5.3 Activation of a Single Slip System**

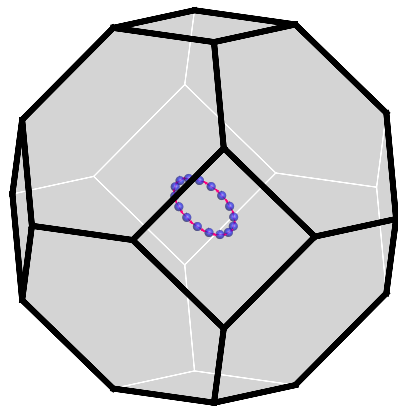
Next, we consider the evolution of dislocation loops on a single slip system. This is done through two examples as described below.

### **Parallel planes**

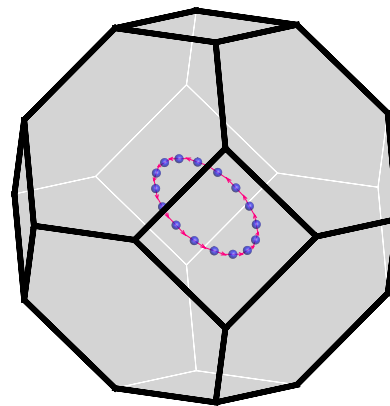
In this example, we look at dislocation loops on several parallel planes of a slip system. Each dislocation is nucleated at a random position within its plane and the ensemble is simulated over time. Figure 5.3 displays the sequence of snapshots corresponding to this setup. The dislocation loops expand within their respective planes under the action of an applied remote stress until they reach the impenetrable boundaries of the grain. It is worth emphasizing that at no point in the simulations is a connectivity or sequencing of monopoles enforced.

### **Parallel planes with dislocation pile-up**

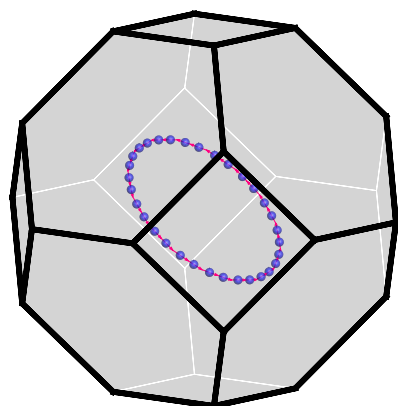
We now consider the case in which several slip planes in a slip system are allowed to operate simultaneously with regularly activated sources. We show in Figure 5.4 the corresponding sequence of snapshots. The location of the sources and slip planes is chosen at random. As in the preceding case, the sources operate repeatedly to nucleate multiple dislocation loops that expand under the action of the applied load and eventually pile up at the boundary. The example serves to illustrate the full three-dimensional character of the formulation, which allows for coplanar dislocations as well as fully-interacting dislocations on multiple planes.



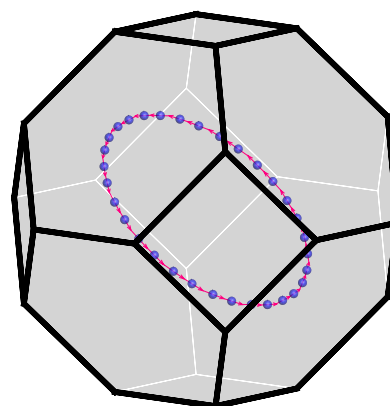
(a) Initial configuration.



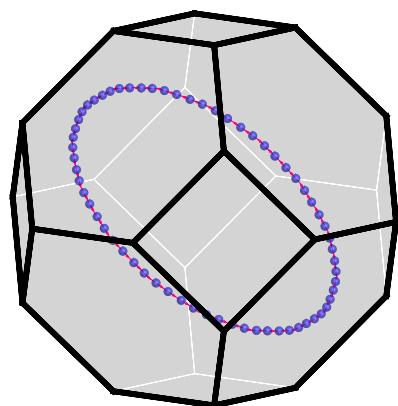
(b) After 50 time steps.



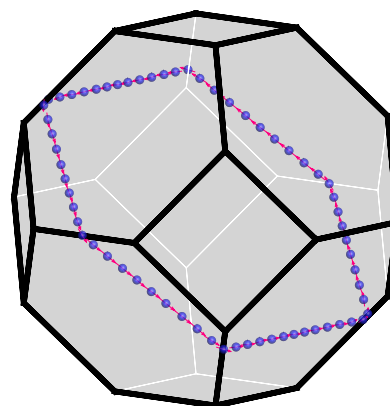
(c) After 100 time steps.



(d) After 150 time steps.

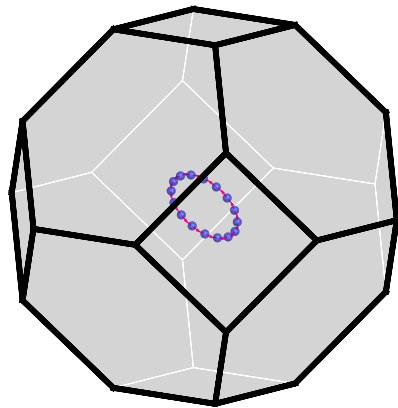


(e) After 200 time steps.

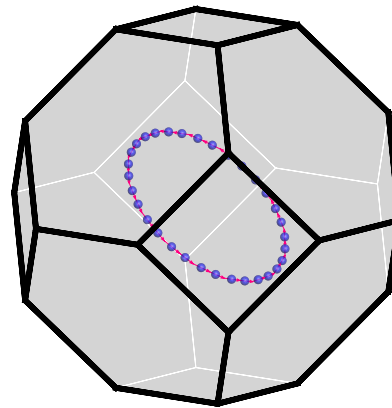


(f) Final configuration.

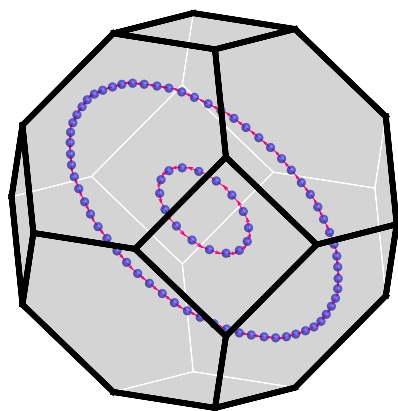
Figure 5.1: BCC grain in elastic matrix. Snapshots of single loop nucleating from a randomly-located source and expanding under the action of an applied uniaxial stress until it reaches the impenetrable boundaries of the grain.



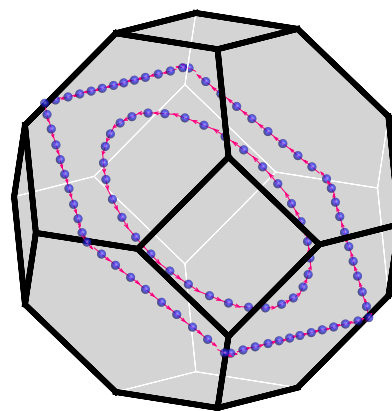
(a) Initial configuration.



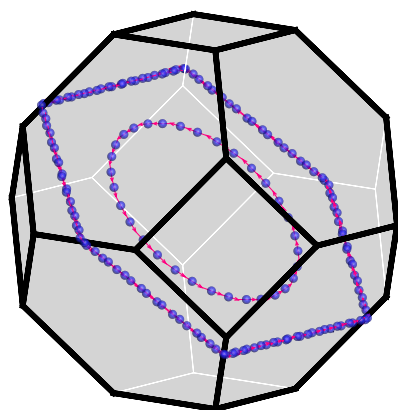
(b) After 100 time steps.



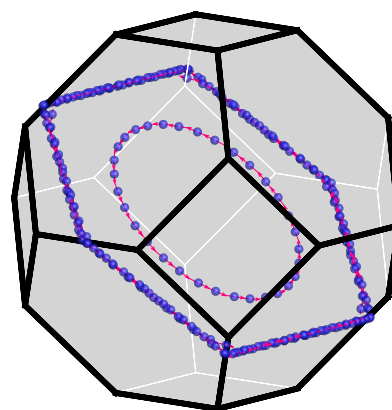
(c) After 200 time steps.



(d) After 300 time steps.

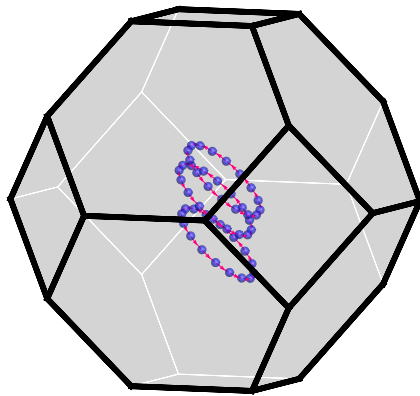


(e) After 400 time steps.

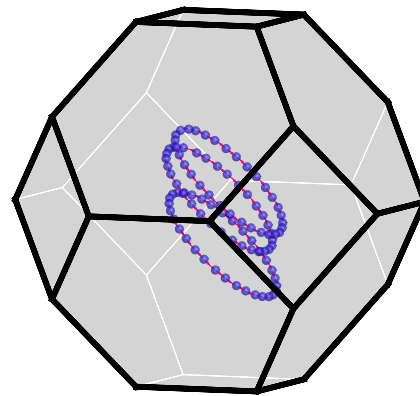


(f) After 500 time steps.

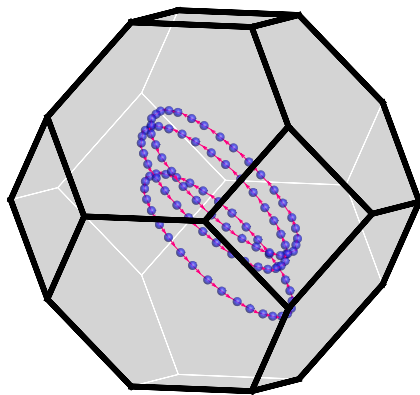
Figure 5.2: BCC grain in elastic matrix. Snapshots of multiple loops nucleating from a common randomly-located source and expanding under the action of an applied uniaxial stress until they reach the impenetrable boundaries of the grain.



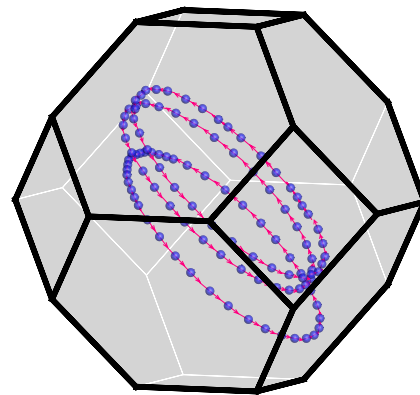
(a) Initial configuration.



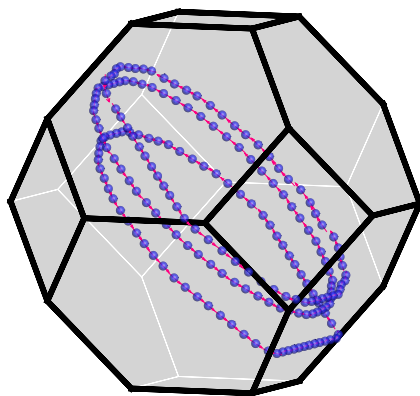
(b) After 60 time steps.



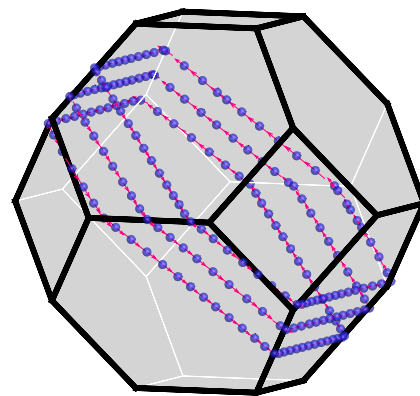
(c) After 120 time steps.



(d) After 180 time steps.

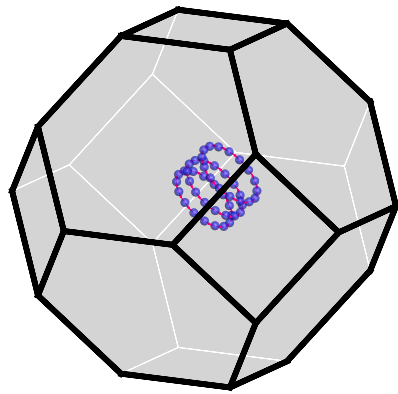


(e) After 240 time steps.

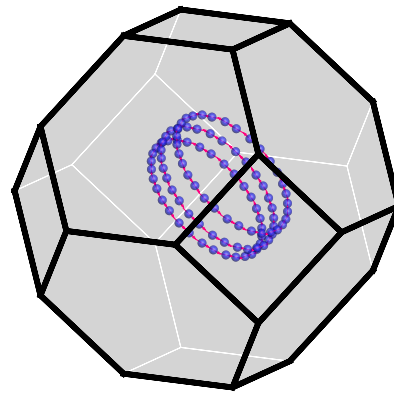


(f) Final configuration.

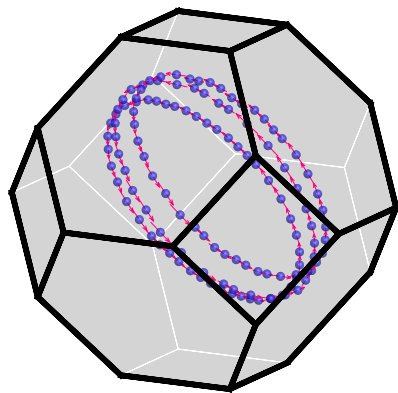
Figure 5.3: BCC grain in elastic matrix. Snapshots of single loops nucleating from randomly-located sources on multiple parallel slip planes and expanding under the action of an applied uniaxial stress until they reach the impenetrable boundaries of the grain.



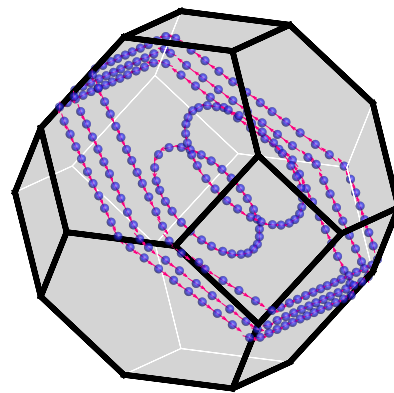
(a) Initial configuration.



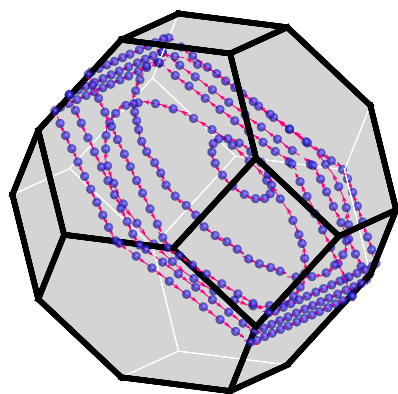
(b) After 100 time steps.



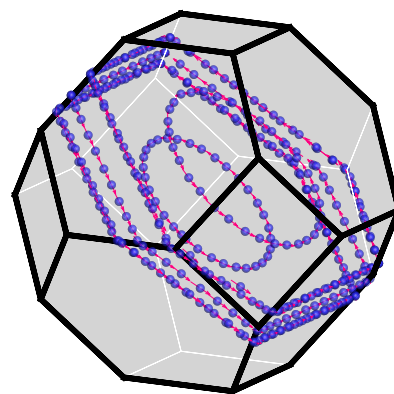
(c) After 200 time steps.



(d) After 300 time steps.



(e) After 400 time steps.



(f) After 500 time steps.

Figure 5.4: BCC grain in elastic matrix. Snapshots of multiple loops nucleating from randomly-located sources on multiple parallel slip planes and expanding under the action of an applied uniaxial stress until they reach the impenetrable boundaries of the grain.

## 5.4 Activation of Multiple Slip Systems

We finish by examining the evolution of dislocation systems on several slip systems. The first example is concerned with the case of dislocations on two slip systems while the second takes into account all slip systems in the single BCC grain.

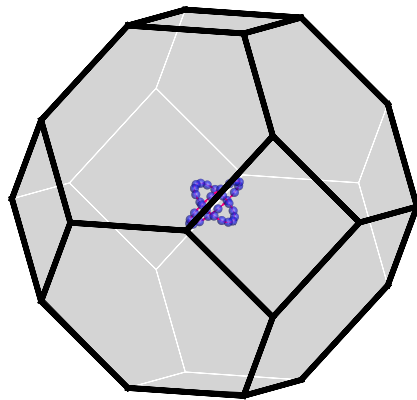
### Activation of two slip systems

In this example, we consider two dislocation loops nucleated at random sources on different planes of different slip systems—see figure 5.5a. The subsequent evolution of the ensemble under the action of a remotely applied stress is shown in figure 5.5. As in the previous examples, the dislocations expand until they reach the boundaries of the grain. Again, this is done without regard for the sequencing of the monopoles. In other words, each monopole carries information about its position, element of line vector, Burgers 'charge', and slip plane normal, and the implementation is completely blind to the connectivity of the monopoles.

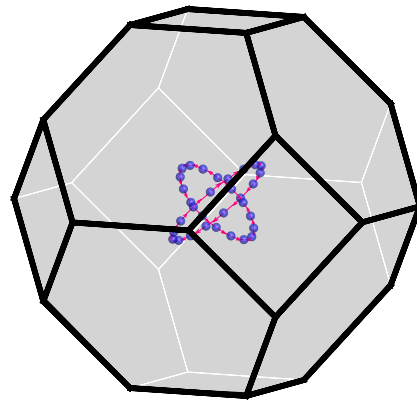
### Activation of all slip systems

Finally, Figure 5.6 displays the complex evolution of the dislocation ensemble that ensues when multiple sources, slip planes, and slip systems are allowed to operate simultaneously. In particular, the sequence of snapshots shown in the figure illustrates the ability of loops in different slip planes to interact at close range, cross each other or form structures.

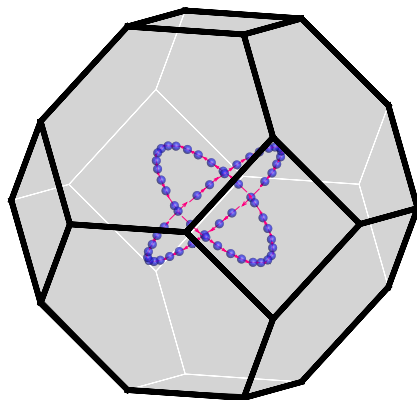
Given the ultimate goal of simulating hardening in the grain, we use Equation (3.100) to compute the stress vs. plastic strain curve corresponding to the dislocation evolution shown in Figure 5.6. The resulting output is displayed in Figure 5.7. We emphasize that all results in this thesis are qualitative in nature and as such, no quantitative comparison should be made between the curve of Figure 5.7 and experimental data, especially since the numerical examples discussed here did not explicitly implement topological changes. Nevertheless, the robust ability of the method to account for—and negotiate—the complex dislocation interactions and evolutions exemplified by the example is noteworthy and bodes well for the general application of the method to a broad range of applications.



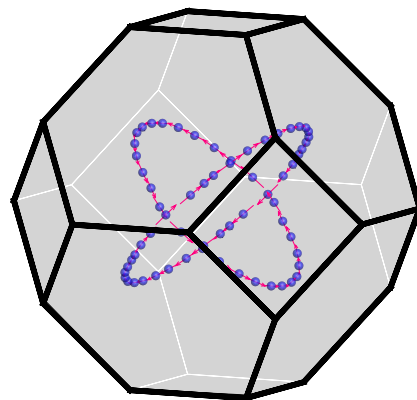
(a) Initial configuration.



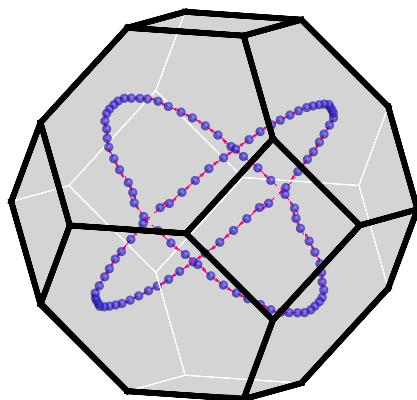
(b) After 50 time steps.



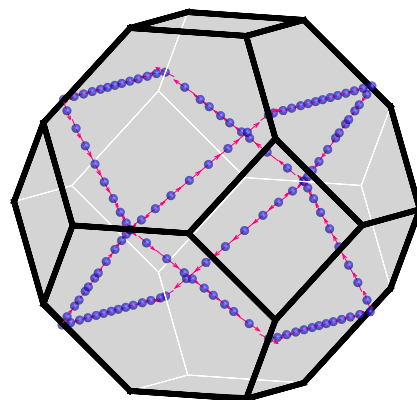
(c) After 100 time steps.



(d) After 150 time steps.

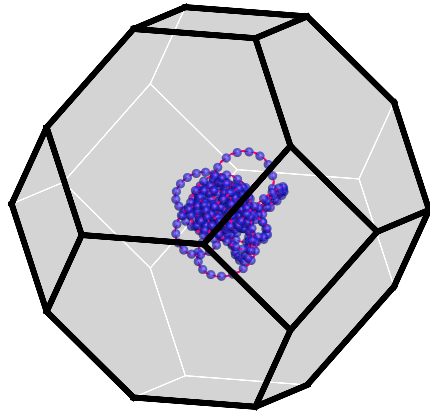


(e) After 200 time steps.

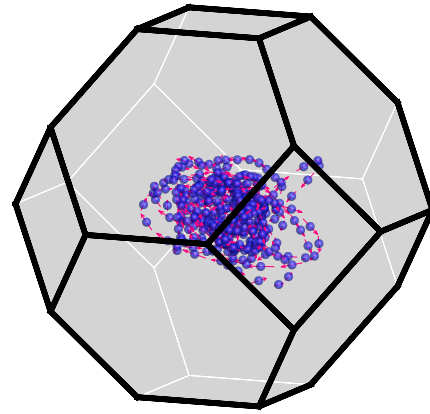


(f) Final configuration.

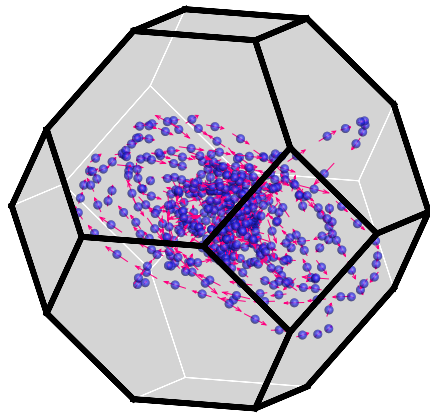
Figure 5.5: BCC grain in elastic matrix. Snapshots of two loops nucleating from two different randomly-located sources on two slip systems and subsequently expanding under the action of an applied uniaxial stress until they reach the impenetrable boundaries of the grain.



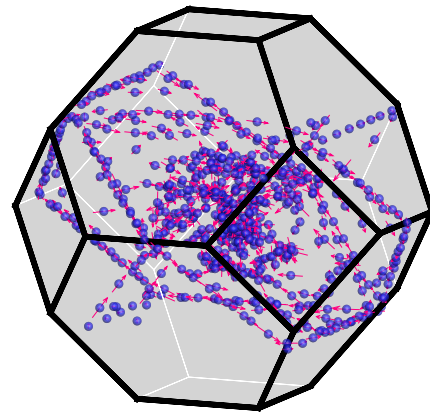
(a) Initial configuration.



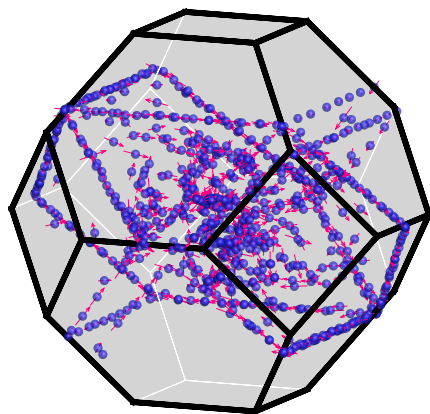
(b) After 100 time steps.



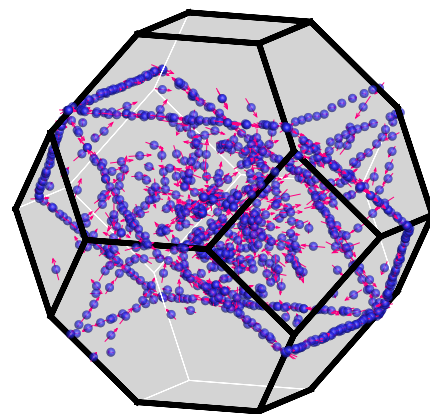
(c) After 200 time steps.



(d) After 300 time steps.



(e) After 400 time steps.



(f) After 500 time steps.

Figure 5.6: BCC grain in elastic matrix. Snapshots of multiple loops nucleating from randomly-located sources on multiple slip planes and expanding under the action of an applied uniaxial stress until they reach the impenetrable boundaries of the grain.

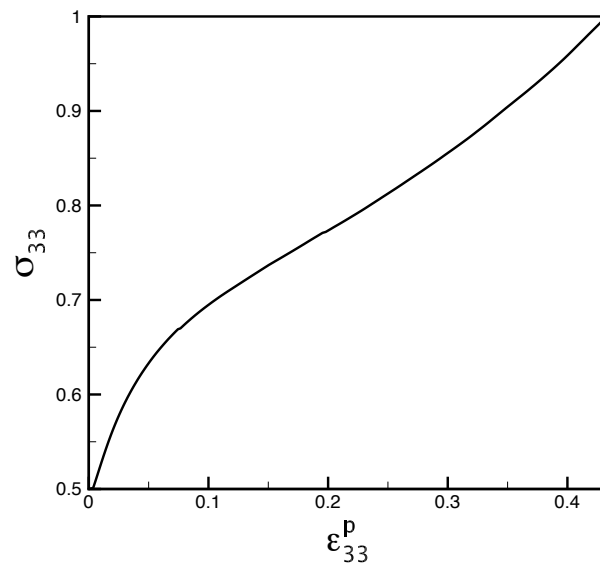


Figure 5.7: Computed plastic strain plotted against the monotonically increasing remote stress for the dislocation ensemble displayed in Figure 5.6.

## Chapter 6

### CONCLUSION

Note: Significant content of this chapter is taken from the work of Deffo, Ariza, and Ortiz [75].

#### 6.1 Summary

In this thesis, we have developed a novel approximation scheme for three-dimensional dislocation dynamics. In doing so, we have examined imperfections in crystals with emphasis on dislocations—Chapter 1. In Chapter 2, we have provided the basic framework for continuum dislocation theory after a review of classical linear elasticity. Finally, in Chapter 3, we have laid out the details of the method of monopoles.

In this method, the dislocation line density is concentrated at points, or *monopoles*. Every monopole carries a Burgers vector and an element of line. Since monopoles are Dirac masses, the monopole representation requires an extension of the classical dislocation transport problem (cf., e.g., [62]), which is restricted to 'continuously distributed dislocations', to general measures. This extension requires: i) expressing the transport Equation (3.11) in weak form—Equation (3.16); ii) expressing the elastic energy in terms of Airy stress potentials—Equation (3.55); and iii) regularizing the elastic energy—Equation (3.61). By virtue of these manipulations, the dislocation density appears *linearly* in all expressions, which thus make sense for general measures. In addition, the regularization of the elastic energy eliminates the logarithmic divergence of Volterra dislocations and assigns finite energies and Peach-Koehler forces to general dislocation measures, including monopoles.

Following concepts from optimal transportation theory (cf., e.g., [97]), we discretize the dislocation transport problem in time by introducing incremental transport maps. These maps push forward the dislocation density from one configuration to the next—Equation (3.23). For dislocation densities in the form of monopoles, this push-forward operation takes a particularly simple form—Equation (3.87): i) the Burgers vectors of the monopoles remain constant; and ii) the elements of line of the monopoles are updated according to the local gradient of the incremental transport map. It bears emphasis that these operations are geometrically exact to within

the interpolation accuracy of the transport map. In particular, the geometrical update preserves the null-divergence constraint and results in line stretching (resp. shortening) for divergent (resp. convergent) geometries, cf. figures 4.5, 4.6 and 4.9. Further adapting concepts from optimal transportation theory and, in particular, from the pioneering work of Jordan, Kinderlehrer, and Otto [98–100], we formulate an incremental minimum principle for the transport map—Equation (3.78)—that encodes the energetics and mobility kinetics of the system. In particular, the motion of the monopoles is the result of a competition between energy, which drives the monopoles to low-energy configurations, and mobility, which opposes motion. Finally, the requisite interpolation of the transport maps is effected by means of mesh-free max-ent interpolation [101].

A distinguishing attribute of the proposed method of monopoles relative to traditional approximation schemes based on segments is that an explicit linear connectivity, or ‘sequence’, between the monopoles need not be defined. In this sense, the method is ‘line-free’. The satisfaction of the requisite null-divergence constraint is ensured by the geometric exactness of the incremental updates—Equation (3.87). In addition, the monopoles tend to align ‘head-to-toe’ spontaneously in order to minimize the elastic energy. The result, which is clearly evident in the verification and numerical examples of Chapters 4 and 5, is that, while not explicitly enforced, the monopole ensemble approximates a collection of lines at all times. The examples also attest to the remarkable robustness of the method and, in particular, to its ability to negotiate complex dislocation dynamics including nucleation, close-range interactions, pileups, intersections and other mechanisms.

## 6.2 Future Work

We close by remarking that the present work has been primarily concerned with the mathematical framework, implementation, and numerical testing of the proposed method of monopoles. In particular, we have not attempted to model specific material systems or make quantitative predictions thereof with any degree of physical fidelity. Nevertheless, because the method is advertised as potentially more efficient than current line dislocation dynamics codes, upon optimization of the method of monopoles, it’d be telling to compare it with current methods for line dislocation dynamics, e.g., *microMegas* or *ParaDiS*, for the simple examples studied in the foregoing. Regardless of the outcome, there is extraordinarily extensive experience in applying dislocation dynamics to the elucidation of a vast array of physical phenomena that we believe can be combined with the proposed method to

great effect. In particular, as already noted, we believe that the method provides an effective avenue for extending to three dimensions the wealth of point-dislocation methods that have been developed and extensively applied in two dimensions, starting with the seminal paper of Lubarda, Blume, and Needleman [94]. These connections and extensions suggest themselves as worthwhile directions of future research.

One such example is the implementation of topological transitions as described in Section 3.7. Indeed, because our goal primarily has been to establish the method of monopoles as a valid approach to dislocation dynamics, in all examples of this work, we have not implemented the complex topological changes that accompany every dislocation dynamics simulation. Therefore, implementing these topological changes will provide the method with full capabilities and enable simulations of dislocation dynamics for quantitative—as opposed to purely qualitative—results that can be compared to experiments. Furthermore, given that an explicit connectivity between the monopoles need not be defined, this gives the method a natural predisposition to parallelization as monopoles could be split between processors without regard for their neighbors.

Another extension of the present work is in the implementation of linear elastic anisotropy in dislocation dynamics. It is well known [78, 131] that current line dislocation dynamics algorithms are computationally expensive for obtaining the stress field at dislocation nodes under conditions of elastic anisotropy. This is because the integrand in the integral expression for the stress field is not known analytically, which in turn is due to the fact that analytical expression for the Green's function of elasticity is known only for elastic isotropy in an infinite medium. Given that in the method of monopoles, integrals around the dislocation line are replaced by (Riemann) sums, this suggests the method could prove viable as a candidate for efficient dislocation dynamics simulations in anisotropic media.

## BIBLIOGRAPHY

- [1] Dr. Nader Engheta. *Metamaterials: What They Are and Why They're Important*. University of Pennsylvania. 2013. URL: <https://www.youtube.com/watch?v=1K4RQr7RICY>.
- [2] R. S. Kshetrimayum. "A brief intro to metamaterials". In: *IEEE Potentials* 23.5 (Dec 2004 – Jan 2005), pp. 44–46. DOI: 10.1109/MP.2005.1368916.
- [3] J.Y. Rhee et al. "Metamaterial-based perfect absorbers". In: *Journal of Electromagnetic Waves and Applications* 28.13 (2014), pp. 1541–1580. DOI: 10.1080/09205071.2014.944273.
- [4] R. A. Shelby, D. R. Smith, and S. Schultz. "Experimental Verification of a Negative Index of Refraction". In: *Science* 292.5514 (2001), pp. 77–79. ISSN: 0036-8075. DOI: 10.1126/science.1058847.
- [5] J. B. Pendry. "Negative refraction". In: *Contemporary Physics* 45.3 (2004), pp. 191–202. DOI: 10.1080/00107510410001667434.
- [6] J. B. Pendry. "Negative Refraction Makes a Perfect Lens". In: *Phys. Rev. Lett.* 85 (18 Oct. 2000), pp. 3966–3969. DOI: 10.1103/PhysRevLett.85.3966.
- [7] G. Oliveri, D. H. Werner, and A. Massa. "Reconfigurable Electromagnetics Through Metamaterials – A Review". In: *Proceedings of the IEEE* 103.7 (2015), pp. 1034–1056. DOI: 10.1109/JPROC.2015.2394292.
- [8] David R Smith. "Beating the diffraction limit". In: *Physics World* 17.5 (2004), p. 23. URL: <http://stacks.iop.org/2058-7058/17/i=5/a=31>.
- [9] J. B. Pendry, D. Schurig, and D. R. Smith. "Controlling Electromagnetic Fields". In: *Science* 312.5781 (2006), pp. 1780–1782. ISSN: 0036-8075. DOI: 10.1126/science.1125907.
- [10] D. Schurig et al. "Metamaterial Electromagnetic Cloak at Microwave Frequencies". In: *Science* 314.5801 (2006), pp. 977–980. ISSN: 0036-8075. DOI: 10.1126/science.1133628.
- [11] N. I. Landy et al. "Perfect Metamaterial Absorber". In: *Phys. Rev. Lett.* 100 (20 May 2008), p. 207402. DOI: 10.1103/PhysRevLett.100.207402.
- [12] Jeff Hawk. *The Boeing 787 Dreamliner: More Than an Airplane*. May 2005. The Boeing Company. URL: <https://web.archive.org/web/20070808001501/http://www.aiaa.org/events/aners/Presentations/ANERS-Hawk.pdf>.
- [13] George Marsh. *Composites flying high (Part 1)*. April 2014. Reinforced Plastics. URL: <https://www.materialstoday.com/composite-applications/features/composites-flying-high-part-1/>.

- [14] Airbus. *A350 XWB Family: The Xtra that makes the difference*. Accessed April 27, 2018. Airbus. URL: <http://www.airbus.com/aircraft/passenger-aircraft/a350xwb-family.html>.
- [15] K. Wang. "The use of titanium for medical applications in the USA". In: *Materials Science and Engineering: A* 213.1 (1996). International Symposium on Metallurgy and Technology of Titanium Alloys, pp. 134–137. ISSN: 0921-5093. DOI: 10.1016/0921-5093(96)10243-4.
- [16] D. F. Williams. "Titanium for Medical Applications". In: *Titanium in Medicine: Material Science, Surface Science, Engineering, Biological Responses and Medical Applications*. Berlin, Heidelberg: Springer Berlin Heidelberg, 2001, pp. 13–24. ISBN: 978-3-642-56486-4. DOI: 10.1007/978-3-642-56486-4\_2. URL: [https://doi.org/10.1007/978-3-642-56486-4\\_2](https://doi.org/10.1007/978-3-642-56486-4_2).
- [17] M. Geetha et al. "Ti based biomaterials, the ultimate choice for orthopaedic implants: A review". In: *Progress in Materials Science* 54.3 (2009), pp. 397–425. ISSN: 0079-6425. DOI: 10.1016/j.pmatsci.2008.06.004.
- [18] D. Hull and D. J. Bacon. *Introduction to Dislocations*. 4th ed. Oxford: Butterworth-Heinemann, 2001. ISBN: 978-0-7506-4681-9.
- [19] J. Friedel. *Dislocations*. International Series of Monographs on Solid State Physics, Volume 3. Pergamon Press Ltd., 1964. ISBN: 978-0-08-013523-6.
- [20] W. T. Read Jr. *Dislocations in Crystals*. International Series in Pure and Applied Physics. New York: McGraw-Hill Book Company, Inc., 1953. ISBN: 9780070512801.
- [21] B. K. Vainshtein, V. M. Fridkin, and V. L. Indenbom. *Structure of Crystals*. 2nd ed. Berlin, Heidelberg, New York: Springer-Verlag, 1994. ISBN: 3-540-56848-4.
- [22] W. Borchardt-Ott. *Crystallography*. 2nd ed. Berlin, Heidelberg, New York: Springer-Verlag, 1995. ISBN: 3-540-59478-2.
- [23] G. Q. Xu and M. J. Demkowicz. "Healing of Nanocracks by Disclinations". In: *Phys. Rev. Lett.* 111 (14 Oct. 2013), p. 145501. DOI: 10.1103/PhysRevLett.111.145501.
- [24] P. Bauman, J. Park, and D. Phillips. "Analysis of Nematic Liquid Crystals with Disclination Lines". In: *Archive for Rational Mechanics and Analysis* 205.3 (2012), pp. 795–826. ISSN: 1432-0673. DOI: 10.1007/s00205-012-0530-7.
- [25] M. Klemm and J. Friedel. "Disclinations, dislocations, and continuous defects: A reappraisal". In: *Rev. Mod. Phys.* 80 (1 Jan. 2008), pp. 61–115. DOI: 10.1103/RevModPhys.80.61.
- [26] J. P. Hirth and J. Lothe. *Theory of Dislocations*. 2nd ed. New York: John Wiley & Sons, 1982. ISBN: 0-471-09125-1.

- [27] W. F. Harris. "The geometry of disclinations in crystals". In: *Surface and Defect Properties of Solids: Volume 3*. Ed. by M. W. Roberts and J. M. Thomas. Vol. 3. The Royal Society of Chemistry, 1974, pp. 57–92. ISBN: 978-0-85186-270-5. DOI: 10.1039/9781847556967-00057.
- [28] A. E. Romanov. "Mechanics and physics of disclinations in solids". In: *European Journal of Mechanics - A/Solids* 22.5 (2003). General and plenary lectures from the 5th EUROMECH Solid Mechanics Conference, pp. 727–741. ISSN: 0997-7538. DOI: 10.1016/S0997-7538(03)00089-5.
- [29] R. deWit. "Theory of disclinations: II. Continuous and discrete disclinations in anisotropic elasticity". In: *Journal of Research of the National Bureau of Standards Section A: Physics and Chemistry* 77A.1 (1973), pp. 49–100. DOI: 10.6028/jres.077A.003.
- [30] R. deWit. "Theory of disclinations: III. Continuous and discrete disclinations in isotropic elasticity". In: *Journal of Research of the National Bureau of Standards Section A: Physics and Chemistry* 77A.3 (1973), pp. 359–368.
- [31] R. deWit. "Theory of disclinations: IV. Straight Disclinations". In: *Journal of Research of the National Bureau of Standards Section A: Physics and Chemistry* 77A.5 (1973), pp. 607–658. DOI: 10.6028/jres.077A.036.
- [32] E. Kroner and K. H. Anthony. "Dislocations and Disclinations in Material Structures: The Basic Topological Concepts". In: *Annual Review of Materials Science* 5.1 (1975), pp. 43–72. DOI: 10.1146/annurev.ms.05.080175.000355.
- [33] V. Volterra. "Sur l'équilibre des corps élastiques multiplement connexes". fre. In: *Annales scientifiques de l'École Normale Supérieure* 24 (1907), pp. 401–517. URL: <http://eudml.org/doc/81250>.
- [34] J. Frenkel. "Zur Theorie der Elastizitätsgrenze und der Festigkeit kristallinischer Körper". In: *Zeitschrift für Physik* 37.7 (1926), pp. 572–609. ISSN: 0044-3328. DOI: 10.1007/BF01397292.
- [35] A. H. Cottrell. *Theory of Crystal Dislocations*. 2nd ed. Documents on Modern Physics. New York: Gordon and Breach, 1964. ISBN: 9780677001708.
- [36] G. I. Taylor. "The mechanism of plastic deformation of crystals. Part I.—Theoretical". In: *Proceedings of the Royal Society of London A: Mathematical, Physical and Engineering Sciences* 145.855 (1934), pp. 362–387. ISSN: 0950-1207. DOI: 10.1098/rspa.1934.0106.
- [37] G. I. Taylor. "The mechanism of plastic deformation of crystals. Part II.—Comparison with observations". In: *Proceedings of the Royal Society of London A: Mathematical, Physical and Engineering Sciences* 145.855 (1934), pp. 388–404. ISSN: 0950-1207. DOI: 10.1098/rspa.1934.0107.

- [38] M. Polanyi. "Über eine Art Gitterstörung, die einen Kristall plastisch machen könnte". In: *Zeitschrift für Physik* 89.9 (Sept. 1, 1934), pp. 660–664. ISSN: 0044-3328. DOI: 10.1007/BF01341481.
- [39] E. Orowan. "Zur Kristallplastizität. III". In: *Zeitschrift für Physik* 89.9 (Sept. 1, 1934), pp. 634–659. ISSN: 0044-3328. DOI: 10.1007/BF01341480.
- [40] V. Bulatov and W. Cai. *Computer Simulations of Dislocations (Oxford Series on Materials Modelling)*. Oxford Series on Materials Modelling. New York, NY, USA: Oxford University Press, Inc., 2006. ISBN: 0198526148.
- [41] K. X. Chen et al. "Effect of dislocations on electrical and optical properties of n-type Al<sub>0.34</sub>Ga<sub>0.66</sub>N". In: *Applied Physics Letters* 93.19 (2008), p. 192108. DOI: 10.1063/1.3021076.
- [42] F. R. N. Nabarro. *Theory of Crystal Dislocations*. The International Series of Monographs on Physics. Glasgow: Oxford Clarendon Press, 1967.
- [43] R. de Wit. "The Continuum Theory of Stationary Dislocations\*\*Based on a thesis submitted in partial fulfillment of the requirements for the degree of Doctor of Philosophy at the University of Illinois, February, 1959." In: ed. by Frederick Seitz and David Turnbull. Vol. 10. *Solid State Physics*. Academic Press, 1960, pp. 249–292. DOI: [https://doi.org/10.1016/S0081-1947\(08\)60703-1](https://doi.org/10.1016/S0081-1947(08)60703-1).
- [44] R. W. Lardner. *Mathematical Theory of Dislocations and Fracture*. Mathematical Expositions No. 17. Toronto: University of Toronto Press, 1974. ISBN: 0-8020-5277-0.
- [45] A. E. H. Love. *A Treatise on the Mathematical Theory of Elasticity*. 4th ed. New York: Dover Publications, 1944. ISBN: 0-486-60174-9.
- [46] S. Timoshenko and J. N. Goodier. *Theory of Elasticity*. 2nd ed. Engineering Societies Monographs. New York: McGraw-Hill Book Company, Inc., 1951. ISBN: 978-0070647190.
- [47] I. S. Sokolnikoff. *Mathematical Theory of Elasticity*. 2nd ed. New York: McGraw-Hill Book Company, Inc., 1956.
- [48] L. D. Landau and E. M. Lifshitz. *Theory of Elasticity*. 3rd ed. Course of Theoretical Physics Volume 7. Oxford: Pergamon Press, 1986.
- [49] M. H. Sadd. *Elasticity – Theory, Applications, and Numerics*. Amsterdam: Elsevier Butterworth-Heinemann, 2005. ISBN: 0-12-605811-3.
- [50] A. F. Bower. *Applied Mechanics of Solids*. Boca Raton: CRC Press, 2010. ISBN: 978-1-4398-0247-2.
- [51] R. B. Hetnarski and J. Ignaczak. *The Mathematical Theory of Elasticity*. 2nd ed. Boca Raton: CRC Press, 2011. ISBN: 978-1-4398-2888-5.

- [52] J. Kacher and I.M. Robertson. "Quasi-four-dimensional analysis of dislocation interactions with grain boundaries in 304 stainless steel". In: *Acta Materialia* 60.19 (2012), pp. 6657–6672. ISSN: 1359-6454. DOI: <https://doi.org/10.1016/j.actamat.2012.08.036>.
- [53] A. J. Wilkinson and P. B. Hirsch. "Electron diffraction based techniques in scanning electron microscopy of bulk materials". In: *Micron* 28.4 (1997), pp. 279–308. ISSN: 0968-4328. DOI: [https://doi.org/10.1016/S0968-4328\(97\)00032-2](https://doi.org/10.1016/S0968-4328(97)00032-2).
- [54] D. J. Bacon, D. M. Barnett, and R. O. Scattergood. "Anisotropic continuum theory of lattice defects". In: *Progress in Materials Science* 23 (1980), pp. 51–262. DOI: 10.1016/0079-6425(80)90007-9.
- [55] S. Lang. *Calculus of Several Variables*. 3rd ed. Undergraduate Texts in Mathematics. New York: Springer-Verlag, 1987. ISBN: 038796405.
- [56] J. E. Marsden and A. Tromba. *Vector Calculus*. 5th ed. New York: W.H. Freeman and Company, 2003. ISBN: 0716749920.
- [57] P. C. Matthews. *Vector Calculus*. Springer undergraduate mathematics series. Berlin: Springer, 1998. ISBN: 3540761802.
- [58] I. M. Gel'fand and G. E. Shilov. *Generalized Functions – Volume 1: Properties and Operations*. Translated by E. Saletan and others. New York: Academic Press, 1964.
- [59] D. S. Jones. *The Theory of generalised functions*. 2nd ed. Cambridge: Cambridge University Press, 1982. ISBN: 0521237238.
- [60] R. P. Kanwal. *Generalized Functions: Theory and Applications*. Boston: Birkhäuser, 2004. ISBN: 0817643435.
- [61] A. El Kinani and M. Oudadess. *Distribution Theory and Applications*. Series on Concrete and Applicable Mathematics – vol. 9. New Jersey: World Scientific, 2010. ISBN: 9789814304917.
- [62] T. Mura. *Micromechanics of Defects in Solids*. 2nd ed. Dordrecht: Kluwer Academic Publishers, 1991. ISBN: 90-247-3256-5.
- [63] E. Kröner. "Continuum theory of defects". In: *Physics of Defects* 35 (1981), pp. 217–315.
- [64] J. M. Burgers. "Some considerations on the fields of stress connected with dislocations in a regular crystal lattice. I". In: *Proc. Kon. Ned. Akad. Wet.* Vol. 42. 1939, pp. 293–325.
- [65] M. Peach and J. S. Koehler. "The Forces Exerted on Dislocations and the Stress Fields Produced by Them". In: *Physical Review* 80.3 (1950), pp. 436–439. DOI: 10.1103/PhysRev.80.436.

- [66] J. D. Eshelby. "The force on an elastic singularity". In: *Philosophical Transactions of the Royal Society of London A: Mathematical, Physical and Engineering Sciences* 244.877 (1951), pp. 87–112. ISSN: 0080-4614. DOI: 10.1098/rsta.1951.0016.
- [67] J. D. Eshelby. "The Continuum Theory of Lattice Defects". In: ed. by Frederick Seitz and David Turnbull. Vol. 3. Solid State Physics. Academic Press, 1956, pp. 79–144. DOI: [https://doi.org/10.1016/S0081-1947\(08\)60132-0](https://doi.org/10.1016/S0081-1947(08)60132-0).
- [68] S.D. Gavazza and D.M. Barnett. "The self-force on a planar dislocation loop in an anisotropic linear-elastic medium". In: *Journal of the Mechanics and Physics of Solids* 24.4 (1976), pp. 171–185. DOI: 10.1016/0022-5096(76)90001-6.
- [69] S. D. Gavazza and D. M. Barnett. "The image force on a dislocation loop in a bounded elastic medium". In: *Scripta Metallurgica* 9.11 (1975), pp. 1263–1265. ISSN: 0036-9748. DOI: [https://doi.org/10.1016/0036-9748\(75\)90421-4](https://doi.org/10.1016/0036-9748(75)90421-4).
- [70] S. D. Gavazza. "Energy Release Rates and Associated Forces on Singular Dislocations". PhD thesis. Stanford University, 1975.
- [71] W. Wu, R. Schäublin, and J. Chen. "General dislocation image stress of anisotropic cubic thin film". In: *Journal of Applied Physics* 112.9 (2012), p. 093522. DOI: 10.1063/1.4764341. URL: <https://doi.org/10.1063/1.4764341>.
- [72] H. Zbib and T. Khraishi. "Chapter 84 - Size Effects and Dislocation – Wave Interaction in Dislocation Dynamics". In: *Dislocations in Solids: A Tribute to F.R.N. Nabarro*. Ed. by J. P. Hirth. Vol. 14. Dislocations in Solids. Elsevier, 2008, pp. 207–249. DOI: [https://doi.org/10.1016/S1572-4859\(07\)00004-6](https://doi.org/10.1016/S1572-4859(07)00004-6).
- [73] W. Cai et al. "A non-singular continuum theory of dislocations". In: *Journal of the Mechanics and Physics of Solids* 54.3 (2006), pp. 561–587. DOI: 10.1016/j.jmps.2005.09.005.
- [74] L. M. Brown. "The self-stress of dislocations and the shape of extended nodes". In: *The Philosophical Magazine: A Journal of Theoretical Experimental and Applied Physics* 10.105 (1964), pp. 441–466. DOI: 10.1080/14786436408224223.
- [75] A. Deffo, M. P. Ariza, and M. Ortiz. "A Line-free Method of Monopoles for 3D Dislocation Dynamics". In: *ArXiv e-prints* (June 2018). arXiv: 1806.04512 [physics.comp-ph].
- [76] Yang. Xiang et al. "A level set method for dislocation dynamics". In: *Acta Materialia* 51.18 (2003), pp. 5499–5518. DOI: 10.1016/S1359-6454(03)00415-4.

- [77] R. Fertig and S. Baker. "Simulation of dislocations and strength in thin films: A review". In: *Progress in Materials Science* 54.6 (2009), pp. 874–908. ISSN: 0079-6425. DOI: <https://doi.org/10.1016/j.pmatsci.2009.03.004>.
- [78] R. Sills et al. "Fundamentals of Dislocation Dynamics Simulations". In: *Multiscale Materials Modeling for Nanomechanics*. Ed. by C. Weinberger and G. Tucker. Vol. 245. Springer Series in Materials Science. Springer, 2016. Chap. 2, pp. 53–88. ISBN: 978-3-319-33480-6.
- [79] L. Kubin. *Dislocations, mesoscale simulations and plastic flow (Oxford Series on Materials Modelling)*. Oxford Series on Materials Modelling. Oxford: Oxford University Press, 2013. ISBN: 978-0-19-852501-1.
- [80] B. Devincre et al. *Modeling crystal plasticity with dislocation dynamics simulations: The 'microMegas' code*. Jan. 2011.
- [81] M. Verdier, M. Fivel, and I. Groma. "Mesoscopic scale simulation of dislocation dynamics in fcc metals: Principles and applications". In: *Modelling and Simulation in Materials Science and Engineering* 6.6 (1998), p. 755. URL: <http://stacks.iop.org/0965-0393/6/i=6/a=007>.
- [82] N. Ghoniem, S. Tong, and L. Sun. "Parametric dislocation dynamics: A thermodynamics-based approach to investigations of mesoscopic plastic deformation". In: *Phys. Rev. B* 61 (2 Jan. 2000), pp. 913–927. DOI: 10.1103/PhysRevB.61.913. URL: <https://link.aps.org/doi/10.1103/PhysRevB.61.913>.
- [83] T. Arsenlis et al. *Parallel Dislocation Simulator*. URL: <http://paradis.stanford.edu/site/home>.
- [84] L. Greengard and V. Rokhlin. "A fast algorithm for particle simulations". In: *Journal of Computational Physics* 73 (1987), pp. 325–348.
- [85] Feng Zhao. "An O(N) Algorithm for Three-Dimensional N-Body Simulations". In: (1987). URL: <http://dspace.mit.edu/handle/1721.1/6962>.
- [86] L. Greengard and W. D. Gropp. "A parallel version of the fast multipole method". In: *Computers Mathematics with Applications* 20.7 (1990), pp. 63–71.
- [87] R. Beatson and L. Greengard. "A short course on fast multipole methods". In: *Wavelets, Multilevel Methods and Elliptic PDEs*. Oxford University Press, 1997, pp. 1–37.
- [88] Nasr M. Ghoniem and L. Z. Sun. "Fast-sum method for the elastic field of three-dimensional dislocation ensembles". In: *Phys. Rev. B* 60 (1 July 1999), pp. 128–140. DOI: 10.1103/PhysRevB.60.128. URL: <https://link.aps.org/doi/10.1103/PhysRevB.60.128>.
- [89] Zhiqiang Wang, Nasr Ghoniem, and Richard LeSar. "Multipole representation of the elastic field of dislocation ensembles". In: *Physical Review B* 69.17 (2004). DOI: 10.1103/PhysRevB.69.174102.

- [90] V. Kain. "5 - Stress corrosion cracking (SCC) in stainless steels". In: *Stress Corrosion Cracking*. Ed. by V.S. Raja and Tetsuo Shoji. Woodhead Publishing Series in Metals and Surface Engineering. Woodhead Publishing, 2011, pp. 199–244. ISBN: 978-1-84569-673-3. DOI: <https://doi.org/10.1533/9780857093769.3.199>. URL: <http://www.sciencedirect.com/science/article/pii/B9781845696733500055>.
- [91] A. Argon. *Strengthening Mechanisms in Crystal Plasticity*. Oxford Series on Materials Modelling. Oxford: Oxford University Press, 2008.
- [92] T. Byun, N. Hashimoto, and K. Farrell. "Temperature dependence of strain hardening and plastic instability behaviors in austenitic stainless steels". In: *Acta Materialia* 52.13 (2004), pp. 3889–3899. ISSN: 1359-6454. DOI: <https://doi.org/10.1016/j.actamat.2004.05.003>.
- [93] M. Koslowski, A. M. Cuitiño, and M. Ortiz. "A phase-field theory of dislocation dynamics, strain hardening and hysteresis in ductile single crystals". In: *Journal of the Mechanics and Physics of Solids* 50 (2002), pp. 2597–2635.
- [94] V. A. Lubarda, J. A. Blume, and A. Needleman. "An analysis of equilibrium dislocation distributions". In: *Acta Metallurgica et Materialia* 41.2 (1993), pp. 625–642. DOI: 10.1016/0956-7151(93)90092-7.
- [95] L. Ambrosio, N. Fusco, and D. Pallara. *Functions of Bounded Variation and Free Discontinuity Problems*. Mathematical Monographs. Oxford University Press, 2000.
- [96] S. Conti, A. Garroni, and A. Massaccesi. "Modeling of dislocations and relaxation of functionals on 1-currents with discrete multiplicity". In: *Calculus of Variations and Partial Differential Equations* 54.2 (2015), pp. 1847–1874. ISSN: 0944-2669. DOI: 10.1007/s00526-015-0846-x. URL: <https://www.wos.org/doi/10.1007/s00526-015-0846-x>.
- [97] C. Villani. *Topics in Optimal Transportation Theory*. Vol. 58. Graduate Studies in Mathematics. Providence, Rhode Island, USA: American Mathematical Society, 2003.
- [98] R. Jordan, D. Kinderlehrer, and F. Otto. "The variational formulation of the Fokker-Planck equation". In: *SIAM Journal on Mathematical Analysis* 29.1 (1998), pp. 1–17.
- [99] B. Li, F. Habbal, and M. Ortiz. "Optimal transportation meshfree approximation schemes for fluid and plastic flows". In: *International Journal for Numerical Methods in Engineering* 83.12 (2010), pp. 1541–1579.
- [100] L. Fedeli, A. Pandolfi, and M. Ortiz. "Geometrically-exact time-integration mesh-free schemes for advection-diffusion problems derived from optimal transportation theory and their connection with particle methods". In: *International Journal for Numerical Methods in Engineering* 112.9 (2017), pp. 1175–1193. DOI: 10.1002/nme.5552.

- [101] M. Arroyo and M. Ortiz. “Local maximum-entropy approximation schemes: a seamless bridge between finite elements and meshfree methods”. In: *International Journal for Numerical Methods in Engineering* 65.13 (2006), pp. 2167–2202. DOI: 10.1002/nme.1534.
- [102] F. Morgan. *Geometric measure theory. A beginner’s guide*. Academic Press, Inc., Boston, MA, 1988, pp. viii+145. ISBN: 0-12-506855-7.
- [103] M. Giaquinta, G. Modica, and J. Soucek. *Cartesian Currents in the Calculus of Variations, vols. I and II*. Vol. 37. Modern Surveys in Mathematics. Berlin, Heidelberg: Springer-Verlag, 1998.
- [104] M. P. Ariza and M. Ortiz. “Discrete crystal elasticity and discrete dislocations in crystals”. In: *Archive for Rational Mechanics and Analysis* 178.2 (2005), pp. 149–226.
- [105] S. Conti, A. Garroni, and M. Ortiz. “The Line-Tension Approximation as the Dilute Limit of Linear-Elastic Dislocations”. In: *Archive for Rational Mechanics and Analysis* 218.2 (2015), pp. 699–755. ISSN: 0003-9527. DOI: 10.1007/s00205-015-0869-7. URL: %3CGo%20to%20ISI%3E://WOS:000358797700003.
- [106] T. Mura. “Continuous distribution of moving dislocations”. In: *The Philosophical Magazine: A Journal of Theoretical Experimental and Applied Physics* 8.89 (1963), pp. 843–857. DOI: 10.1080/14786436308213841.
- [107] J. F. Nye. “Some geometrical relations in dislocated crystals”. In: *Acta Metallurgica* 1.2 (1953), pp. 153–162. DOI: 10.1016/0001-6160(53)90054-6.
- [108] E. Kroner. “Berechnung der elastischen Konstanten des Vielkristalls aus den Konstanten des Einkristalls”. In: *Zeitung der Physik* 151 (1958), pp. 504–518.
- [109] R. Bott and L. W. Tu. *Differential Forms in Algebraic Topology*. Springer-Verlag, 1982.
- [110] W. Gangbo and R. J. McCann. “The Geometry of Optimal Transportation”. In: *Acta Mathematica* 177.2 (1996), pp. 113–161.
- [111] R. T. Rockafellar. *Convex analysis*. Princeton mathematical series, Princeton, N. J.: Princeton University Press, 1970, xviii, 451 p. ISBN: 0691080690. URL: Publisher%20description%20http://www.loc.gov/catdir/description/prin051/68056318.html.
- [112] R. Abraham, J. E. Marsden, and T. S. Ratiu. *Manifolds, tensor analysis, and applications*. 2nd. Applied mathematical sciences. New York: Springer-Verlag, 1988.
- [113] G. Stampacchia. “Le problème de Dirichlet pour les équations elliptiques du second ordre à coefficients discontinus”. In: *Annales du Institut Fourier (Grenoble)* 15 (1965), pp. 189–258.

- [114] A. Ramasubramaniam, M. P. Ariza, and M. Ortiz. "A discrete mechanics approach to dislocation dynamics in BCC crystals". In: *Journal of the Mechanics and Physics of Solids* 55.3 (2007), pp. 615–647.
- [115] P. Rosakis and A. J. Rosakis. "The Screw Dislocation Problem in Incompressible Finite Elastostatics - a Discussion of Nonlinear Effects". In: *Journal of Elasticity* 20.1 (1988), pp. 3–40.
- [116] S. Muller and M. Palombaro. "Existence of minimizers for a polyconvex energy in a crystal with dislocations". In: *Calculus of Variations and Partial Differential Equations* 31.4 (2008), pp. 473–482.
- [117] W. Rudin. *Functional analysis*. 2nd. International series in pure and applied mathematics. New York: McGraw-Hill, 1991.
- [118] R. Jordan, D. Kinderlehrer, and F. Otto. "Free energy and the Fokker-Planck equation". In: *Physica D: Nonlinear Phenomena* 107.2 (1997). 16th Annual International Conference of the Center for Nonlinear Studies, pp. 265–271. ISSN: 0167-2789. DOI: 10.1016/S0167-2789(97)00093-6.
- [119] R. Jordan, D. Kinderlehrer, and F. Otto. "Dynamics of the Fokker-Planck equation". In: *Phase Transitions - B* 69.3 (1999), pp. 271–288.
- [120] M. Ortiz and J. B. Martin. "Symmetry-Preserving Return Mapping Algorithms and Incrementally Extremal Paths: A Unification of Concepts". In: *International Journal for Numerical Methods in Engineering* 28 (1989), pp. 1839–1853.
- [121] E. Polak and G. Ribiere. "Note on Convergence of Conjugate Direction Methods". In: *Revue Francaise D Informatique De Recherche Operationnelle* 3.16 (1969), pp. 35–+. ISSN: 0035-3035.
- [122] S. Balay et al. "Efficient Management of Parallelism in Object Oriented Numerical Software Libraries". In: *Modern Software Tools in Scientific Computing*. Ed. by Arge, E., Bruaset, A. M. and Langtangen, H. P. Birkhäuser Press, 1997, pp. 163–202.
- [123] S. Conti, A. Garroni, and S. Mueller. "Dislocation microstructures and strain-gradient plasticity with one active slip plane". In: *Journal of the Mechanics and Physics of Solids* 93 (2016). Special Issue in honor of Michael Ortiz, pp. 240–251. ISSN: 0022-5096. DOI: <https://doi.org/10.1016/j.jmps.2015.12.008>. URL: <http://www.sciencedirect.com/science/article/pii/S002250961530363X>.
- [124] S. Lang. *A First Course in Calculus*. Addison-Wesley Series in Mathematics. Reading, Mass: Addison-Wesley Publishing Company, 1964.
- [125] M. Spivak. *Calculus*. 4th ed. Houston: Publish or Perish, Inc., 2008. ISBN: 978-0-914098-91-1.
- [126] J. Rogawski. *Calculus: Early Transcendentals*. New York: W.H. Freeman and Company, 2008. ISBN: 978-1-4292-0841-3.

- [127] Y. Zhu, S. Chapman, and A. Acharya. "Dislocation motion and instability". In: *Journal of the Mechanics and Physics of Solids* 61.8 (2013), pp. 1835–1853. DOI: 10.1016/j.jmps.2013.03.002.
- [128] W. Cai and V. Bulatov. "Mobility laws in dislocation dynamics simulations". In: *Materials Science and Engineering: A* 387-389 (2004), pp. 277–281. DOI: 10.1016/j.msea.2003.12.085.
- [129] T.A. Khraishi et al. "The stress field of a general circular Volterra dislocation loop: Analytical and numerical approaches". In: *Philosophical Magazine Letters* 80.2 (2000), pp. 95–105. DOI: 10.1080/095008300176353.
- [130] F. Kroupa. "Circular edge dislocation loop". In: *Czechoslovakij fiziceskij zurnal B* 10.4 (1960), pp. 284–293. DOI: 10.1007/BF02033533.
- [131] J. Yin, D. Barnett, and W. Cai. "Efficient computation of forces on dislocation segments in anisotropic elasticity". In: *Modelling and Simulation in Materials Science and Engineering* 18.4 (2010), p. 045013. URL: <http://stacks.iop.org/0965-0393/18/i=4/a=045013>.
- [132] W. Han and B. Reddy. *Plasticity: Mathematical Theory and Numerical Analysis*. 2nd ed. Interdisciplinary Applied Mathematics. New York: Springer-Verlag, 2013. ISBN: 978-1-4614-5939-2.

## Appendix A

### INTERPOLATED TRANSPORT MAPS

#### A.1 Zeroth-order Max Ent Shape Functions

The zeroth-order consistent max-ent shape functions at  $\mathbf{x}$  are the solutions of the constrained optimization problem [101]

$$\text{Minimize: } \sum_{a=1}^M \beta_a N_a(\mathbf{x}) |\mathbf{x} - \mathbf{x}_a|^2 + \sum_{a=1}^M N_a(\mathbf{x}) \log N_a(\mathbf{x}), \quad (\text{A.1a})$$

$$\text{subject to: } N_a(\mathbf{x}) \geq 0, \quad a = 1, \dots, M, \quad \sum_{a=1}^M N_a(\mathbf{x}) = 1, \quad (\text{A.1b})$$

where  $\{\mathbf{x}_a\}_{a=1}^M$  are the nodes of the interpolation and  $\{\beta_a\}_{a=1}^M$  are adjustable parameters. The shape functions thus defined supply the least biased and most local reconstruction of a function whose values are known on the node set [101]. Problem (A.1) can be solved explicitly, with the result

$$N_a(\mathbf{x}) = \frac{1}{Z} \exp\left(-\frac{\beta_a}{2} |\mathbf{x} - \mathbf{x}_a|^2\right), \quad (\text{A.2})$$

where

$$Z = \sum_{a=1}^M \exp\left(-\frac{\beta_a}{2} |\mathbf{x} - \mathbf{x}_a|^2\right) \quad (\text{A.3})$$

is the partition function. Suppose that the nodes moves to new positions  $\{\mathbf{y}_a\}_{a=1}^M$ . We then define an interpolated transport map as

$$\varphi(\mathbf{x}) = \mathbf{x} + \sum_{a=1}^M (\mathbf{y}_a - \mathbf{x}_a) N_a(\mathbf{x}), \quad (\text{A.4})$$

with gradient

$$\nabla \varphi(\mathbf{x}) = \mathbf{I} + \sum_{a=1}^M (\mathbf{y}_a - \mathbf{x}_a) \nabla N_a(\mathbf{x}). \quad (\text{A.5})$$

#### A.2 Tests

##### Translation of the Monopoles

Suppose that  $\mathbf{y}_a = \mathbf{x}_a + \mathbf{u}$ , i.e., the nodal set translates by  $\mathbf{u}$ . From the zeroth-order condition, we find

$$\varphi(\mathbf{x}) = \mathbf{x} + \left( \sum_{a=1}^M N_a(\mathbf{x}) \right) \mathbf{u} = \mathbf{x} + \mathbf{u}, \quad (\text{A.6})$$

and

$$\nabla\varphi(\mathbf{x}) = \mathbf{I} + \left( \sum_{a=1}^M \nabla N_a(\mathbf{x}) \right) \mathbf{u} = \mathbf{I} \quad (\text{A.7})$$

so that

$$\boldsymbol{\xi}_{a,\nu+1} = \nabla\varphi(\mathbf{x}_a)\boldsymbol{\xi}_{a,\nu} = \boldsymbol{\xi}_{a,\nu}$$

as required.

### Rotation of the Monopoles

Now, suppose that  $\mathbf{y}_a = \mathbf{R}\mathbf{x}_a$  for some  $\mathbf{R} \in SO(3)$ , i.e., the nodal set rotates under a constant tensor  $\mathbf{R}$ . From (A.4), we have that

$$\varphi(\mathbf{x}) = \mathbf{x} + \sum_{a=1}^M (\mathbf{R}\mathbf{x}_a - \mathbf{x}_a)N_a(\mathbf{x}) \quad (\text{A.8})$$

or, in index notation,

$$\begin{aligned} \varphi_i(\mathbf{x}) &= x_i + \sum_{a=1}^M (R_{ij}x_j^a - x_i^a)N_a(\mathbf{x}) \\ &= x_i + \sum_{a=1}^M (R_{ij} - \delta_{ij})x_j^a N_a(\mathbf{x}) \\ &= x_i + (R_{ij} - \delta_{ij}) \sum_{a=1}^M N_a(\mathbf{x})x_j^a. \end{aligned} \quad (\text{A.9})$$

If we further assume—as in [101]—that the shape functions satisfy the first-order consistency condition

$$\sum_{a=1}^M N_a(\mathbf{x})x_a = \mathbf{x} \quad \forall \mathbf{x}, \quad (\text{A.10})$$

then (A.9) simplifies to

$$\varphi_i(\mathbf{x}) = R_{ij}x_j \quad (\text{A.11})$$

so that

$$\nabla\varphi(\mathbf{x}) = \mathbf{R}. \quad (\text{A.12})$$

It follows that

$$\begin{aligned} |\boldsymbol{\xi}_{a,\nu+1}| &= |\nabla\varphi(\mathbf{x}_a)\boldsymbol{\xi}_{a,\nu}| \\ &= |\mathbf{R}\boldsymbol{\xi}_{a,\nu}| \\ &= |\boldsymbol{\xi}_{a,\nu}| \end{aligned} \quad (\text{A.13})$$

again as required.

We note that although the shape functions given by Equations (A.2) and (A.3) do not satisfy the first-order consistency condition (A.10) in general, this is typically not an issue for problems in the small deformation setting where rigid body motion leaves the body unstrained [132]. However, for problems in large deformation, the chosen shape functions should satisfy both the zeroth- and first-order consistency conditions (A.1b) and (A.10). An example of such shape functions is given by Equations (17) and (18) of reference [101].